



TECHNISCHE
UNIVERSITÄT
WIEN
Vienna | Austria



MASTERARBEIT

Suche nach Physik jenseits des Standardmodells mit dem CRESST-Experiment

ausgeführt am
Institut für Hochenergiephysik
der Österreichischen Akademie der Wissenschaften

der Technischen Universität Wien

unter der Anleitung von
Univ.Prof. Dipl.-Phys. Dr.rer.nat. Jochen Schieck
Univ.Ass. Dipl.-Phys. Dr.rer.nat. Achim Gütlein

durch
Lukas Zehrer, BSc
3200 Ober-Grafendorf

Datum

Unterschrift

Abstract

In spite of the successes of observational astro- and particle physics and cosmology very much of the universe remains unknown. The Standard Model of particle physics is a theory describing the electromagnetic, weak, and strong nuclear interactions, as well as classifying all the subatomic particles known. But there is overwhelming evidence, that all the known particles, the ordinary (baryonic) matter, the building blocks of planets, stars and ourselves, only make up about 4.9% of the energy content of the universe. The standard model of cosmology (Λ CDM) indicates that the total mass-energy of the universe contains beside the 4.9% ordinary matter two other components: 26.8% dark matter and 68.3% dark energy.

The accelerating expansion of the Universe is the result of the effect of the dark energy with its most simple form given by a cosmological constant Λ in Einstein's Equation.

Dark matter is an unidentified type of matter that is not accounted for by dark energy and neutrinos and is generally believed to be a non-relativistic, charge neutral and non-baryonic new form of matter. Although dark matter has not been directly observed yet, its existence and properties are inferred from its gravitational effects such as the motions of visible matter, gravitational lensing, its influence on the universe's large-scale structure, and its effects in the cosmic microwave background.

Thus the search for Dark Matter is the search for physics beyond the standard model. Although the nature of dark matter is yet unknown, its presence is crucial to understanding the future of the universe.

The CRESST experiment is searching for direct evidence in the form of a nuclear recoil induced on a scintillating CaWO_4 crystal by a dark matter particle, and is installed and taking data underground at Laboratory Nazionali del Gran Sasso (LNGS) in Italy.

While both, dark energy and dark matter, have not been detected directly, a class of dark matter particles that interact only via gravity and the weak force, referred to as Weakly Interacting Massive Particles (WIMPs), has been established as the leading candidate among the dark matter community.

For this thesis a special model of dark matter was studied, namely the dark photon.

This thesis provides a detailed description of the calculation of the 90% upper limit on the dark photon kinetic mixing κ based on data from the second phase of the CRESST experiment. The analysis was carried out in a frequentist approach based on the (unbinned) maximum-likelihood method and likelihood ratios. To make a statement about the calculated result and its quality, the used algorithm had to be tested, what was done with Monte Carlo simulations (pseudo data).

Contents

1. Dark Matter	1
1.1. Introduction	1
1.1.1. Additional	3
1.2. Indications of Dark Matter	4
1.2.1. Dynamics of Galaxy Clusters	4
1.2.2. 21 cm Hydrogen Line	4
1.3. Evidence	5
1.3.1. Dynamics of Galaxies	5
1.3.2. Gravitational Lensing	11
1.3.3. Cosmic Microwave Background	16
1.3.4. Large Scale Structure	26
1.4. The Standard Model of Cosmology - Λ CDM Model	32
1.5. The Standard Model of Particle Physics	34
1.5.1. Shortcomings of the SM	36
1.6. Unsolved Questions and Open Issues	38
1.6.1. Core-Cusp Problem	38
1.6.2. Missing Satellite Problem	39
1.6.3. "Too big to fail" Problem	41
1.7. Dark Matter Detection	42
1.7.1. Direct Dark Matter Detection	43
1.7.2. Indirect Dark Matter Detection	46
1.7.3. Dark Matter Production	48
1.7.4. Axion Searches	48
1.8. Dark Matter (Particle) Candidates	50
1.8.1. WIMP	51
1.8.2. Asymmetric Dark Matter (ADM)	53
1.8.3. Axion	54
1.8.4. SUSY	55
1.8.5. Dark Photons (Vector Particles)	56
1.8.6. Alternative Theories	62
1.9. Conclusion	62
2. The CRESST Experiment	63
2.1. Phases	66
2.1.1. CRESST-II	66
2.1.2. CRESST-III	68
2.2. Calcium tungstate CaWO_4	69
3. Statistics	71
3.1. Interpretation of probability	72

3.2. Probability density function	75
3.2.1. Quantile	77
3.3. Statistical tests, Hypotheses	78
3.4. Parameter estimation	79
3.5. The method of maximum likelihood	80
3.5.1. The log-likelihood function	82
3.5.2. Extended maximum likelihood	82
3.5.3. Fitting a model to data	84
3.6. Wilks' Theorem	85
4. Analysis (Software), discussion and results	87
4.1. The model	87
4.2. Likelihood fit	90
4.3. Limit	91
4.4. Algorithm	93
4.5. Test-Software	95
4.5.1. Testing the $t(\eta)$ - vs. χ_1^2 - distribution	97
4.6. Results	99
A. Appendix	107
A.1. Redshift and Doppler Effect	107
A.2. Distance Measurement	107
A.2.1. Stellar Parallax	107
A.2.2. Standard Candle	107
A.2.3. Pulsating Variable Stars	107
A.3. Cosmology	108
A.3.1. General Relativity	108
A.3.2. FLRW Metric	109
A.3.3. Friedmann Equation	109
A.4. Milky Way	110
A.5. Galaxy Clusters	113
A.6. Gas in the Universe	114
A.7. Horizontal Branch	115
A.8. Vectors, scalars, and spinors	115
A.9. The Lagrangian	116
List of Figures	A
References	E

1. Dark Matter

This chapter gives an explanation to the notion "Dark Matter", its indications and the observed evidence.

Dark matter is undetectable by any electromagnetic radiation at our disposal - it can't be seen in the visible range, it can't be detected by radio waves at the low end of the spectrum or by the X-rays at the high end of the spectrum. It appears not to interact by the electromagnetic force. The obvious question is then "How do we know it is there?". With the answer to that - it interacts by gravity and thereby produces measurable results, as all observation of "Dark Matter" so far are based on gravitational interactions.

The following sections present how we got to know some characteristics of dark matter, like it is non-luminous (i.e. electrically neutral), has a weak (or even less) interaction with ordinary matter, a low self-interaction cross-section, is stable with respect to the lifetime of the universe, is non-baryonic and (probably) is a massive particle as it acts gravitationally (there is no evidence for the particle character of "Dark Matter", however, it is well motivated from the particle physics point of view), and we still don't know its origins.

An historical outline is presented, starting with the dynamics of galaxies and galaxy clusters, coming to a brief introduction on cosmology, going to the **standard model** of particle physics (**SM**) and its deficiencies (like not explained phenomena and experimental results, not observed theoretical predictions and theoretical problems), concluding with an explanation on how the search for dark matter is one field in the search for physics **beyond the standard model (BSM)**. Some constraints on the nature of dark matter are represented in the course of describing some phenomena, as well as methods on detection of dark matter are explained (whereat in chapter 2 the main focus lies on the CRESST experiment) and in the end candidates for dark matter (particles) are illustrated (where *dark photons* are described in section 1.8.5, which are needed in chapter 4).

1.1. Introduction

In the late 18th Century, long before distances to stars were known, William Herschel tried to estimate the size and shape of our Galaxy. In visible light we see an accumulation of stars, but the structure is not so clear. Herschel did not realize, that most of the stars were obscured from his view and concluded the Galaxy was a flattened, disk-shaped object, with the Sun near the center, greatly underestimating the size of the galaxy. At the beginning of the 20th century, the prevailing view of the cosmos was, that the universe consisted entirely of our own - the Milky Way - galaxy (an actual visualization can be seen in fig. 38 on page 112 and fig. 37 on page 111).

Due to the work of scientists like H. S. Leavitt (relation of luminosity and period for Cepheids - a kind of star that is used to determine the distance from the galaxy using as *standard candle* (see appendix A.2); and eq. (1)), J. E. Keeler, W. W. Campbell, V. M. Slipher (first discovery of the shift of spectral lines of galaxies - galactic redshifts, eq.

(3) and (32); [1]) and E. Hubble it was proven that extragalactic objects exist.

$$F = \frac{L}{4\pi d^2} \Rightarrow d = \sqrt{\frac{L}{4\pi F}}, \quad (1)$$

states, that the distance d of a galaxy can be calculated from light flux F from objects with defined luminosity L (Standard Candles e.g. Cepheid variable stars, supernovae Ia). With:

$$L = 4\pi R^2 \sigma T^4, \quad (2)$$

where L is the luminosity of a star (assuming the star is a black body, compare fig. 11, which is a good approximation), the temperature T , and radius R of the star and σ is the Stefan-Boltzmann constant $5.67 \cdot 10^{-8} \text{ W m}^{-2} \text{ K}^{-4}$.

With the the redshift z (and blueshift, where $z < 0$), a dimensionless quantity, as instrument to measure velocity of recession of galaxies

$$z = \sqrt{\frac{1 + \beta}{1 - \beta}} - 1, \quad (3)$$

where $\beta = \frac{v}{c}$, v the velocity at which the source moves away from the observer, c the speed of light and

$$z = \frac{\lambda_{ob} - \lambda_{em}}{\lambda_{em}} = \frac{\lambda_{ob}}{\lambda_{em}} - 1, \quad (4)$$

where z is characterized by the relative difference between the observed (λ_{ob}) and emitted (λ_{em}) wavelengths (or frequency ν - convert via $c = \lambda \cdot \nu$) of an object. More to the topic of redshift and the Doppler Effect see in appendix A.1.

Hubble identified Cepheid variables amongst others in the Andromeda Nebula (M31) (brief explanation see section 1.1.1). This observations (made in 1922-1923) consequently proved that these nebulae were much too distant to be part of the Milky Way and were, in fact, entire galaxies outside our own. The Coma Cluster is one example of a collection of many galaxies, each consisting of hundreds of billions of stars, as well as there are many different types of galaxies. Also Hubble was the first to categorize galaxies in a comprehensive way (see fig. 39 in appendix - A.4):

- Spirals
- Barred spirals
- Ellipticals
- Irregulars

These results changed the scientific view of the universe fundamentally. Nowadays it is known that many galaxies exist and are estimated to (at least) 200 billion galaxies (arranged in clusters - more see appendix A.5) in the observable universe. (Current observations estimate the number of galaxies in the observable universe to \approx two trillion, almost a factor of ten higher than would be seen in an all sky survey at Hubble Ultra-Deep Field depth. [2])

Hubble also formulated the famous *Hubble law* (eq. (5)) in 1929 [3] stating that the redshift of an astronomical object is linearly proportional to its distance, however the discovery of the expanding Universe was already made two years earlier in 1927 by Georges Lemaître [4] (and was based on the discovery of the redshift by Milton Humanson and the spatial distribution of the galaxies).

$$v = H_0 d, \quad (5)$$

is a linear relation between recess velocity v and the distance d , with $H_0 = 68 \text{ km s}^{-1} \text{ Mpc}^{-1}$ the Hubble constant (Hubble parameter), and respectively the redshift (when the velocity v is much less than the speed of light ($v \ll c$ and $\gamma \approx 1$ - eq. (7)) z becomes $z \approx \frac{v}{c}$) is given by

$$z = \frac{H_0 d}{c}. \quad (6)$$

With these findings we got to know, that most galaxies recede from us, it became possible to measure the velocities at which they recede from us, their distance and that the recession speed is larger for more distant galaxies.

This was determined from the Doppler effect (see appendix A.1). A redshift resulting from Hubble flow is called the *cosmological redshift*. The whole universe is expanding. Galaxies are moving away from all points in space - not just us (more on this topic in section A.3).

1.1.1. Additional

Lorentz Factor γ

$$\gamma = \frac{1}{\sqrt{1 - \frac{v^2}{c^2}}} = \frac{1}{\sqrt{1 - \beta^2}}, \quad (7)$$

the Lorentz factor (or Lorentz term).

Measure of length 1 Mpc = 1 Mega parsec = $1 \cdot 10^6$ parsec, with 1 parsec = $3.0857 \cdot 10^{16} \text{ m}$ = 3.26156 ly, and 1 ly = $9.4607 \cdot 10^{15} \text{ m}$.

Messier Catalogue Astronomers often refer to objects (stars, nebula, galaxies, etc.) by their number in the Messier Catalogue, which the 18th century French astronomer Charles Messier compiled to aid him in his search for comets.

1.2. Indications of Dark Matter

1.2.1. Dynamics of Galaxy Clusters

In 1933 Fritz Zwicky studied two neighbouring galaxy clusters, Coma and Virgo and was the first to apply the virial theorem

$$M = \frac{5R}{3G} \overline{v^2} \quad (8)$$

to astrophysics [5] by relating the observed velocity of galaxies with the gravitational potential. By estimating the gravitational mass based on the motions of galaxies near its (the clusters) edge, then comparing it to an estimate based on its luminosity and number of galaxies, he obtained that the velocities of the individual galaxies that belonged to a cluster were of several hundred times greater than expected from Kepler's law (he deduced a ratio of gravitational interacting matter to luminous matter of $400 M_{\odot}/L_{\odot}$, given in terms of solar mass M_{\odot} and solar luminosity L_{\odot}). The more mass there is in the galaxy cluster, the stronger are the forces exerted on each single galaxy and the higher is their speed. Zwicky verified that the gravity effect of the visible galaxies was far too small for such fast orbits, thus far more *non-luminous* matter than observed luminous matter must be contained to hold the cluster via its associated gravitational attraction together, calling it *dunkle Materie* "**dark** matter". [6] This was the first indication found for dark matter, stating that most of the matter in galaxy clusters is dark.

1.2.2. 21 cm Hydrogen Line

In 1959 Louise Volders demonstrated deviations expected according to Keplerian dynamics in the spinning of the Triangulum Galaxy (M33) - spiral galaxy - by observations of the Doppler shift of the 21 cm radio line. Because it is a radio frequency it passes undisturbed through dust, and is thus a good tool for measurements on this big scales. (This effect originates when the electron of the hydrogen atom flips its spin, and then it emits a 21 cm radio wave.)

1.3. Evidence

Today the evidence in favour of dark matter is stronger than it has ever been! To mention just a few examples, by means of Astrophysical motivations

- Rotation curves of spiral galaxies
- Gravitational lensing for galaxy clusters

and Cosmological motivations

- Large-scale structure of the Universe
- Anisotropy of cosmic microwave background (CMB)
- N-body simulations
- Brilliant agreement of the CMB and SN Ia data
- Nucleosynthesis theory

In the following some of them are briefly explained in a historical approach.

1.3.1. Dynamics of Galaxies

Giving further support for Zwicky's hypothesis, Vera Rubin confirmed in 1970 ([7]) the non-Keplerian profile of rotation velocities for a huge number of galaxies (starting with the Andromeda Galaxy) using optical spectroscopy, where she uncovered the discrepancy between the predicted angular motion of galaxies and the observed motion, and thereby obtained the strongest evidence up to that time for the existence of dark matter.

By setting the gravitational force (F_G) and the centrifugal force (F_Z) equal, describing the circular movement of a star around the galactic centre, the rotational velocity $v=v(r)$ of an object on a stable Keplerian orbit in dependence of the radius r of its orbit can be calculated (in the context of classical Newtonian gravitation - connecting of the angular velocity of an orbiting satellite around a mass in a virialized system) like:

$$F_G = \frac{GmM}{r^2} = \frac{m \cdot v^2}{r} = F_Z \quad (9)$$

$$\Rightarrow v(r) = \sqrt{\frac{G \cdot M}{r}}, \quad (10)$$

with M being the mass within the orbit and G the gravitational constant - $G \approx 6.674 \cdot 10^{-11} \text{ N} \frac{\text{m}^2}{\text{kg}^2}$.

Thus, for stars well outside the (luminous) galactic body, one would expect the velocity to follow a Keplerian behaviour, i.e.

$$v(r) \propto \frac{1}{\sqrt{r}} \quad (11)$$

if only visible matter would be present.

In observations from 1980 (V. Rubin et al. [8]) individual stars or star clusters were measured to establish the velocity curve of a given galaxy, i.e. the circular velocity around the galactic center as function of the radius r (eq. (10) and (11)) of the orbit. A flat rotation curve even well beyond the galactic body was observed in systematic measurements of rotation curves for 21 galaxies and no single curve followed the expected Keplerian behaviour.

The orbital speed of a star or gas cloud around the Galaxy is determined by mass inside the orbit. Therefore it is needed to calculate the mass inside the Sun's orbit. This can be done via Kepler's Law:

$$M_{total} \propto \frac{(\text{orbital size})^3}{(\text{orbital period})^2} \quad (12)$$

Rubin's results showed, that if the gravity of the constituent stars was all that was holding the galaxies together, they would rupture because of their fast rotation velocity. But as they are not flying apart, a huge amount of unseen, non-luminous mass must be holding them together, at least ten times as much dark mass as can be accounted for by the visible stars. This phenomenon became known as the *galaxy rotation problem*. Rubin's observations indicated, that not just galaxy-clusters, but also individual galaxies contain dark matter, and were the first robust results to suggest that either Newtonian gravity does not apply universally, or that, conservatively, upwards of 50% of the mass of galaxies was contained in the dark galactic halo.

A comparison of the rotation curve of the typical spiral galaxy M33 predicted from the distribution of the visible matter and the above mentioned results from the observations of Volders and Rubin is represented in figure 1.

Dark halo

Implying the existence of a dark halo (i.e. a mass distribution made by non-luminous and non-absorbing matter) with a mass density $\rho(r) \propto \frac{1}{r^2}$ (eq. (13) and (14)) the observed deviation from the Keplerian velocity curves can be explained and was first done by J. Einasto et al. [10] and J.P. Ostriker et al. [11], stating that dark matter in galaxy clusters is not homogenous distributed throughout the cluster, but clustered around the individual galaxies, resulting in dark halos around the luminous part of the galaxies. [5]

With $M = \rho \cdot V$ assuming a spherical distribution of matter with a constant density ρ and $V = \frac{4}{3}\pi r^3$ and eq. (11) one gets:

$$v(r) = \sqrt{\frac{GM}{r}} = \sqrt{\frac{G \cdot \rho \frac{4}{3}\pi r^3}{r}} = r \sqrt{G\rho \frac{4}{3}\pi}, \quad (13)$$

or

$$\Rightarrow \rho = \rho(r) = \frac{3}{4} \frac{v^2}{G\pi} \cdot \frac{1}{r^2}. \quad (14)$$

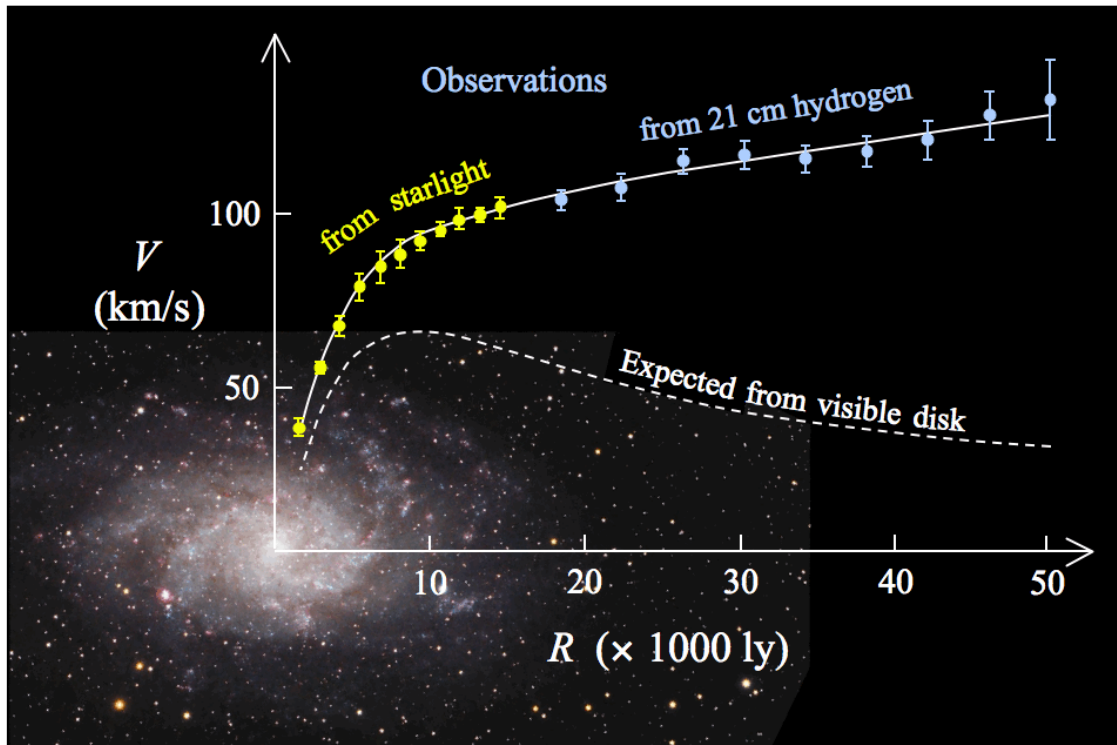


Figure 1: Rotation curve of the typical spiral galaxy M33 (yellow and blue points with error bars) and the predicted one from distribution of the visible matter (white line). The discrepancy between the two curves is accounted for by adding a dark matter halo surrounding the galaxy. [9]

Measurements of numerous spiral galaxies return, that $v(r) \propto \text{constant}$ for a test mass m being within the spherical distribution of density ρ . To explain this a massive halo (10:1; mass ratio halo to baryonic matter) is required (a comparison of the Milky Way and its DM-halo can be seen in fig. 37 on page 111).

In figure 2 a measurement from 1985 of the circular speed $v(r)$ as a function of the radius r for the barred spiral galaxy NGC 3198 shows, that for large r ($r > 10$ kpc) the velocity is almost constant and thus requests additional non-luminous gravitational matter.

Astronomers discovered, that the galaxy VIRGOHI21 practically totally consists of dark matter, observing nearly no stars, only 21 cm hydrogen-line emission and found that hydrogen is rotating, what can only be explained by a ratio of the hydrogen mass (M_H) to the total mass of $M_H/M_{total} \approx 1/10^3$. [12] Also recent discoveries, like properties of the longer known galaxy Dragonfly 44 (with W.M. Keck Observatory and the Gemini North telescope, both in Hawaii), which is located in the nearby Coma constellation and is a diffuse "blob" about the size of the Milky Way showed, that only one-hundredth of 1% is in the form of stars and "normal" matter. The other 99.99% is in the form of dark matter. [13] This would suggest the long theorized existence of dark galaxies, but there are no confirmed dark galaxies to date.

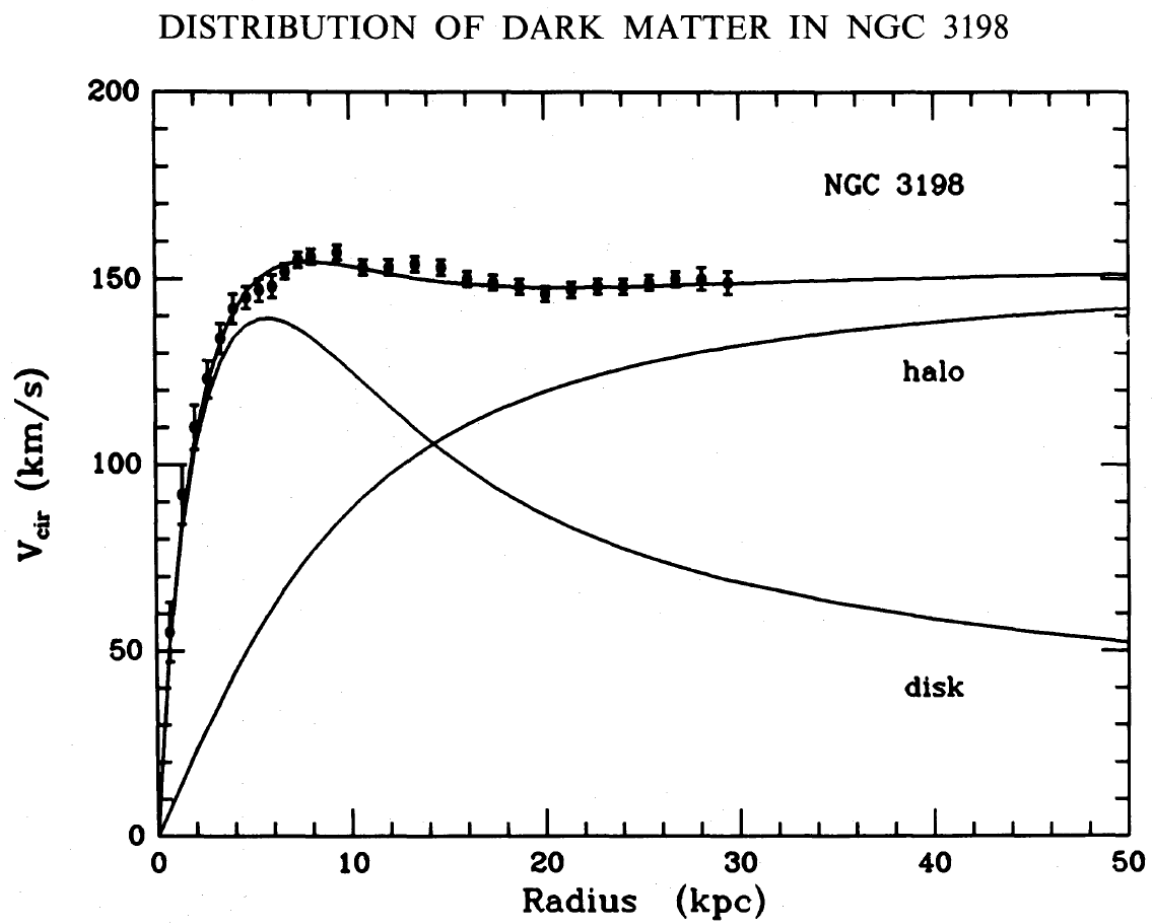


Figure 2: The velocity distribution for the barred spiral galaxy NGC 3198. The dots from the measurement indicate a massive halo, the lines correspond to models with contributions from a halo or a disk. [14]

Effects on the solar system

One question to these findings is, why the influence from dark matter has not been seen at observing the solar system. The influences from these non-luminous gravitational pulling matter becomes noticeable just on the very large scales, it hardly effects the solar system \odot , where the mass is completely dominated by baryonic matter, what is shown in the following calculations (eq. (15) to (17)) and in figure 3.

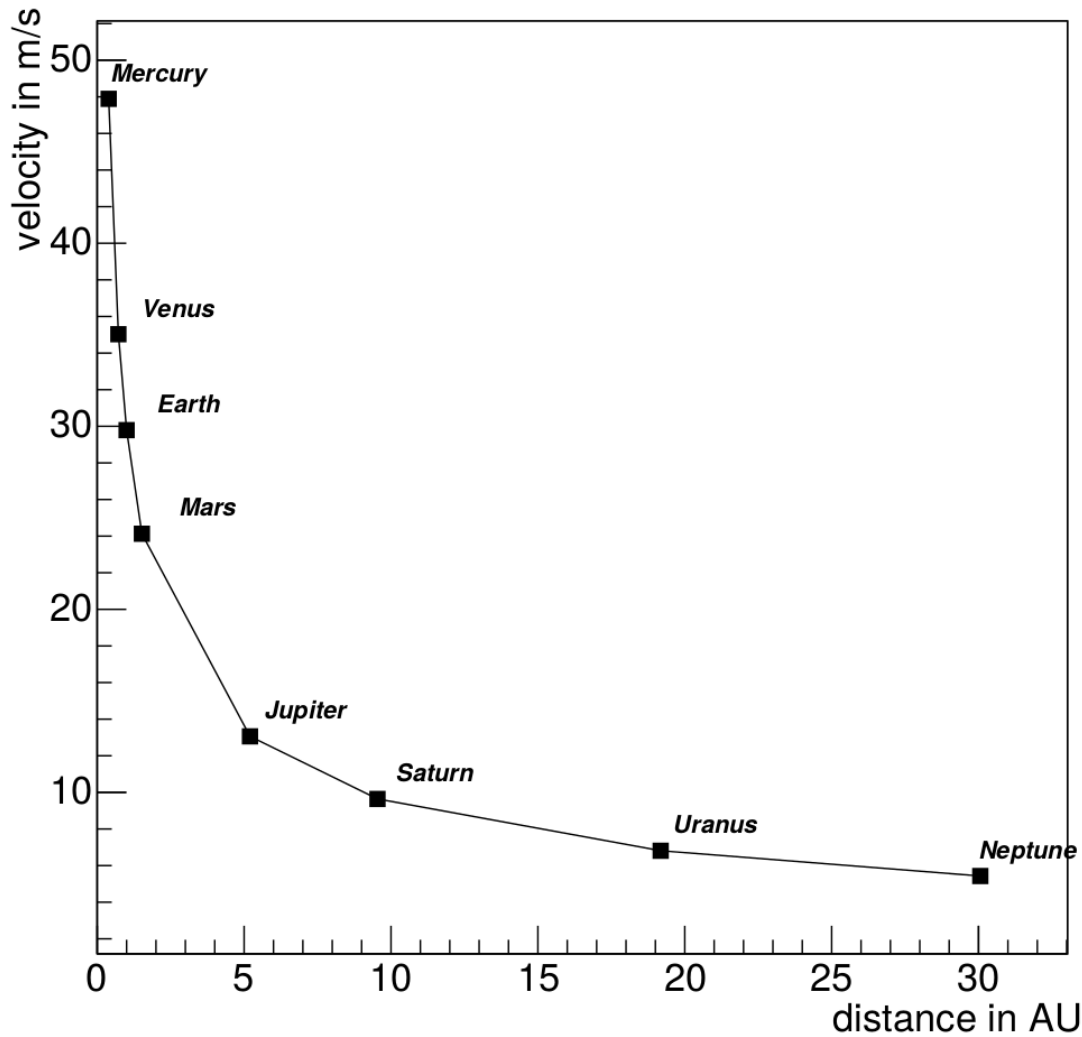


Figure 3: Velocity distribution of the planets within our solar system with the nice $v \propto \frac{1}{\sqrt{r}}$ distribution. [5]

This can easily be explained with a simple estimated model, describing the influence of dark matter inside the orbit of the earth. Taking the distance from Earth to the Sun of $1 \text{ AU} \approx 150 \cdot 10^{11} \text{ m}$ (astronomical unit), with the diameter of the earth of $\approx 13 \cdot 10^6 \text{ m}$ one gets a volume of

$$V = \pi AU^2 \cdot 13 \cdot 10^6 \text{ m} = \pi \cdot (150 \cdot 10^{11} \text{ m})^2 \cdot 13 \cdot 10^6 \text{ m} \approx 9 \cdot 10^{33} \text{ m}^3 . \quad (15)$$

The nowadays known dark matter density ρ_{DM} of the galactic halo of the Milky Way from measurements (from indirect DM detection 1.7.2, and simulations), is $\rho_{DM} = 0.3 \text{ GeV}/\text{cm}^3$ for the solar neighbourhood ($1 \text{ eV} = 1.602176565 \cdot 10^{-19} \text{ J}$), or via $E = m \cdot c^2$ (the mass equivalent of $1 \text{ eV}/c^2 = 1.782662 \cdot 10^{-36} \text{ kg}$) this can be converted to

$$\rho_{DM} = \frac{0.3 \cdot 10^9 \cdot 1.8 \cdot 10^{-36} \text{ kg}}{(10^{-2})^3 \text{ m}^3} \approx 0.5 \cdot 10^{-21} \frac{\text{kg}}{\text{m}^3} . \quad (16)$$

Therefore the mass of DM between the sun and earth (m_{DM-SE}) can be approximated to

$$m_{DM-SE} = \rho_{DM} \cdot V = 0.5 \cdot 10^{-21} \frac{\text{kg}}{\text{m}^3} \cdot 9 \cdot 10^{33} \text{ m}^3 = 4.5 \cdot 10^{12} \text{ kg} . \quad (17)$$

Comparing this result on m_{DM-SE} with the mass of the sun $m_{\odot} \approx 2 \cdot 10^{30} \text{ kg}$ and noticing the difference in a magnitude of 10^{18} it becomes clear, why the influence on these scales is negligible and thus there is no deviation from Keplerian behaviour.

Dark matter distribution

In literature many different approaches to the actual distribution of dark matter density ρ_{DM} are discussed, e.g. iso-thermal halos, tri-axial halos, etc. There are some popular distributions like the Einasto profile, Sérsic profiles, and one in the following equations briefly outlined model is the Navarro-Frenk-White (NFW) model [15], which can be parametrized as

$$\rho_{DM} = \frac{\rho_0}{\left(\frac{r}{R}\right)^{\gamma} \cdot \left[1 + \left(\frac{r}{R}\right)^{\alpha}\right]^{(\beta-\gamma)/\alpha}} , \quad (18)$$

with

$$\alpha = 1.0, \beta = 3.0, \gamma = 1.0, R = 20 \text{ kpc} , \quad (19)$$

with the dark matter density of the halo ρ_0 and a characteristic scale R . It is used also in fig. 2. [5]

The Navarro–Frenk–White (NFW) profile is a spatial mass distribution of dark matter fitted to dark matter haloes identified in N-body simulations by Julio Navarro, Carlos Frenk and Simon White, and is one of the most commonly used model profiles for dark matter halos. Alternative models, in particular the Einasto profile, have been shown to represent the dark matter profiles of simulated halos as well as or better than the

NFW profile. Because of the limited resolution of N-body simulations, it is not yet known which model provides the best description of the central densities of simulated dark-matter halos. The NFW dark matter profile is not consistent with observations of low surface brightness galaxies, which have less central mass than predicted. This is known as the *cusp-core* (or *cuspy halo*) *problem* (see sec. 1.6.1).

1.3.2. Gravitational Lensing

Further evidence for dark matter was delivered by the effect of (weak) *gravitational lensing*. As already supposed by Isaac Newton, Newtonian gravity predicts that starlight will bend around a massive object. A little bit more detail on space time etc. will be given in section A.3, but for now it is sufficient to mention, that the trajectory of light is always a geodesic for a given space time. As energy can curve the space time, it can also affect the light trajectory. This principle is illustrated in fig. 4: A massive object between a light source (here a distant galaxy) and an observer can bend the light trajectory like an optical lens, hence this effect is called gravitational lensing. As consequence of the bended light trajectory, the position of the distant object is changed for the observer and the image of an extended object get distorted.

After Albert Einstein predicted (in 1915) with his theory of general relativity, that the deflection angle, due to gravitational lensing, was twice the Newtonian prediction, it was A. Eddington [16] during the total eclipse in 1919, who made Einstein and his theory world-famous, by verifying this. He measured, that the position of stars near the eclipsed Sun where changed with respect to their position in absence of the Sun (i.e. at night).

The deflection angle $\hat{\alpha}$ can be calculated from the mass M of the lens and the impact parameter ζ [18] via:

$$\hat{\alpha} = \frac{4GM}{c^2\zeta}, \quad (20)$$

with the speed of light c and the gravitational constant G , see also fig. 4.

Nowadays it is distinguished between three classes of gravitational lensing, according on the strength of the effect:

1. Strong gravitational lensing - where the image is split
2. weak gravitational lensing - no clearly visible distortion of the image occurs
3. Microlensing - is a strong lensing event, in case the lens is small, e.g. a massive astrophysical compact halo object (MACHO) - see section 1.3.4 on page 29.

ad 2.:

The distortions of background sources are much smaller, and no obvious distortion of the image of an individual source is observed, but it is possible due observing multiple

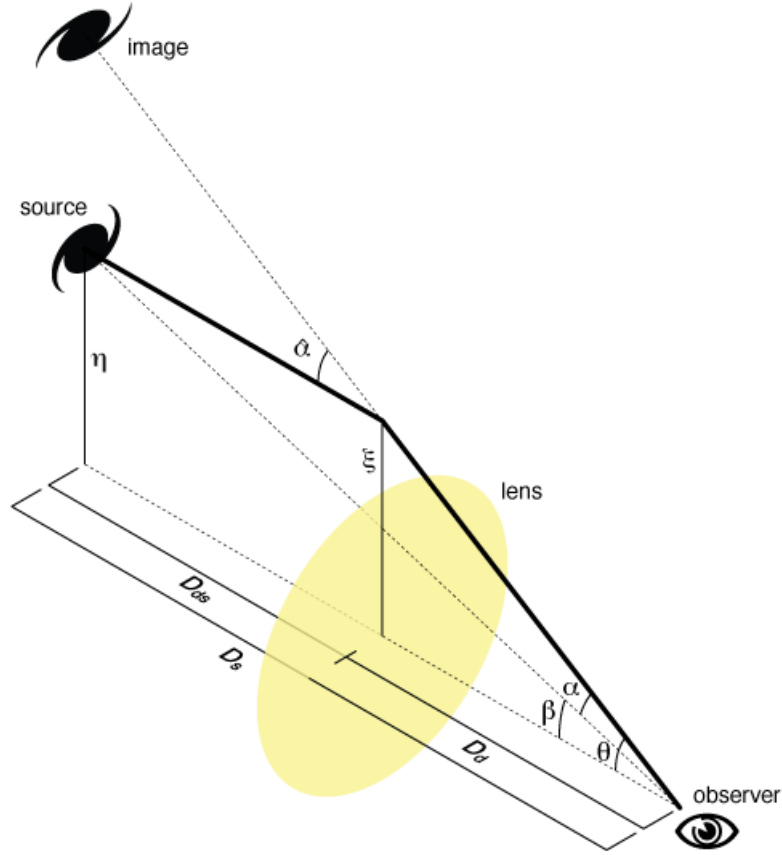


Figure 4: A lens of mass M will deflect light from a distant source by an angle $\hat{\alpha}$ dependent on the impact parameter ζ . [5] [17]

sources, to statistically deduce the correlation between the images (due to the gravitational lensing). Because of this use of multiple sources, more extended gravitational lenses can be studied, e.g. cosmic filaments or colliding galaxy clusters.

By measuring the shapes and orientations of large numbers of distant galaxies, their orientations can be averaged to measure the shear of the lensing field in any region. Based on the observed ellipticities a shear map can be constructed. This, in turn, can be used to reconstruct the distribution of gravitational interacting matter between source(s) and observer:

in particular, the background distribution of dark matter can be reconstructed (over density - and in contrary an under density between source and observer, e.g. a void).

But the results of these surveys are also important for cosmological parameter estimation, to better understand and improve upon the Λ CDM model (see section 1.4), and to provide a consistency check on other cosmological observations. They may also provide an important future constraint on dark energy.

The effects of both, the strong and the weak gravitational lensing, shows for galaxy

clusters more gravitational interacting matter than luminous matter. The differences can be explained as dark matter and is in agreement with the results obtained from dynamics of galaxies (discussed in the previous section), but this is not just an additional indication for dark matter, with gravitational lensing, it is also possible to map the distribution of dark matter in comparison with luminous matter, see e.g. fig. 5 for the famous "Bullet cluster".

Gravitational lenses act equally on all kinds of electromagnetic radiation, not just visible light. Weak lensing effects are being studied for the cosmic microwave background (see section 1.3.3) as well as galaxy surveys. Strong lenses have been observed in radio and X-ray regimes as well.

Bullet Cluster

The bullet cluster (1E 0657-558) consists actually of two well separated colliding galaxy clusters observed in 1 billion pc away from Earth, and passed through 150 million years ago. The name Bullet Cluster refers to the smaller subcluster, moving away from the larger one and looks like a bullet passing through a target.

It was found per measurements from weak lensing, that the visible mass accounts for only $\lesssim 2\%$ of its total mass [19] and therefore the existence of dark matter is needed.

Furthermore the bullet cluster allows also to investigate the nature of its dark matter, i.e. if it is *non-baryonic* dark matter or *baryonic* dark matter (see section 1.8). A classic candidate for non-baryonic dark matter in galaxy clusters is the intergalactic medium (see appendix A.5), i.e. hot gas not associated with individual galaxies but with the total cluster [20].

The Bullet Cluster is one of the hottest known clusters of galaxies. Investigating this collision one can discriminate three parts:

- The stars of the galaxies, observable in visible light, were not greatly affected by the collision, and most passed right through, gravitationally slowed but not otherwise altered.
- Observations in X-ray found the hot gas of the two colliding components. It is located in-between the two subclusters and represents most of the baryonic (i.e. ordinary) matter in the cluster pair, but it contributes only $\lesssim 15\%$ to the total cluster mass. The gases interact electromagnetically, causing the gases of both clusters to slow much more than the stars.
- The third component, indirectly detected by the (weak) gravitational lensing of background objects is the dark matter.

By interpenetrating each other, the galaxies of each subcluster where not distorted, due to the large distances between it. Contrary, the extended gas around each subcluster was separated from the galaxies by friction. [19]

The weak-lensing, which is strongest in two separated regions near (possibly coincident with) the visible galaxies, showed that most of the cluster mass coincide with the subclusters. Therefore, baryonic dark matter is only a minor contribution to the mass budget of the bullet cluster and provides support for the idea that most of the mass in the cluster pair is in the form of two regions of dark matter, which bypassed the gas regions during the collision and lies ahead of the collisional gas, see fig. 5. Non-baryonic dark matter could be a solution for the missing major contribution. [19]

Additional, this potential *non-baryonic* mass must have a *low self-interaction cross-section*, because otherwise friction would have separated it from the galaxies as it coincide (similar to the intergalactic mediums). This together with the observation of several other merging clusters could set limits on the self-interaction cross-section. [21].

This (and other similar observations) allow good limits on the cross-section of the self-interaction of dark matter ([21]) and provides an observable constraint for cosmological models, which may diverge at temperatures beyond their predicted critical cluster temperature ([22]).

A study from 2010 has concluded that the velocities of the collision as currently measured are "incompatible with the prediction of a Λ CDM model" (discussed in section 1.4) [23], and it may indicate that the prevailing cosmological model is insufficient to describe the mass discrepancy on galaxy scales, or that its predictions about the shape of the universe are incorrect.

In theories without dark matter, such as Modified Newtonian Dynamics (MOND), the lensing would be expected to follow the baryonic matter (i.e. the X-ray gas). Since the observation of the bullet cluster, shown in fig. 5, the MOND approach lost its validity as substitute for the existence of dark matter. (However, small MOND effects on top of non-baryonic dark matter are not excluded.) These obstacles may be solved by even more generalized modifications, e.g. *Modified Gravity* (MOG) which introduce a position dependent gravitational coupling to explain the Bullet Cluster. [24]

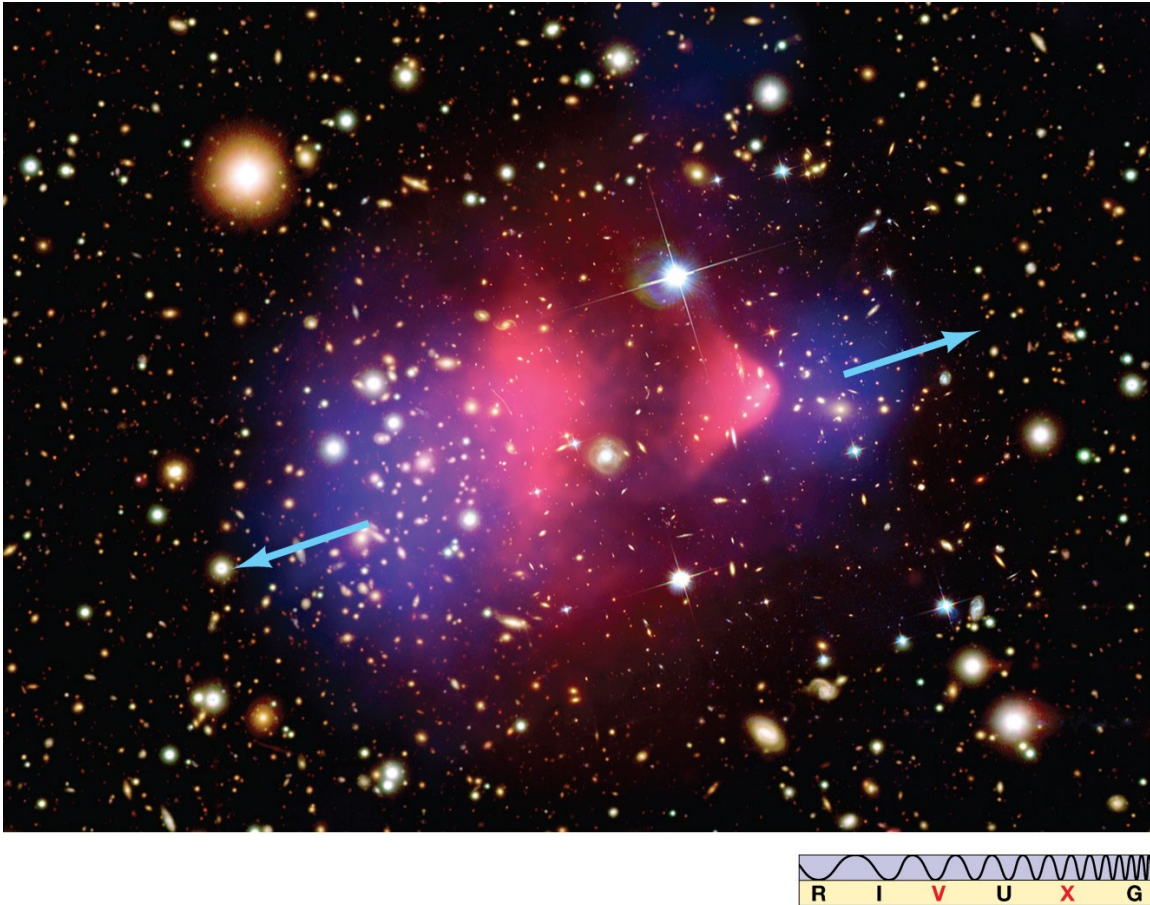


Figure 5: Composite picture of the bullet cluster. Optical image of the Bullet Cluster (1E 0657-558), overlaid with a X-ray observation (red) and a lensing map (blue). For details see text. Credit: X-ray: NASA/CXC/CfA/M.Markevitch et al.; Optical: NASA/STScI; Magellan/U.Arizona/D.Clowe et al.; Lensing Map: NASA/STScI; ESO WFI; Magellan/U.Arizona/D.Clowe et al. [19] [25]

1.3.3. Cosmic Microwave Background

After G. Gamow, R. Herman and R. A. Alpher first predicted it in 1948, it was discovered by A. Penzias and R. Wilson in 1965 with the Holmdel horn antenna. The most precise observation of the **Cosmic Microwave Background (CMB)** power spectrum (fig. 8) was done with the PLANCK satellite ((Re)Named in honour of the German physicist Max Planck (1858-1947), who derived the formula for black-body radiation.), which was a space observatory operated by the European Space Agency (ESA) from 2009 to 2013. It mapped the anisotropies of the CMB (fig. 7) at microwave and infra-red frequencies, with high sensitivity and small angular resolution and provided a major source of information relevant to several cosmological and astrophysical issues, such as testing theories of the early Universe and the origin of cosmic structure. As of 2013 it has provided the most accurate measurements of several key cosmological parameters, including the average density of ordinary matter and dark matter in the Universe and with an expanded release including polarization data in February 2015.

Planck's objective is to analyse, with the highest accuracy ever achieved, the remnants of the radiation that filled the Universe immediately after the Big Bang - this is observed today as the Cosmic Microwave Background.

Properties

Alluding to its Wien peak in the microwave region, it shows the wavelength dependence of a "blackbody" radiator at about 3 K temperature today.

All objects emit radiation with the wavelengths characteristic of their temperature. The ≈ 380000 year old universe was a 3000 K blackbody (fig. 11), with its peak wavelength = 1 micrometer = 10^{-6} m, releasing this microwave radiation. Looking across space today it is glowing with 1 millimetre = 10^{-3} m. This shift of the spectrum of the cosmic microwave background from 3000 K to 3 K is an enormous redshift, named *cosmological redshift*.

Before the decoupling, photons and electrons were coupled via Thompson scattering. Electrons and protons were coupled via charge conservation. Matter got compressed during fall into the gravitational well, resulting in temperature increase. Radiation pressure increased with temperature, and radiation pressure rarefied matter again, resulting in temperature decrease. A consequence are acoustic oscillation with wavelength λ and higher harmonics. This process stops at recombination.

So this "light" which is detected now originated in the very early universe, in an age then about 380000 years or nearly 13.7 billion years ago and is considered to be the remnant of the radiation emitted at the time the expanding universe became transparent. This decoupling of γ took place at a temperature of about 3000 K, at a redshift z of about $z = 1100$ (*last scattering surface*), and a time when the universe was $t = 380000$ years old (the redshift z is related to the distance d by Hubble's law eq. (6)). Till then all matter was in plasma (protons and electrons separated) and light could not pass through, but then the microwave radiation decoupled from baryonic matter and the universe transforms from being opaque in the plasma to being transparent. This is called the *Era*

of *Recombination*, because the expansion of the Universe cools the plasma, protons and electrons combined and formed neutral hydrogen and helium atoms, photons decouple and so light could pass through and travelled in all directions and can be observed as cosmic microwave background (CMB) radiation. A representation of the composition at this time can be seen in fig. 6. The redshift is determined by eq. (4). From the measured blackbody temperature the photon number n_γ and the energy density ρ_γ can be calculated at the epoch of recombination to $n_\gamma = (2\zeta(3)/\pi^2)T_\gamma^3 \simeq 411 \text{ cm}^{-3}$ and the energy density is given by $\rho_\gamma = (\pi^2/15)T_\gamma^4 \simeq 0.260 \text{ eV cm}^{-3}$.

This microwave radiation is still here to today and penetrates the entire universe in the guise as an almost perfect black body radiation at $T = T_\gamma = 2.735 \text{ K}$. This is due to the expansion of space, as the universe expands, the wavelength of primordial light also increases. (redshift)

Also the discovery of the 3 K microwave background radiation was one of the crucial steps leading to the calculation of the standard "*Big Bang*" model of cosmology.

It is nearly the same in all directions, but slightly asymmetric ($\approx 0.1\%$), due a local Doppler shift due to the earth's motion. It is called CMB "dipole" and is visible because of our local group's relative speed to this primordial radiation ($\approx 600 \text{ km/s}$). Observations revealed, that the Sun moves at 382 km/s , the Milky Way at 540 km/s and that the Milky Way Galaxy is moving toward the Hydra-Centaurus Supercluster and this in turn toward the Great Attractor (many clusters are moving in this direction - enormous pull).

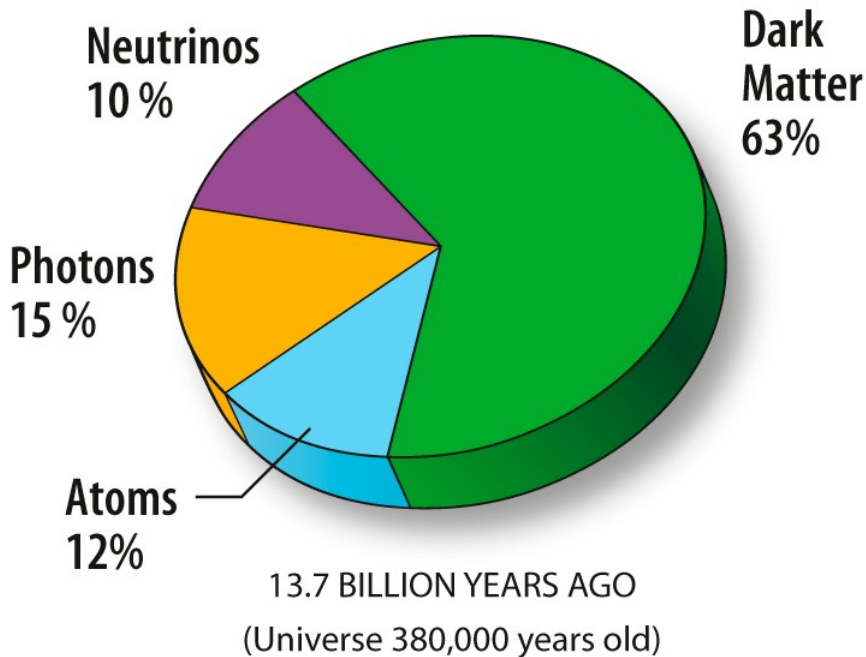


Figure 6: Content of the universe at an age of 380000 a.

Observations of the anisotropy of the CMB from temperature fluctuations showed, that it is *homogeneous* (the universe looks the same everywhere on large scales - there is

no special place (center)) and *isotropic* (the universe looks the same in all directions on the sky - there is no special direction (axis)). This behaviour got the notion *cosmological principle* and describes the distribution of matter in the universe, when viewed on a large enough scale, since the forces are expected to act uniformly throughout the universe, and should, therefore, produce no observable irregularities in the large scale structuring over the course of evolution of the matter field that was initially laid down by the Big Bang (more on that see the following section 1.3.4).

Temperature variations in the cosmic background radiation are a record of sound waves in the early universe - called *Primordial sound waves*. Studying the character of these sound waves, and the polarization of the background radiation that they produce, helps constrain models of the universe. The three major peaks (in fig. 8) show the relative contributions of dark energy, ordinary matter, and dark matter.

The high degree of uniformity throughout the observable universe and its faint but measured anisotropy lend strong support for the Big Bang model in general and the Λ CDM ("Lambda Cold Dark Matter", see section 1.4) model in particular.

Further details of the CMB verified, that the cosmological principle holds. Planck creates a very detailed picture of the microwave radiation, and the content of this image tells us much about the fundamental structure of the universe:

- If the Universe was denser and hotter in the past, there should be leftover heat from the early Universe. The CMB (the afterglow from the Big Bang) is homogeneous to 1 part in 10^5 (anisotropic \approx at the mK-level), a very direct evidence for the cosmological principle to hold.
- the age of the universe is 13.8 billion years (with less than 0.1% (1/1000) uncertainty); If the expansion rate of the universe $H = \frac{\dot{R}}{R}$ was constant H_0 , the age of the universe could be computed as (eq. (5))

$$t_{Hubble} = \frac{d}{v} = \frac{1}{H_0}. \quad (21)$$

It is shown later, that the H is not constant with time. Taking this into account ends up with the age of the universe of about 14 billion years.

- the total energy-mass density Ω_0 ("Omega nought") is very close to 1.00 (less than 1% uncertainty) in other words, the universe is flat (eq. (26)); The radius of the observable universe is determined by the distance to the optical horizon, beyond which no light signals could reach the Earth at the present time. If the universe was static, flat:

$$d_{Hubble} = c \cdot t_{Hubble} = \frac{c}{H_0} \approx 4.2 \text{ Gpc} \quad (22)$$

But the expansion of the universe enlarges this number, such that (under reason-

able assumptions) the radius of the observable universe is

$$H \approx 3.3 \frac{c}{H_0} \approx 14 \text{ Gpc} \approx 45 \text{ Gly} . \quad (23)$$

- The Universe recombined at $z \simeq 1100$ and re-ionized at $z \simeq 10$. This sets the times when the CMB formed and when the first stars formed, respectively. (Observations of galaxies today seem to indicate that most of the volume of the intergalactic medium (IGM) consists of ionized material (since there are few absorption lines due to hydrogen atoms). This implies a *period of re-ionization* during which some of the material of the universe was broken into hydrogen ions.)
- the fractions (Ω_x) of ordinary matter, dark matter and dark energy - fig. 9, definition and brief explanation see eq. (24), (25) and (27) and the following text;

Due to this precise measurements and fit (of the observed power spectrum) with the Λ CDM model, with results ([26]) in $\Omega_b \approx 0.049$ and $\Omega_m \approx 0.314$, clearly indicates the existence of non-baryonic dark matter in the universe via the difference $\Omega_m - \Omega_b \approx 0.265 = \Omega_{dm}$.

The thereby current average density of ordinary matter and dark matter (and dark energy - brief see page 25) in the Universe can be seen in figure 9.

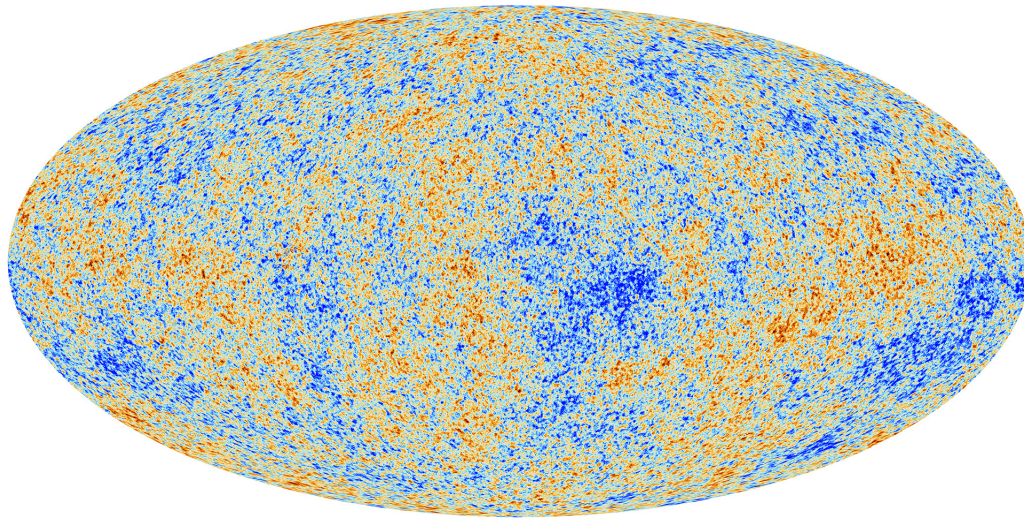


Figure 7: The anisotropies of the Cosmic microwave background (CMB) as observed by Planck. The CMB is a snapshot of the oldest light in our Universe, imprinted on the sky when the Universe was just 380 000 years old. It shows tiny temperature fluctuations that correspond to regions of slightly different densities, representing the seeds of all future structure: the stars and galaxies of today. [27]

It is convenient to express the abundance of a substance Ω in the Universe in units of ρ_{crit} (more to this see appendix A.3), or in other words to express the density as a

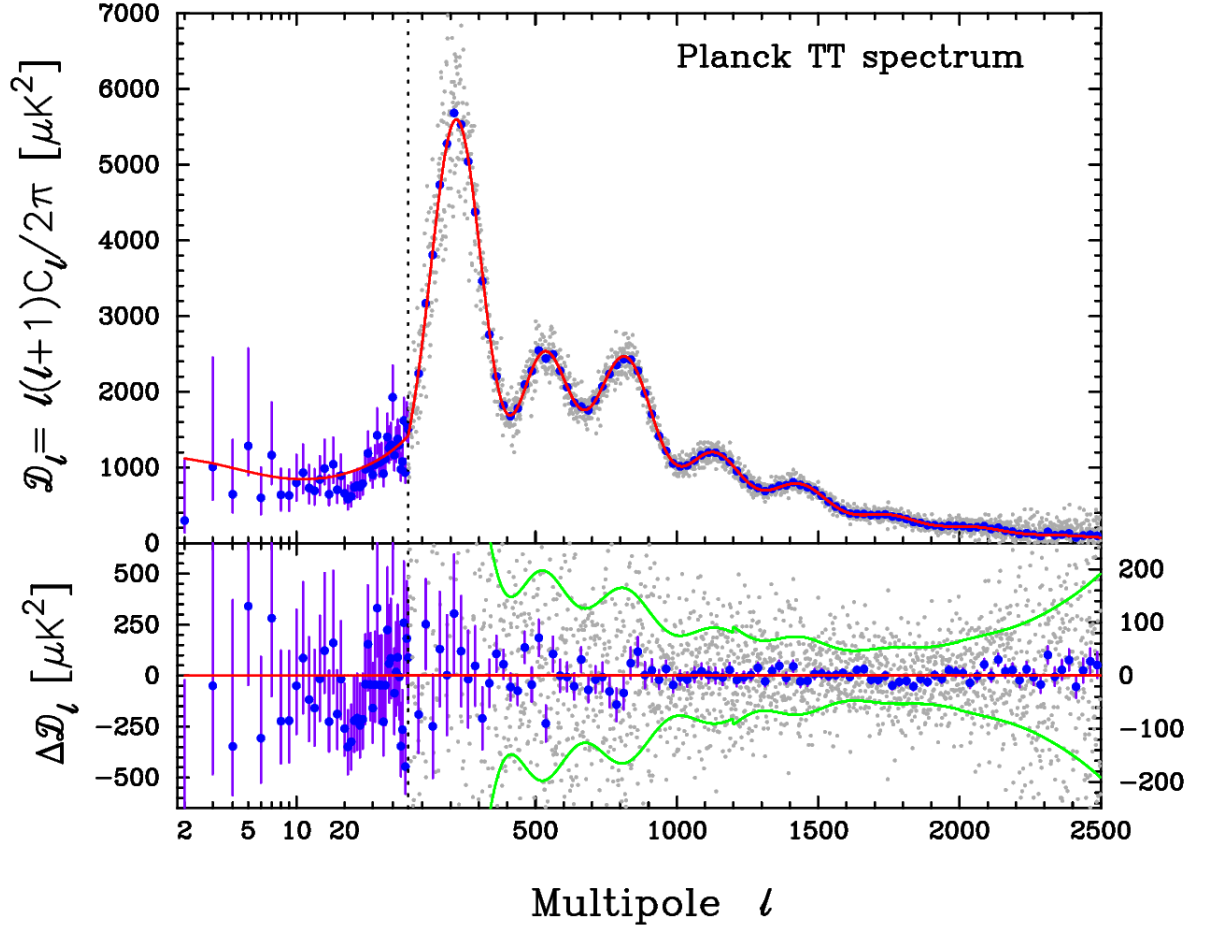


Figure 8: The TT power spectrum of the CMB anisotropies as measured by PLANCK. On the upper panel on the vertical axis the band-power estimates \mathcal{D}_l in μK^2 are shown, while the lower panel shows the residuals between measurement and model. The uncertainties include both the statistical instrumental noise and cosmic variance. The red curve is the best-fit Λ CDM model to the data. On the horizontal axis the multipole moment l and the corresponding angular size are shown. Figure taken from [26].

fraction of the density required for the critical condition with the parameter $\Omega = \frac{\rho_x(t=t_0)}{\rho_{crit}}$ so that $\Omega = 1$ represents the condition of critical density (coming from the Friedmann equation - more see appendix). This leads to the definition:

$$\Omega = \sum_i \Omega_i \equiv \sum_i \frac{\rho_i}{\rho_{crit}} \quad (24)$$

It is standard to define the present-day density parameter Ω_x for various species as the dimensionless ratio

$$\Omega_x \equiv \frac{\rho_x(t=t_0)}{\rho_{crit}} = \frac{8\pi G\rho_x(t=t_0)}{3H_0^2}, \quad (25)$$

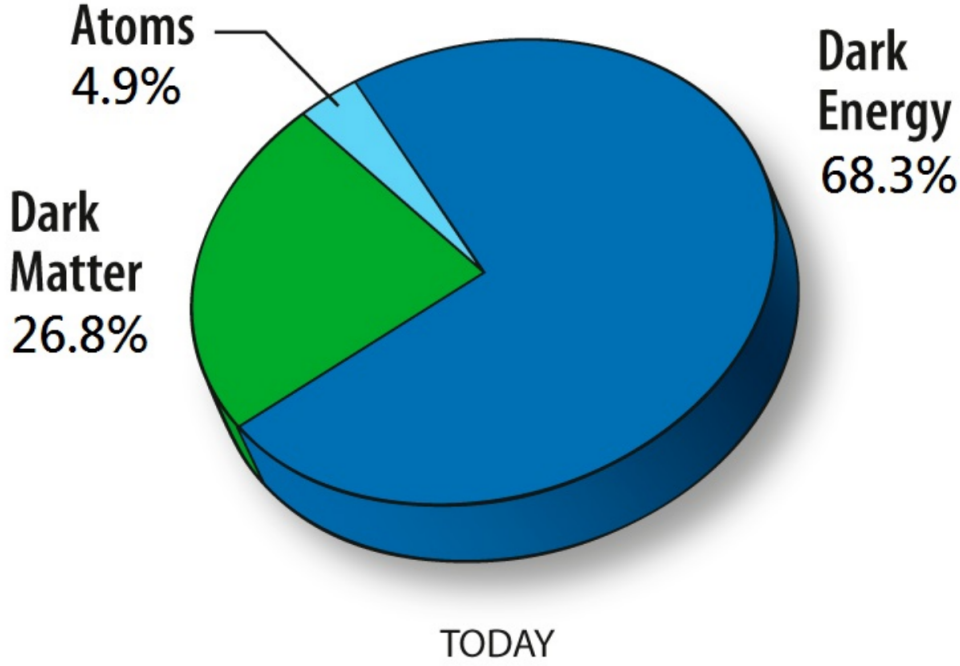


Figure 9: Energy matter density content of our current universe.

where the subscript x is one of "b" for baryons, "c" or "dm" for cold dark matter, "rad" for radiation (photons plus relativistic neutrinos), and "DE" or " Λ " for dark energy. It should be noted, that in general Ω is a function of time t , since both ρ and ρ_c depend on time. The present value of the density parameter is denoted $\Omega_0 = \Omega(t = t_0)$.

Observations show that the radiation density is very small today, $\Omega_{rad} \approx 10^{-4}$, and the Universe is matter dominated, $\Omega_m > \Omega_{rad}$ (see fig. 10).

In the minimal 6-parameter Λ CDM model (more see 1.4), it is assumed that curvature Ω_k is zero. The geometry of the Universe is close to flat as the density of the Universe matches the critical density very closely ($\Omega_0 = 1.003^{+0.013}_{-0.017}$) and the curvature is consistent with a flat universe ($k=0$) $\Omega_k = \frac{3kc^2}{8\pi Ga^2\rho_c} = 0$

$$\Omega_0 = 1 + \Omega_k, \quad (26)$$

with $\Omega_0 = \Omega + \Omega_\Lambda$ and $\Omega = \Omega_{rad} + \Omega_m$.

The total matter energy density is

$$\Omega_m = \Omega_{lum} + \Omega_b + \Omega_{dm} \quad (27)$$

and hence

$$\Omega_{rad} + \Omega_m + \Omega_\Lambda = 1, \quad (28)$$

in which the energy density contribution from radiation Ω_{rad} can be neglected, as mentioned before.

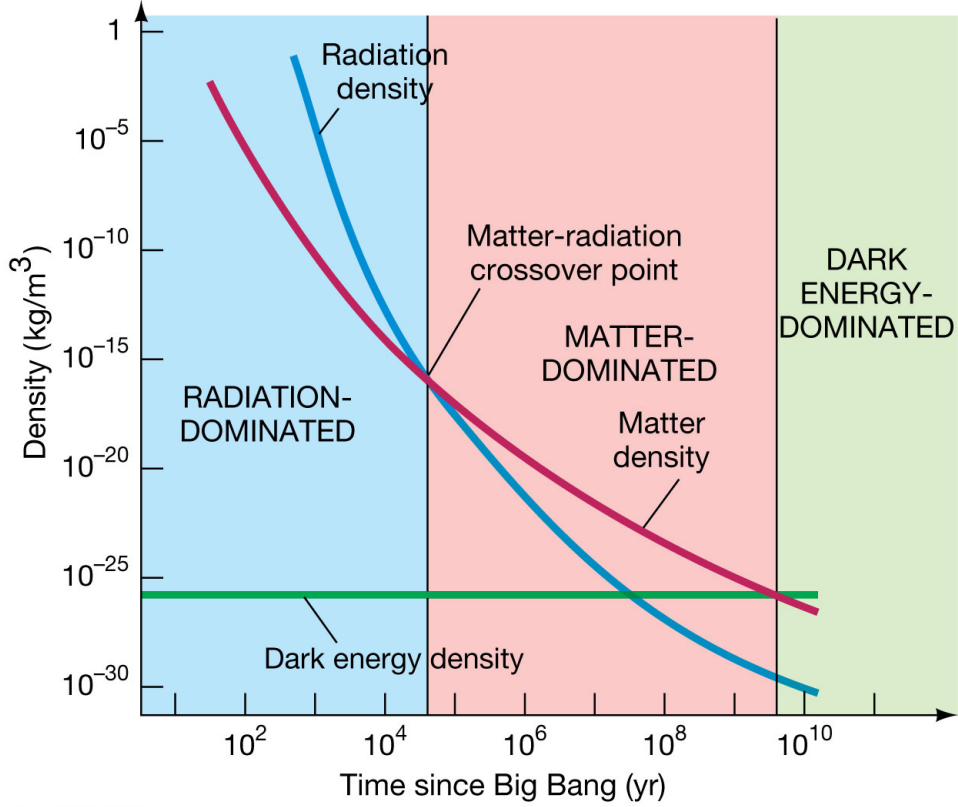


Figure 10: Evolution of density. [28]

Ω_{lum} , the energy contribution from luminous matter, is ≈ 0.01 , and the contribution from baryonic luminous matter, $\Omega_b \approx 0.049$. The energy density from the cosmological constant is determined to be $\Omega_\Lambda \approx 0.683$.

The radiation density can be split into two components, one for the photons and one for the neutrinos

$$\Omega_{rad} = \Omega_\gamma \cdot (1 + 0.2271 N_{eff}). \quad (29)$$

In the equation above, the photon energy density Ω_γ is related to the relativistic neutrino energy density of via the effective number N_{eff} of neutrino species which is set to its standard value 3.04. The effective number of neutrinos decreases to the physical number of neutrino, three, as the number of relativistic neutrinos declines. The non-relativistic neutrino density Ω_ν can be retrieved from the relation:

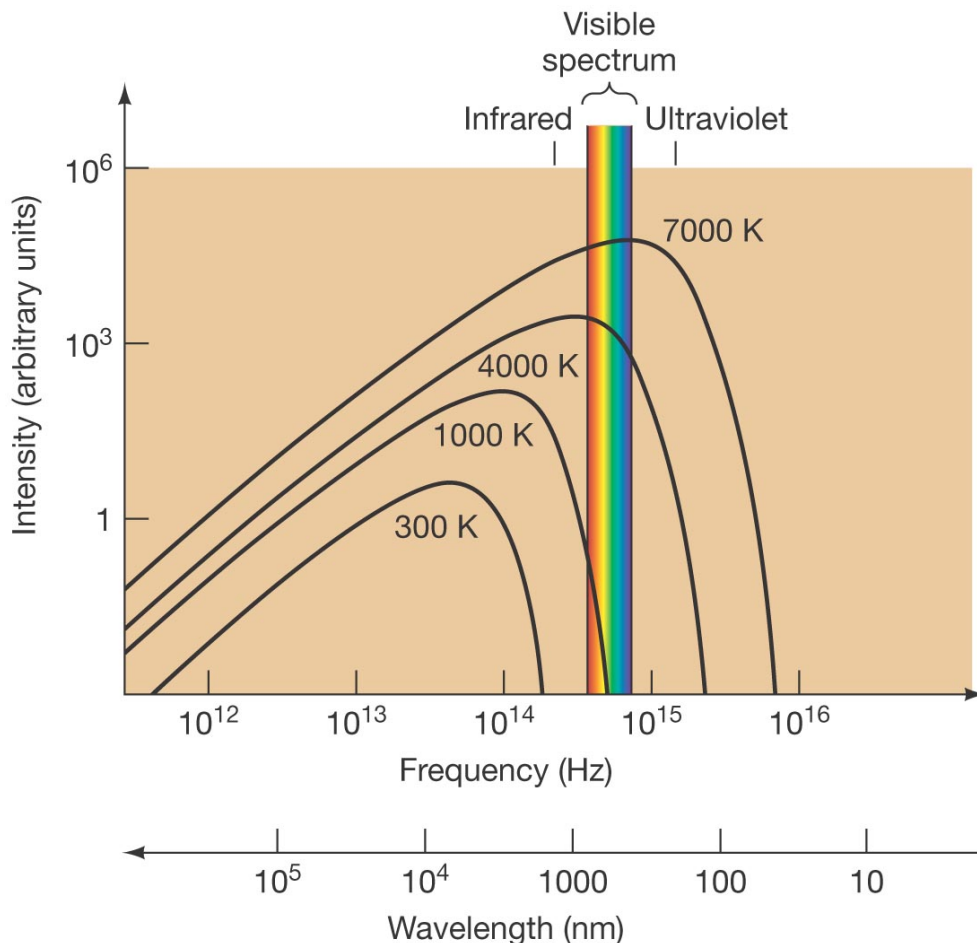
$$\Omega_\nu = \frac{\sum m_\nu}{94h^2 eV}. \quad (30)$$

After all this ascertainties, dark matter is described as being cold (i.e. its velocity is far less than the speed of light at the epoch of radiation-matter equality); non-baryonic (i.e. consisting of matter other than protons and neutrons); dissipationless (i.e. cannot

cool by radiating photons); and collisionless (i.e. the dark matter particles interact with each other and other particles only through gravity and possibly the weak force). The dark matter component (Ω_{dm}) is currently estimated to constitute about 26.8% of the mass-energy density of the universe.

The remaining 4.9% comprises all ordinary matter observed as atoms, chemical elements, gas and plasma, the stuff of which visible planets, stars and galaxies are made. As a matter of fact, the great majority of ordinary matter in the universe is unseen, since visible stars and gas inside galaxies and clusters account for less than 10% of the ordinary matter contribution to the mass-energy density of the universe.

Also, the energy density includes a very small fraction ($\approx 0.01\%$) in cosmic microwave background radiation, and not more than 0.5% in relic neutrinos. Although very small today, these were much more important in the distant past, dominating the matter at redshift > 3200 (fig. 10).



Copyright © 2008 Pearson Education, Inc., publishing as Pearson Addison-Wesley.

Figure 11: Spectrum of the blackbody radiation at different temperatures T . [29]

The power spectrum

The power spectrum, presented in figure 8, is sensitive to Ω_Λ , Ω_m and Ω_b . The anisotropy, or directional dependency, of the cosmic microwave background is divided into two types: primary anisotropy, due to effects that occur at the last scattering surface and before; and secondary anisotropy, due to effects such as interactions of the background radiation with hot gas or gravitational potentials, which occur between the last scattering surface and the observer. The structure of the cosmic microwave background anisotropies is principally determined by two effects: acoustic oscillations and diffusion damping (also called collisionless damping or Silk damping). These two effects compete to create acoustic oscillations, which give the microwave background its characteristic peak structure.

The angles subtended by the Hubble radius at last scattering correspond to a multipole moment of $l \simeq 100$. The anisotropies at larger scales have not evolved significantly and reflect the initial conditions at the epoch of recombination. The locations of the peaks also give important information about the nature of the primordial density perturbations. There are two fundamental types of density perturbations called *adiabatic* and *isocurvature*. A general density perturbation is a mixture of both, and different theories that purport to explain the primordial density perturbation spectrum predict different mixtures. The multipole modes in the range of 100 to 1000 contain the acoustic peaks of the anisotropy spectrum, which are a consequence of gravity-driven acoustic oscillations of the plasma before recombination. Perturbations within the horizon at last scattering had been able to evolve causally and produced the observed anisotropy at recombination. The frozen phases of these sound-waves imprint relations of the total matter density Ω_0 to the baryonic matter density Ω_b , giving the CMB anisotropies its constraining power on cosmological models.

The scale associated with the peaks is the sound horizon at last scattering, which size can be calculated from the first peak, which is sensitive to the density of baryonic matter Ω_b and Ω_Λ . The angular scale of the first peak determines the curvature of the universe (but not the topology of the universe). The sound horizon is the wave length of the base mode at decoupling and depends on Ω_m and Ω_Λ and is ≈ 150 Mpc. The distance to the last scattering surface d depends on the curvature of the universe. The projection of this length onto the sky yields an angular scale which is sensitive to the spatial curvature of the Universe and thus its total energy content, Ω_0 , if the Hubble constant is known.

The second peak is sensitive to Ω_b . More baryons result in a stronger compression and in a higher amplitude of the odd-numbered peaks in the power spectrum. The ratio between even and odd peaks, e.g. between first and second peak, is sensitive to Ω_b , since ratio of the odd peaks to the even peaks determines the reduced baryon density.

Higher peaks are sensitive to Ω_m . So the third peak can be used to get information about the dark-matter density. The time of transition from the radiation dominated epoch of the universe to the matter dominated epoch depends on Ω_m , e.g. for a smaller Ω_m , the transition happens later. In this case the decay of the gravitational wells by radiation is stronger, which affects the amplitude of all peaks.

For the search for dark matter, the CMB is important as it shows clearly that dark matter is not just an observable feature of today's Universe, but was present in the early Universe with observable unique consequences. The formation of the acoustic oscillation peaks requires Cold dark matter, as free-streaming relativistic Hot Dark Matter could not accredit.

Dark Energy

In the late 1990s, the measurement of the luminosity-distance relation of Type Ia supernovae led to the discovery, that the expansion of the Universe is accelerating, implying that most of the energy in the Universe is some exotic Dark Energy, characterized by its *negative* pressure-density ratio. This was confirmed by analysis of the microwave background anisotropies, and by massive surveys of galaxies like the Sloan Digital Sky Survey (SDSS). Both observations combined provided increasingly accurate values for cosmological parameters.

Horizon problem

To complete this (sub)section the horizon problem (sometimes called the homogeneity problem) shall be mentioned briefly.

With the discovery of this *isotropic* CMB in 1965, the *Horizon problem* became evident: As the particle horizon at the time of last scattering now has shrunk to an area about 1.6° in the visible background today, no physical influence could have smoothed out initial inhomogeneities in either a matter - or radiation - dominated Universe and thus bringing points separated by more than a few degrees at the time of last scattering to the same temperature. This contradicts the observation of a nearly perfect isotropy of the CMB at large angular scales.

So the horizon problem is a problem with the standard cosmological model of the Big Bang and points out, that different regions of the universe have not "contacted" each other because of the great distances between them, but nevertheless they have the same temperature and other physical properties. This should not be possible, given that the transfer of information (or energy, heat, etc.) can occur, at most, at the speed of light.

Two theories that attempt to solve the horizon problem are the theory of cosmic inflation and variable speed of light. In the beginning of the 1980s the proposal of the theory of inflation offered a solution to the Horizon problem among some other outstanding cosmological puzzles, and provided a mechanism for the origin of large-scale structure, which could be tested by the observation of anisotropies in the CMB.

1.3.4. Large Scale Structure

Even a little more details on the nature of dark matter can be attained by studying the evolution of the universe, the formation of large scale structures. From cosmology, the study of the structure and evolution of the entire universe, it is known, that the universe shows structure at many scales, as there are: subatomic particles, atoms, stars and planets, star clusters and galaxies, galactic cluster and superclusters, voids and sheets. The collection of data, such as of Galaxy Surveys has shown, that structure does end on the scale of greater than 200-300 Mpc (largest structure - Sloan Great Wall - nearly 300 Mpc across), but no evidence of any larger structures, or the Pencil-Beam Survey, which observed voids and sheets on scales of 100-200 Mpc, and also no indication of any larger structures.

Evolution

Structure formation refers to the serial transformations of the universe following the Big Bang. The universe, as is now known from observations of the cosmic microwave background radiation, began in a hot, dense, nearly uniform state approximately 13.8 billion years ago. The early radiation-dominated Universe is considered to be preceded by a different accelerating phase of the Universe known as *cosmic inflation*. This inflationary epoch in the early universe, with exponential expansion of space, lasted from $\approx 10^{-36}$ seconds after the Big Bang to sometime between 10^{-33} and 10^{-32} seconds and the temperature drops from 10^{27} K down to 10^{22} K. At present, it is known that the Universe is accelerating and thus is described by a vacuum- (or cosmological constant-) dominated Universe (see fig. 10). The evolution of the Universe can be described by the Einstein equations, which arise in general relativity, including matter fields and a cosmological constant (CC) Λ (more see appendix A.3).

Structure formation attempts to model how these structures of galaxies, galaxy clusters and larger structures formed by gravitational instability of small early density ripples and density fluctuations. During inflation the Universe became very flat and homogeneous with only small amounts of fluctuations. After inflation, the temperature returns to the pre-inflationary temperature; this is called *reheating* or thermalization because the large potential energy of the inflation field decays into particles and fills the Universe with SM particles, including electromagnetic radiation, starting the radiation dominated phase of the Universe. This oscillating inflation field briefly makes the Universe matter-dominated until its decay produces relativistic particles: the Universe is then *reheated* and thus begins the standard Big Bang Universe. For simplicity, it is usually assumed that the particles produced from inflation decay are thermalized instantly and the reheating temperature T_{reh} is defined as the temperature when the energy density of radiation dominates the matter density of the oscillating inflation field. That happens around a time comparable to the lifetime of the inflation field, $t \sim H^{-1}$, when the inflation energy density exponentially decreases. The reheating temperature can be derived from the Friedmann equation (see eq. (31)). To maintain the successful predictions for the abundances of light nuclei production during the standard Big Bang Nucleosynthesis

(BBN), it is required that $T_{reh} \gtrsim 4$ MeV. [30] Following the inflationary period, the Universe continues to expand, but at a less rapid rate. The early Universe after inflation was filled with relativistic particles in a plasma that was very hot and dense. The relativistic particles, collectively referred to as radiation, became thermalized due to their self-interactions thus reaching local thermodynamic equilibrium. What prevents small matter density fluctuations from collapsing is radiation, and (e.g. for a low-density gas of non-relativistic massive particles) the relation between the pressure and the energy density comes from the Equation of state: $p \cdot V = Nk_B T$.

So on very large scales (≈ 100 Mpc) the universe is homogeneous and isotropic, but at the next smaller distances (≈ 50 Mpc) this changes and voids and superclusters are observed. Prior to structure formation, e.g., Friedmann cosmology solutions to general relativity describe a homogeneous universe. Later, small anisotropies gradually grew and condensed the homogeneous universe into stars, galaxies and larger structures.

Before decoupling the elementary particles did form a single photon-baryon-electron fluid, where structures with a big enough mass (at least as large as M_J - Jeans Mass - can be derived from the equation of state, the Jeans length and scales with the sound speed c_s in the relative medium, then $c_s \approx \frac{c}{\sqrt{3}}$; from [1] and [5]) are gravitationally stable and were not washed out by pressure changes, what corresponds to a mass larger than the largest supercluster observed.

The time of decoupling is an important time in the structure evolution of the universe. Before the decoupling only very large structures are gravitationally stable. After decoupling the sound of speed for baryons is determined by the temperature, what results in a smaller sound speed $c_s \approx 1.5 \cdot 10^{-5} \cdot c$, what in turn allows much smaller structures to develop: $M_J \approx 10^5 \cdot M_\odot$ (smaller ones are washed out). After decoupling baryons fall into dark matter halos and loose energy via radiation and at very high baryonic densities fusion can star.

The modern view of the origin of structure is that it grew from initially small irregularities through gravitational attraction, which draws material towards regions which start off with higher than average density. As gravity is the driving force, the formation of structure is a probe of the total density of matter, just like rotation curves and bulk flows and here the role of dark matter is taken into account.

Observations suggest that structure formation proceeds hierarchically, with the smallest structures collapsing first, followed by galaxies and then galaxy clusters. As the structures collapse in the evolving universe, they begin to "light up", as baryonic matter heats up through gravitational contraction and approaches hydrostatic pressure balance.

It has been widely accepted that the baryonic matter in the universe would not in itself provide enough gravitational attraction to form the observed structures by the present age of the Universe. Initially, baryonic matter's post-Big Bang temperature and pressure were too high to collapse and form smaller structures, such as stars, via the Jeans instability. This problem can be circumvented by the introduction of non-baryonic dark matter, which provides the extra gravitational force to allow structures to form more quickly and is not inhibited by pressure effects. [1] So the gravity from dark matter increases the compaction force, allowing the formation of these structures. (The *thermal*

production of dark matter relics is the mechanism in which they are produced from particles in thermal equilibrium in such a way, that their resultant energy spectrum is the same as that of the particles in the thermal equilibrium. DM relics can subsequently freeze out from the thermal equilibrium or they can be already decoupled, e.g. when produced from scatterings or decays of thermal particles.)

Classification

Dark matter can be divided into three categories (cold, warm and hot), referring to velocity (rather than an actual temperature), indicating how far corresponding objects moved due to random motions in the early universe, before they slowed due to cosmic expansion - this is an important distance called the "free streaming length" (FSL). The FSL sets a minimum scale for later structure formation, since primordial density fluctuations smaller than this length get washed out as particles spread from over-dense to under-dense regions, while larger fluctuations are unaffected.

- **Hot** dark matter could be described with light relativistic particles travelling with (almost) the speed of light c . On the first look the neutrino would qualify as such particle. They were discovered independently, long before the hunt for dark matter. They were postulated in 1930, and detected in 1956. Neutrinos' mass is less than 10^{-6} that of an electron. The most experiments allow the determination of the (squared) mass-differences between the physical eigenstates, but not the absolute mass. The absolute mass of the neutrino can for example be retrieved from the measurement of the lowered endpoint of the electron energy spectrum close of the β -decay or from the measurement of life-time of the neutrino-less double β -decay. Neutrinos interact with normal matter only via gravity and the weak force, making them difficult to detect (the weak force only works over a small distance (10^{-17} to 10^{-16} m), thus a neutrino triggers a weak force event only if it hits a nucleus head-on). For example, if the average neutrino mass were over $50 \text{ eV}/c^2$ (less than 10^{-5} of the mass of an electron), the universe would collapse. Data from CMB and KATHRIN and other methods indicate that their average mass probably does not exceed $0.3 \text{ eV}/c^2$. Thus, observed neutrinos cannot explain dark matter.

They would have decoupled from baryon-radiation plasma before the era of decoupling. Their high mobility would lead to a wash out from initial density fluctuations (diffusion), what would result in no structure building. Observations showed, that (almost) massless particles like neutrinos cannot act as dark matter candidate. Additional for hot dark matter the large structures (the size of superclusters) would collapse first (top down scenario), but observation only observes the collapse of superclusters only now. Also "hot" dark matter implies that the first objects that can form are huge supercluster-size pancakes, which then fragment into galaxies. Deep-field observations show instead that galaxies formed first, followed by clusters and superclusters as galaxies clump together.

- **Warm** dark matter

Predictions based on warm dark matter are similar to those for cold dark matter on large scales, but with less small-scale density perturbations. This reduces the predicted abundance of dwarf galaxies and may lead to lower density of dark matter in the central parts of large galaxies and some researchers consider this to be a better fit to observations. A challenge for this model is the lack of particle candidates with the required mass ≈ 300 eV to 3000 eV.

No known particles can be categorized as "warm" dark matter. A postulated candidate is the *sterile neutrino*. This is a heavier, slower form of neutrino that does not interact through the weak force, unlike other neutrinos (more see 1.5). Some modified gravity theories, such as scalar-tensor-vector gravity, require "warm" dark matter to make their equations work.

- **Cold dark matter**

Possibilities range from large objects like MACHOs (black holes, neutron stars or brown dwarfs together known as massive compact halo objects) to new particles such as WIMPs and axions (brief explanation later, sec. 1.8), but the constituents are yet unknown. MACHOs cannot make up more than a small fraction of dark matter according to studies of Big Bang nucleosynthesis and gravitational lensing and are therefore excluded as promising theory. Many supersymmetric models offer dark matter candidates in the form of the WIMPy Lightest Supersymmetric Particle (LSP). Separately, heavy sterile neutrinos exist in non-supersymmetric extensions to the standard model that explain the small neutrino mass through the seesaw mechanism.

Cold dark matter refer to heavy non-relativistic particles and which are ascribed no interaction with radiation and decoupled from the baryon-photon plasma. Their low mobility leads to a low speed of sound and the possibility to build up structure from initial density fluctuations. Thus the grow of dark matter structure started at about $z \approx 3600$, the time when (the universe goes from a radiation to a matter dominated universe - see fig. 10) the DM particle (WIMP) thermally decouples from the medium, roughly when the temperature falls below the rest mass of the DM particle (WIMP). Cold dark matter preserves small mass fluctuations in the expected power spectrum for initial density perturbations. In concern of collapse, first objects are the smallest (galaxies) followed by clusters and superclusters (*bottom up scenario*), which is consistent with observations.

Properties and constraints

Additional computer simulations of billions of dark matter particles seem to confirm that the "cold" dark matter model of structure formation is consistent with the structures observed through galaxy surveys, such as the *Sloan Digital Sky Survey* and *2dF Galaxy Redshift Survey*, as well as observations of the *Lyman-alpha forest*.

Although the character of perturbations in the simplest inflationary theories is purely adiabatic, many models predict correlated *adiabatic* and *isocurvature* modes. Predictions

on an isocurvature component is contradicted by current data and analyses (e.g. WMAP, CMB and LSS) and assume, that the adiabatic perturbation mode holds exactly.

Several processes ensure that growth actually depends on the matter content of the Universe.

During the radiation dominated epoch, pressure opposes gravity effectively for wavelengths below the Horizon length. An important scale thus yields the *comoving* horizon size $D_H(z_{eq})$ at the redshift of radiation-matter equality z_{eq} . At early times, free-streaming dark matter particles erased all scales up to the horizon until these particles became non-relativistic, allowing the determination of an upper bound on the amount of relativistic dark matter particles in the early Universe. For example, light massive neutrinos become non-relativistic at z_{eq} , implying that all structure up to the horizon-scale power-spectrum is erased.

A further important scale is set by the process of Silk damping in which photon diffusion can erase perturbations in the matter-radiation fluid. This can be measured from statistical analysis of the spatial distribution of galaxies in today's Universe via the overall power spectrum, which is related to the primordial power spectrum.

The detection of Baryonic Acoustic Oscillations (BAO) adds to the knowledge about the accelerated expansion of Universe and its content by comparing observations of the sound horizon today (using the Large Scale Structure of Universe) to the sound horizon at the time of recombination (using the CMB). The physics of the propagation of the baryonic density waves in the early universe is simple enough to allow the prediction the size of the sound horizon at recombination. As mentioned before (sec. 1.3.3) also the formation of the acoustic oscillation peaks requires **Cold** Dark Matter, as free-streaming relativistic *Hot* dark matter could not accredit.

For simulations of the large scale structure of the Universe to be in agreement with observations, the amount of relativistic dark matter must be limited severely. As the free streaming relativistic particles would have washed out any emergent small-scale structures in the early Universe, notable amounts of relativistic dark matter are excluded. This requires either fairly massive particles as dark matter since accelerator physics exclude the existence of appropriate low mass candidates, or the dark matter particle must have been produced by a mechanism which prevents its thermalization with the rest of the Universe.

The relic density of a dark matter particle after freeze-out in the early Universe must yield the observed density of dark matter, Ω_{dm} of the CMB. In addition, the particle must be stable enough to explain the today's dark matter density. While a lesser relic density could be cured by the possibility that several species of dark matter particles exist, a relic density too large is in disagreement with the observed flatness of the Universe.

The three neutrino types already observed are indeed abundant, and "dark", and matter, but because their individual masses (confirmed through neutrino-oscillations) - however uncertain they may be - are almost certainly tiny, they can only supply a small fraction of dark matter, due to limits derived from large-scale structure and high-redshift galaxies. The neutrino as hot dark matter can be excluded to constitute the bulk of the required dark matter in the Universe due to problems with structure formation in the

early Universe. Additionally the neutrino as weakly interacting, non-baryonic particle cannot provide enough of the observed dark matter energy density Ω_{dm} without being in severe contradiction to the observed structure of the Universe. Cold dark matter leads to a "bottom-up" formation of structure while hot dark matter would result in a "top-down" formation scenario, whereat the latter is excluded by high-redshift galaxy observations. (Also there is strong evidence that galaxies formed before clusters, in the sense that the stars in galaxies are 10 to 14 billion years old, but many clusters of galaxies are still forming today. This would rule against the top-down scenario and support the bottom-up process.)

Also the new physics related to dark matter must respect the observations of the photon to baryon abundance, η , and temperature T at the time of Big Bang Nucleosynthesis (BBN), as only a very limited amount of particle decays from the dark matter sector are allowed to maintain this/them.

Possible candidates for non-baryonic dark matter are hypothetical particles such as axions or supersymmetric particles (more see later chapter 1.8). Unlike baryonic matter, non-baryonic matter did not contribute to the formation of the elements in the early universe (BBN) and so its presence is revealed only via its gravitational effects. In addition, if the particles of which it is composed are supersymmetric, they can undergo annihilation interactions with themselves, possibly resulting in observable by-products such as gamma rays and neutrinos ("indirect detection" - see sec. 1.7.2).

Predictions on the abundances of the lightest elements synthesized in the early Universe are in good agreement with the primordial abundances inferred from observational data: This is understood as a validation of the standard hot Big Bang Cosmology. Big Bang Nucleosynthesis provides powerful constraints on possible deviations from the cosmological Standard Model (sec. 1.4) as well as on new physics beyond the Standard Model of particle physics (see sec. 1.5). BBN constraints cold dark matter to be non-baryonic as interactions between dark matter spoil the observed abundances of the primordial elements. Furthermore, the reheating of the Universe by the decay of hypothetical particles at the epoch of Big Bang Nucleosynthesis is constrained by its interference with the formation of the primordial elemental abundances.

Finally, relics from the early Universe which could constitute Superheavy (or ultra-heavy) dark matter candidates are in contradiction to the absence of cosmic rays above the Greisen-Zatsepin-Kuzmin (GZK) cut-off.

1.4. The Standard Model of Cosmology - Λ CDM Model

It is a description of the universe, respecting the phenomena on dark matter (about its existence, hints about certain properties and the amount of dark matter in the universe) explained in the previous sections, and contains a cosmological constant (Λ) added to the Einstein's equation of general relativity (see eq. (88)), with the equation of state $p_\Lambda = -\rho_\Lambda$. In short, it assumes, that the dark matter found in the Universe is cold (i.e. it is non-relativistic; **CDM**), is based on the cosmological principle (described in a previous section), and includes a "Big Bang", which implies, that the universe originates from an initial singularity, from which space-time started expanding, followed by an inflationary phase. This model described the Universe as a perturbed FLRW space-time (see appendix A.3.2) with dynamics governed by Einstein's equations, assuming a vanishing global space-time curvature ($k = 0$, as mentioned before).

It is frequently referred to as "the standard model of Big Bang cosmology", because it is the simplest model that provides a reasonably good account of properties (some discussed in previous sections) of the cosmos like the existence and structure of the CMB, large-scale structure (in the distribution of galaxies), the abundances of hydrogen (including deuterium), helium, and lithium and the accelerating expansion of the universe (observed in the light from distant galaxies and supernovae). Also the model assumes, that general relativity is the correct theory of gravity on cosmological scales.

Λ represents the cosmological constant, which is currently associated with a dark energy (or vacuum energy) in empty space that is used to explain the contemporary accelerating expansion of space against the attractive effects of gravity. A cosmological constant has negative pressure, $p = -\rho c^2$, which contributes to the stress-energy tensor that, according to the general theory of relativity, causes accelerating expansion.

To describe the evolution of the universe the Friedmann equations are used, with the first:

$$H^2 = \left(\frac{\dot{a}}{a}\right)^2 = \frac{8\pi G}{3}\rho - \frac{kc^2}{a^2} + \frac{\Lambda c^2}{3}, \quad (31)$$

which is derived from the 00 component of Einstein's field equations (see appendix eq. (88)) and the second:

$$\frac{\ddot{a}}{a} = \frac{\Lambda c^2}{3} - \frac{4\pi G}{3} \left(\rho + \frac{3p}{c^2}\right), \quad (32)$$

which is derived from the first (31) together with the trace of Einstein's field equations. H is the Hubble parameter, c is the speed of light in vacuum, a the scale factor, G the gravitational constant, ρ the mass density, $\frac{k}{a^2}$ the spatial curvature and Λ the cosmological constant, which is the driving force for the accelerated expansion of the universe (expansion rate of the universe \dot{a}). The spatial curvature is set to zero as our universe is (at least almost) flat. a , H , ρ , and p are functions of time, whereby ρ , and p are the density and pressure, respectively. Although this expansion increases the distance between objects that are not under shared gravitational influence, it does not increase

the size of the objects (e.g. galaxies) in space. It also allows for distant galaxies to recede from each other at speeds greater than the speed of light. The local expansion is less than the speed of light, but expansion summed across great distances can collectively exceed the speed of light. Furthermore, the critical density (ρ_c) is defined by setting Λ to zero

$$\rho_c = \frac{3H^2}{8\pi G} = 1.87847 \cdot 10^{-26} h^2 \text{ kg m}^{-3}, \quad (33)$$

where $h \equiv H_0 / (100 \text{ km s}^{-1} \text{ Mpc}^{-1})$ is the reduced Hubble constant. The density parameter, Ω (described on page 20), is defined as the ratio of the actual (or observed) density ρ to the critical density ρ_c of the Friedmann universe. The relation between the actual density and the critical density determines the overall geometry of the universe; when they are equal, the geometry of the universe is flat (Euclidean).

Since the densities of various species scale as different powers of a , e.g. a^{-3} for matter etc., the Friedmann equation can be conveniently rewritten in terms of the various density parameters, and in the minimal 6-parameter Λ CDM model, it is assumed that curvature Ω_k is zero (and $w = \frac{p_\Lambda}{\rho_\Lambda} = -1$, where w is the equation of state of dark energy), so this simplifies to

$$H(a) \equiv \frac{\dot{a}}{a} = H_0 \sqrt{\Omega_m a^{-3} + \Omega_{rad} a^{-4} + \Omega_\Lambda}, \quad (34)$$

whereat by neglecting the term of radiation density (very small today, $\Omega_{rad} \approx 10^{-4}$) an analytical solution for $a(t)$ can be obtained.

Independent on what exactly dark matter is composed of, this model describes the evolution of the universe from right after the inflationary epoch up to now and to the future very well via eq. (31) and (32). (More details on Einstein's equations are given in the section on cosmology, see appendix A.3.)

1.5. The Standard Model of Particle Physics

The Standard Model of Particle Physics (**SM**) was developed throughout the latter half of the 20th century and is used for classifying all the subatomic particles known. It contains three of the four known forces of nature:

- weak interaction
- strong interaction
- electromagnetic interaction

These interactions are mediated by massless spin one gauge bosons. The SM accounts since many years for all observed particles and interactions up to now, but there is no particle within the Standard Model which has the right properties to explain the effects of dark matter. From the mathematical point of view the SM is a relativistic quantum field theory (QFT), containing the internal symmetries of the unitary product gauge group $SU(3)_c \otimes SU(2)_L \otimes U(1)_Y$, which exhibits a spontaneous symmetry breakdown:

$$SU(3)_c \otimes SU(2)_L \otimes U(1)_Y \rightarrow SU(3)_c \otimes U(1)_Q \quad (35)$$

A QFT treats particles as excited states of the underlying physical field, so these are called field quanta. Quantum mechanical interactions between particles are described by interaction terms between the corresponding underlying quantum fields. These interactions can conveniently be visualized via Feynman diagrams, that also serve as a formal tool to evaluate various processes. The theory is commonly viewed as containing the fundamental set of particles: the leptons, quarks, gauge bosons and the Higgs particle (fig. 12).

Since it is a field theory its fundamental objects are *quantum fields*, which are defined at all points in spacetime. These fields are the fermion fields (ψ , which account for "matter particles"), the electroweak boson fields (the W_μ SU(2) triplet field: W_1, W_2, W_3 and the B_μ U(1)_Y hypercharge singlet, which both are massless), the gluon field (G_μ^a , massless too) and the Higgs field (φ). U(1) (from eq. (35)) acts on B and φ , SU(2) acts on W and ϕ , and SU(3) acts on G.

That these are quantum rather than classical fields has the mathematical consequence that they are operator-valued. In particular, values of the fields generally do not commute. As operators, they act upon the quantum state (ket vector) - little more detail is given in appendix A.8. The fundamental constituents of matter are spin-1/2 particles, fermionic quarks and leptons. The left-handed fermions are arranged in three generations of SU(2)_L doublets. The masses of the fermionic fields are generated due to their Yukawa coupling to the Higgs field, arising from the Yukawa interactions of the quark fields with the Higgs condensate. The quarks in the weak eigenstate representation are related to the mass eigenstates by the Cabibbo-Kobayashi-Maskawa (CKM) matrix. Analogous to the quark sector, for the leptonic sector there emerges a (unitary) matrix, called the Pontecorvo-Maki-Nakagawa-Sakata (PMNS) matrix.

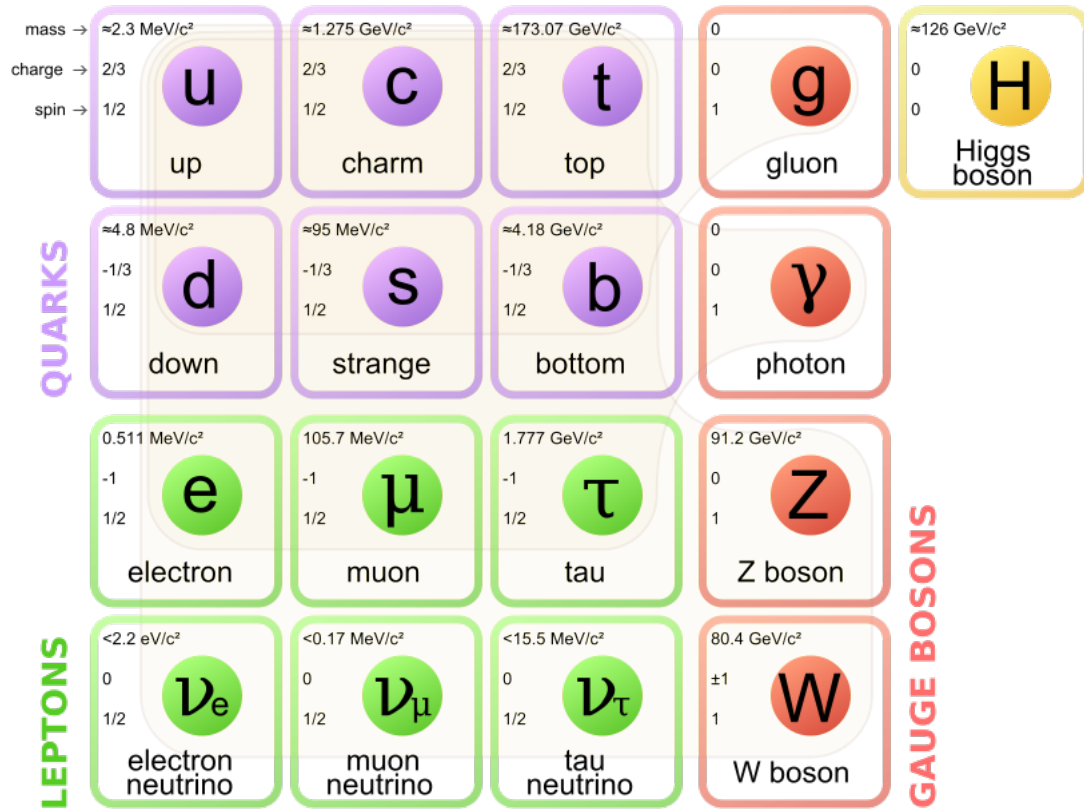


Figure 12: A schematic depiction of the Standard Model of elementary particles, with the three generations of matter (first three columns), gauge bosons in the fourth column, and the Higgs boson in the fifth. [31]

The weak force is best understood in terms of electro-weak theory (EWT). During the quark epoch of the early universe, the electroweak force separated into the electromagnetic and weak forces. Important examples of the weak interaction include beta decay, and the fusion of hydrogen into deuterium (that powers the Sun’s thermonuclear process). Under spontaneous electroweak symmetry breaking, from $SU(2)_L \otimes U(1)_Y$ to $U(1)_Q$, the electroweak and the Higgs field merge to the observable massive vector bosons in the SM W^\pm , Z^0 , a massless γ and a massive Higgs boson H^0 . After spontaneous symmetry breakdown, a $U(1)$ symmetry, acting on Q (the electric charge generator) emerges (eq. (35)). The spontaneous symmetry breaking causes the W_3 and B bosons to coalesce together into two different bosons (the Z_0 boson and the photon γ of quantum electrodynamics.) and the W_1 and W_2 bosons, in turn, combine to deliver the massive charged bosons W^\pm .

All charged particles take place in the electromagnetic interaction, whereat the force can be attractive and repulsive, depending on the charge of interacting the particles. The mediator of the electromagnetic interaction is the photon γ . It’s range is infinity (compare forces in table 1).

The weak interaction affects all the fermions of the Standard Model, but acting only on left-handed fermions (and right-handed anti-fermions) as well as the Higgs boson. As neutrinos have only a weak charge and no electric or strong charge, only left-handed neutrinos are observed. Neutrinos interact through gravity and the weak interaction only, and neutrinos were the original reason for the name *weak force*. Its mediators are the W- and Z-bosons, which restrict the range of this force by their finite mass. The weak interaction violates parity (P) and charge conjugation (C) maximally and does not preserve the combined CP symmetry to a smaller extent.

Further the first of the three gauge groups shown in eq. (35) above is the $SU(3)_c$ of color (strong) interaction, known as Quantumchromodynamics (QCD). Quarks participate in the strong interaction, carrying the corresponding charge known as the color charge. The mediator are gluons (G_μ^a), obeying the $SU(3)$ color symmetry, which also contain a charge and couple to each other (self coupling). These quarks are bound to each other within a hadron (for example baryons consist of three quarks, mesons of two quarks) and are not freely visible (*confined*). Due to the self-interaction of the gluons the strong force is a short-range force (compare forces in table 1), which preserves the symmetries of parity (P) and charge conjugation (C).

Table 1: Fundamental interactions with their strength relative to the strong interaction and their range.

interaction	relative strength	range
strong interaction	1	1 fm
electromagnetic interaction	10^{-2}	∞
weak interaction	10^{-7}	10^{-3} fm
gravitational interaction	10^{-40}	∞

From the cosmological point of view, the Standard Model of particle physics is the effective theory which governs the evolution of the Universe from the point when electro-weak symmetry breaking occurred.

The crucial input for cosmology and the evolution of the particle content of the Universe from the SM is the particle dynamics (to know the existing particles, their masses and their interactions) during the early Universe. This is important for the calculation of relic densities of the various particle species found in the Universe. While leptogenesis and baryogenesis is not explainable within the SM, it does contain the elementary fields of all experimentally confirmed particles and forces. It is the foundation for the understanding of the freeze-out of neutrons and protons and for the subsequent Big Bang Nucleosynthesis (BBN).

1.5.1. Shortcomings of the SM

The SM does leave some phenomena unexplained and it falls short of being a complete theory of fundamental interactions. For example it does not incorporate the full theory

of gravitation as described by general relativity (brief explanation see appendix A.3.1), or account for the accelerating expansion of the universe (as possibly described by dark energy).

It also does not incorporate the observed neutrino oscillations (and their non-zero masses). Neutrinos are massless in the standard model of particle physics. As right-handed neutrino would not interact via weak, strong, or electromagnetic interactions, it would be a *sterile neutrino*. Contrary, the standard left-handed neutrinos are called *active neutrinos*. Sterile neutrinos may also explain why the mass of the active neutrinos $m_{\nu-a}$ is so small compared to the mass of the other leptons via the *see saw mechanism*. The right-handed neutrinos could gain additional mass via a Majorana mass term, which includes a free parameter M . Sterile neutrinos could interact with matter through a mass mixing, but it is suppressed by $m_{\nu-a}/M$.

In physical cosmology, baryogenesis (and leptogenesis) is the generic term for the hypothetical physical processes that produced an asymmetry (imbalance) between baryons (leptons) and anti-baryons (anti-leptons) produced in the very early universe. This results in the dominance of matter (baryons+leptons) over antimatter (anti-baryons + anti-leptons) and can not be explained by the amount of CP violation in the SM.

Since no Standard Model particles are left as candidates for the dark matter, motivated extensions like Supersymmetry, Extra Dimensions, Axions, sterile neutrinos, etc. are studied.

By talking about physics *beyond* the Standard Model (BSM), it refers to the theoretical developments needed to explain the (above mentioned) deficiencies of the Standard Model (the origin of mass, the strong CP problem, neutrino oscillations, matter-antimatter asymmetry, and the nature of dark matter and dark energy). Another problem lies within the mathematical framework of the Standard Model itself - the Standard Model is inconsistent with that of general relativity, to the point that one or both theories break down under certain conditions (for example within known spacetime singularities like the Big Bang and black hole event horizons).

1.6. Unsolved Questions and Open Issues

The Milky Way is surrounded by lots of smaller galaxies called satellite galaxies. The biggest and most famous of these are the Large and Small Magellanic Clouds (only visible in the Southern Hemisphere). Persistent challenges from observations that probe the innermost regions of dark matter halos and the properties of the Milky Way's dwarf galaxy satellites facing the remarkably successful CDM cosmological model. The CDM model has been demonstrably successful at explaining a variety of observations on cosmological scales. Tests on smaller scales are often complicated by the physics of galaxy formation, but are crucial for verifying this model. However, testing the Λ CDM model on galactic and sub-galactic scales is considerably more difficult (both from an observational and a theoretical point of view). Some current observational and theoretical discrepancies of these "small scale controversies" are reviewed in this section.

1.6.1. Core-Cusp Problem

This is a problem, arising from cosmological N-body simulations, which indicate an inner distribution of the density profile ρ of dark matter halos as $\rho \propto r^\alpha$, with $\alpha = -1$. [32] The core-cusp problem (or cuspy halo problem) refers to a discrepancy between this simulations and the observed dark matter density profiles (of low-mass - or dwarf - galaxies). It can be shown, that a halo with constant DM density ρ leads to a rotation curve with a linear increase, in contrast to a "cuspy" halo with a DM density with $\rho \propto r^{-1}$ leads to an increase of the rotation curve with the square root of the radius.

Nearly all simulations form dark matter halos which have "cuspy" dark matter distributions, with density increasing steeply at small radii, while observational determination of α based on rotational curves result in $\alpha \approx 0$. So these rotation curves suggest, that they have flat central dark matter density profiles ("cores").

From more evolved N-body simulations fitted with a generic NFW (eq. (18) and parameters from (19)) fit function leads to a DM density profile with a similar cuspy behaviour of the DM profile.

Potential solutions to the core-cusp problem are:

- By including a baryonic feedback (i.e. baryonic matter falling into the gravitational potential, leading to a supernova explosion which also leads to a decreased DM density in the inner part of the halo, or a active galactic nuclei), a "flatten out" of the core of a galaxy's DM profile can be achieved, since the feedback-driven gas outflows produce a time-varying gravitational potential that transfers energy to the orbits of the collisionless dark matter particles.
- Another proposal is, that DM only weakly interacts with ordinary matter but has strong self interaction.

The key question is whether the conflicts between N-body predictions and observed galaxy properties can be resolved by "baryonic physics" - gas cooling, star formation, and associated feedback - or whether they require different properties of the dark matter itself.

1.6.2. Missing Satellite Problem

It is also known as the dwarf galaxy problem. As the problem in the previous section it arises also from numerical cosmological simulations. These simulations predict the evolution of the distribution of matter in the universe, where dark matter seems to cluster hierarchically and in ever increasing number counts for smaller-and-smaller-sized halos. It refers to the difference of the number of predicted CDM sub-halos obtained with N-body simulations compared to the number of satellite galaxies observed in our local group.

The left panel of figure 13 shows the projected dark matter density distribution of a $10^{12} M_{\odot}$ CDM halo formed in a cosmological N-body simulation. Because CDM preserves primordial fluctuations down to very small scales, halos today are filled with enormous numbers of sub-halos that collapse at early times and preserve their identities after falling into larger systems.

Prior to 2000, there were only nine dwarf satellite galaxies known within the ≈ 250 kpc virial radius of the Milky Way halo (illustrated in the right panel of figure 13), with the smallest having stellar velocity dispersions $\approx 10 \text{ km s}^{-1}$. Klypin et al. (1999) and Moore et al. (1999b) predicted a factor ≈ 5 -20 more sub-halos above a corresponding velocity threshold in their simulated Milky Way halos. Establishing the "correspondence" between satellite stellar dynamics and sub-halo properties is a key technical point. Today about 4-5 times more satellite galaxies with a circular velocity $v_{\text{circ}} \approx 10 - 20 \text{ km s}^{-1}$ is expected from simulation. [5] (Sub-halos are rather characterised by their circular velocity v_{circ} than their total mass, because of problems defining the sub-halo with respect to the halo.) With v_{circ} the mass within the radius of the rotating sub-halo can be measured.

A combination of feedback (explained in the previous subsection) and low star-formation efficiency could explain why most of the dark matter sub-halos orbiting the Milky Way do not host visible galaxies.

A variety of studies have shown that baryonic effects can plausibly account for cores in halos occupied by high surface brightness galaxies and can plausibly suppress star formation in very low mass halos. Improved simulations may show that baryonic effects can soften cusps even in galaxies that are now dark matter dominated, or they may show that the energetics arguments summarized above do indeed point to a genuine problem for CDM that cannot be resolved by supernova feedback or galactic tides. Improved simulations of models with interacting dark matter may show that they can readily solve the small scale problems, or they may show that cross-section parameters chosen to match one set of observations ultimately fail when confronted with another set. Improved measurements of stellar velocities in satellite galaxies, and discovery of new satellites from imaging surveys such as PanSTARRS and the Dark Energy Survey, may better delineate the satellite problem itself, and the problem shifts from a DM-problem towards a problem of galaxy formation.

The most promising possible solutions so far are:

- Processes keeping them "dark" by suppressing gas accretion in these halos (for example ultraviolet photoionisation prevents from cooling a gas).

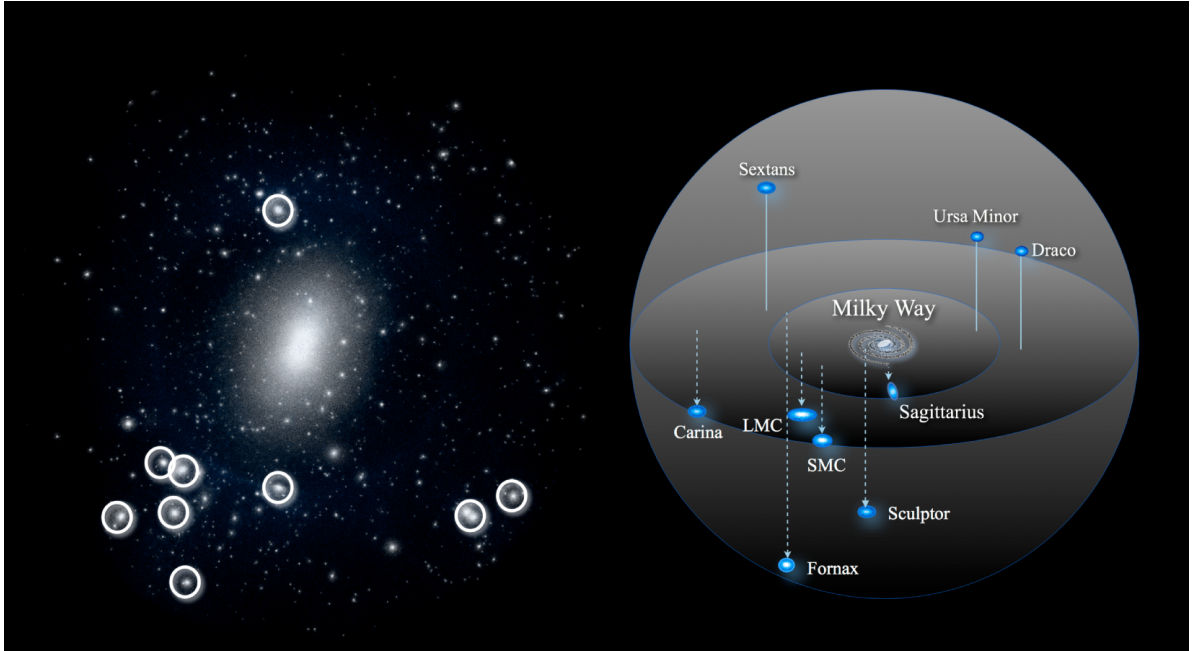


Figure 13: The missing satellite and "too big to fail" problems. (*Left*) Projected dark matter distribution (600 kpc on a side) of a simulated, $10^{12}M_{\odot}$ CDM halo (Garrison-Kimmel, Boylan-Kolchin, & Bullock, in preparation). The numerous small sub-halos far exceed the number of known Milky Way satellites. Circles mark the nine most massive sub-halos. (*Right*) Spatial distribution of the "classical" satellites of the Milky Way. The central densities of the sub-halos in the left panel are too high to host the dwarf satellites in the right panel, predicting stellar velocity dispersions higher than observed. The diameter of the outer sphere in the right panel is 300 kpc; relative to the simulation prediction (and to the Andromeda galaxy) the Milky Way's satellite system is unusually centrally concentrated (Yniguez et al. 2013). [33]

- Dwarf galaxies are too faint to be discovered (recently the SDSS has observed some ultra-faint galaxies). It could be, that smaller halos do exist, but only a few of them end up becoming visible because they have not been able to attract enough baryonic matter to create a visible dwarf galaxy. In support of this are observations of ultra-faint Milky Way dwarf satellites, that showed that some were around 99.9% dark matter (with a mass-to-light ratio of about 1000). (See also end of 1.3.1 on page 6.)
- Possibly dwarf galaxies tend to be merged into or tidally stripped apart by larger galaxies due to complex interactions. This tidal stripping has been part of the problem in identifying dwarf galaxies in the first place, which is an extremely difficult task since these objects have low surface brightness and are highly diffused, so much that they are virtually unnoticeable.

1.6.3. "Too big to fail" Problem

The "missing satellites problem" is perhaps the most widely known and most investigated discrepancy between theoretical predictions of the Λ CDM model and observations. Still, any time concentrating on galaxies that are satellites of other galaxies, complicated interactions between messy atoms and photons are getting in the way of the pristine elegance of the non-interacting dark matter. So it is checked if this purported problem exists even out "in the field" with lonely galaxies far away from big monsters like the Milky Way.

It is similar to core-cusp problem, whit N-body simulation predicting to much mass in the central region. Comparing the mass of the observed dwarfs and the massive sub-halos from N-body simulation leads to a discrepancy, because the mass of the sub-halos from simulation exceeds the mass of the observed dwarfs by a factor four to five.

The too big to fail problem is pointing out, that some of the predicted galaxies are just so massive that there is no way they could not have visible stars. Or, put another way: the Milky Way does have some satellites, as do other galaxies, but when examining these smaller galaxies, they seem to have a lot less dark matter than the simulations would predict. This effect is significant and a statistical fluctuation can be excluded.

Either these sub-halos actually exist as predicted in the Milky Way, requiring to understand their properties and stellar content, or they do not exist, in which case it is necessary to understand the mechanism(s) that suppress their formation or survival. Dark matter self-interactions would also reduce the central densities of sub-halos, and would additionally make them more vulnerable to tidal disruption. It is far from obvious that the abundance and dynamics of observed MW satellites would be correctly reproduced in the viable parameter space of these non-CDM models. The majority of the most massive sub-halos in dissipationless Λ CDM simulations are too dense to host any of the bright Milky Way satellites. It follows, that galaxy formation must be effectively stochastic in haloes with maximum circular velocities of $v_{circ} \leq 50 \text{ km s}^{-1}$. This conclusion may be circumvented if the Milky Way's sub-halo population differs substantially from the average Λ CDM expectation, or if the abundance or structure of massive sub-halos in the Milky Way is strongly affected by baryonic processes or different dark matter physics. [34] It shall be noted, that it is still possible, that combinations of several of the effects mentioned above may prove sufficient to provide a solution (so that baryonic effects does not seem to be able to resolve the reported discrepancy, at least when considered on its own). It is also possible that the baryonic effects considered may be larger than indicated by the theoretical models used in some works.

1.7. Dark Matter Detection

The previous sections presented some properties, boundaries and constraints and evidence for dark matter. All the observed evidence for dark matter was found only through gravitational interaction, but some theories expect some additional (weak) interactions beyond gravity between dark matter and Standard Model particles. The aim is the detection of dark matter through non-gravitational interaction, but so far there is no conclusive prediction of a DM particle (χ) candidate and size and type of interaction. There is a big diversity of theories for DM particle candidates with a broad range of predictions which need different approaches with different experimental reach. A compelling solution for the DM problem requires a coherent answer from different approaches. These orthogonal approaches, described in a little more detail in the following sections, can be categorized as:

1. **direct detection** - elastic scattering between DM and a nucleon
2. **indirect detection** - through the annihilation of DM particles into Standard Model particles
3. **production** - meaning the annihilation of Standard Model particles into DM particles
4. **(Astrophysical probes)** - non-gravitational interaction of DM particles on astrophysical scales

The different experimental approaches 1. to 3. can be seen as realisation of the same Feynman diagram with space, time and direction being exchanged in figure 14.

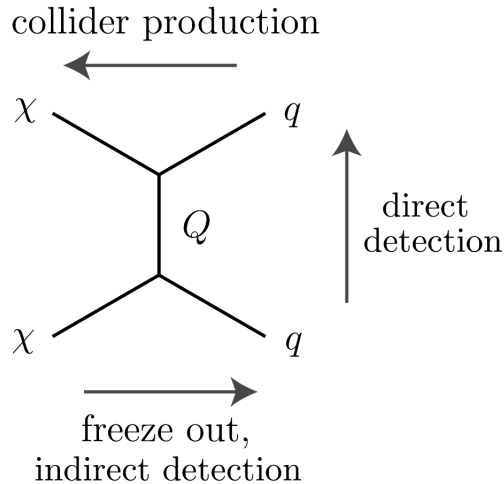


Figure 14: Feynman diagram with the possible interaction for studying non-gravitational interaction between matter and dark matter. To describe the various approaches the arrow indicating the evolution of time and space needs to be rotated. Fig. taken from [35].

In order to establish a firm link between a dark matter particle candidate and the observed effects of dark matter in the Universe, it must be shown that the particle is abundant in the Universe today. Both direct and indirect detection experiments looking for WIMP dark matter are addressed and a short summary of experiments looking for axions is given, too.

1.7.1. Direct Dark Matter Detection

Earth based experiments can search for scattering of dark matter particles on standard model particles, since the Earth is located in the galactic dark halo. In direct detection experiments one looks for the interaction of a WIMP (explanation see 1.8.1) with a suitable detector in a laboratory on earth and considers only interaction with quarks (the most microscopic scale). As no free quarks exists, the observable effect would be a recoiling nucleus in the detector target. So the effective WIMP-nucleon interaction (the next level) depends on the quark content per nucleon, i.e. per proton and per neutron. Finally, the WIMP-nucleus cross section $\sigma_{\chi N}$ is constructed by coherently adding the contributions from the individual nucleons per nucleus. If dark matter is made up of WIMPs, then millions, possibly billions, of WIMPs must pass through every square centimetre of the Earth each second. Many experiments aim to test this hypothesis. Although WIMPs are popular search candidates, most experiments can also analyse their data for signatures of other models of DM (e.g. direct detection experiments are able to search for axion in the μeV to meV region).

The interaction of WIMPs and ordinary nuclei can proceed via a spin-dependent (SD, axial-vector) or a spin-independent (SI, scalar and vector) channel. Considering WIMPs as the lightest supersymmetric (SUSY) neutralino, their coupling to quarks can be modelled via axial-vector interactions α_q^a to the quark *spin* (SD), or via scalar interactions α_q^s (quark type q) to the quark *mass* (SI). The WIMP-quark couplings α_q^s and α_q^a has to be calculated on the fundamental level by evaluating the corresponding Feynman diagrams (examples for the coupling to the light quarks and to the gluons are shown in fig. 15). In the most models of SI interactions the cross section scales like A^2 , which is the reason to use heavy targets aiming for high event rates (taking advantage from the A^2 scaling). Results from experiments with different targets can be compared via the WIMP-nucleon cross section (via the scaled WIMP-nucleus cross section $\sigma_{0,SI}/A^2$). For the SD cross section there is no scaling with A^2 nor is there a scaling with J^2 (with J the total nuclear spin). So far no indication for spin-dependent interactions are observed. Consequently, direct searches can set limits on the cross section.

The parameters for direct methods can be divided in three groups:

- The astrophysical parameters are $\rho_0 = n_\chi m_\chi$ the density, $v_{\chi N}$ the velocity of the WIMP relative to the target nucleus and v_{esc} the velocity needed to escape the gravitation well of the Galaxy. They depend on the used halo model and are fixed by astrophysical observations.

- Detector parameters are chosen via the material selection for the target and the experimental set-up. They are the atomic weight A (which is related to the number of nuclei in the target via $N_T = mN_A/A$), the target mass m and the the minimal measurable energy - the detector *threshold* E_T .
- The particle parameters (m_χ and $\sigma_{\chi N}$) depend on the actual model for the DM particle and its interaction with the nucleus. $\sigma_{\chi N}$ is the cross section for WIMP-nucleus-scattering with the unit usually in barn ($1 \text{ b} = 100 \text{ fm}^2 = 10^{-28} \text{ m}^2$). As result of a direct detection experiment, limits or detection claims are given for $\sigma_{\chi N}(m_\chi)$. To compare the results of experiments with different target materials, $\sigma_{\chi N}$ is often scaled to $\sigma_{\chi n}$, the WIMP-nucleon-cross section.

Since the cross section is very low, the expected event rate is extremely low (in the order of 1 event per ton per year). Therefore experiments with a target mass in the multi-ton range are planned (e.g. the LZ experiment - LUX-Zeplin (LZ) a international collaboration combining the LUX and ZEPLIN groups) to obtain a high statistic of potential scatterings. This shall be achieved via a large exposure (i.e. target mass m times the observation time). Additionally, one aims for low detector thresholds E_T .

WIMP induced nuclear recoils are a rare process ($\sigma \lesssim 10^{-10}$ pb). In the isothermal, isotropic halo model, the mean velocity of the WIMPs is equal to the local circular velocity. For a laboratory on earth, this velocity has to be modified by the peculiar motion of the sun and the motion of earth around the sun. For these velocities, WIMPs will interact with ordinary matter through elastic scattering on nuclei. For the velocities assumed for WIMPs in the galactic halo, the nuclear recoil is expected to be of the order of a few tens of keV. In this energy region, detectors are prone to a wide variety of background events induced by radioactivity of the experimental surroundings, what requests a proper discrimination of the spurious events. For the sensitivity achieved in this field today, also the shielding from cosmic rays is mandatory, thus these experiments are located in underground laboratories. Most modern experiments employ techniques which can discern nuclear recoils in the detector and signals due electrons and γ s. Furthermore, it is possible to discriminate α -particles and protons from recoiling nuclei.

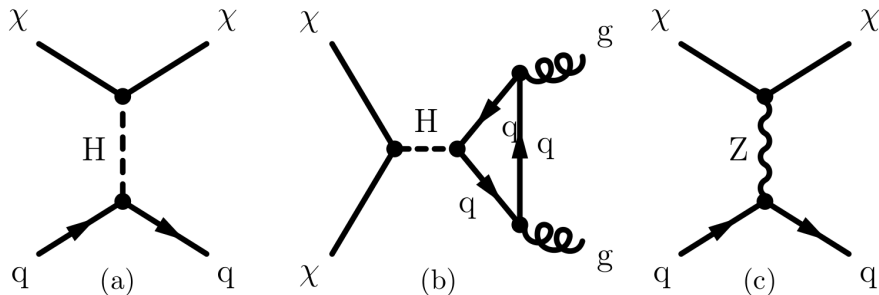


Figure 15: Example Feynman diagrams contributing to: spin-independent WIMP-quark scattering (a) and WIMP-gluon scattering (b), spin-dependent WIMP-quark scattering (c). Figure taken from [5] and based on [36].

Only materials with very low contamination (called *radiopure* materials) are selected for the detector construction, and as surrounding of the detector shieldings for further reduction are placed, like Pb against gamma-rays, or polyethylene against neutrons (e.g. from U/Th in the concrete of the laboratory floor). This reduces the background from radioactivity to neutron induced nuclear recoils if the discrimination technique is applicable.

The most stringent constraints on the medium mass WIMP type dark matter is achieved in experiments with simultaneous read-out of two independent signal channels of a detector, allowing to discriminate the various sources of energy deposition due to the ratio of the two signal strengths (i.e. it is possible to discern the energy deposition by a nuclear recoil from the energy deposition of an electron).

For example a detector type consists of cryogenic bolometers made of a scintillating insulator, which are operated in such a way that the scintillation light and the heat deposited can be read out simultaneously. The required sensitivity of the bolometer demands operation temperatures close to absolute zero temperature. The discrimination of the particle type becomes possible by the light yield of a given event in the detector. If energy is deposited by a recoiling nucleus, the light is *quenched*, compared to an energy deposit by an electron or by a lighter particle, where less scintillation light is produced in the crystal. This technique allows the operation of a large variety of materials. This work is focusing on the CRESST experiment (more details in chapter 2), which operates a set of CaWO_4 bolometers at $T \lesssim 30 \text{ mK}$ in the Laboratori Nazionali del Gran Sasso (LNGS) underground laboratory. LUX and CRESST are examples for experiments which obtained null results and set exclusion limits, which set the leading limits for the lowest cross section and the lowest recoil energy respectively.

Most experiments use either cryogenic or noble liquid detector technologies. Cryogenic detectors (as CRESST mentioned above) generally operate at temperatures below 100 mK and measure the heat produced when a particle hits an atom in a crystal absorber (scintillating insulators, or semi-conductor such as silicon and germanium have been operated successfully). Among the many different cryogenic detector experiments are: CDMS, CRESST, EDELWEISS, EURECA.

(liquid) noble gas detectors are three dimensional sensitive dual phase trajectory projection chambers (TPCs), which detect the direct scintillation light from an event in the liquid phase and the secondary proportional scintillation light in the gaseous phase from the ionization of the event driven in a high voltage field. Noble liquid experiments include ZEPLIN, XENON, DEAP, ArDM, WARP, DarkSide, PandaX, and LUX, the Large Underground Xenon experiment.

Other experiments include DAMA/LIBRA, KIMS, COUPP, TEXONO (operates ultra-low energy germanium semiconductor diodes - ULEG), CoGeNext (operates a heavy p-type point contact germanium detector), SIMPLE and PICASSO.

DAMA/LIBRA operates highly radiopure NaI crystals, the KIMS experiment runs

scintillating CsI(Tl) crystals, both read out by photomultiplier tubes (PMT) and try to observe a annual modulation of the count rate (with a maximum around June 2nd). The COUPP experiment operates a bubble chamber of superheated CF₃I, which is examined photographically for bubbles due to interactions of impinging particles with the superheated liquid.

1.7.2. Indirect Dark Matter Detection

The search for the secondary particles of DM annihilation is labelled indirect detection. If the DM particle χ is a Majorana particle, two χ can annihilate and produce secondary particles with a total energy of two m_χ . So the indirect detection of DM is the attempt to detect the signature of the annihilation of DM particles with the corresponding anti-particles. The annihilation process used for this indirect DM detection is identical to the process which is responsible for the DM relic density produced during WIMP freeze out. Thereby it delivers a hint for the size (or benchmark process) for the expected cross section. This searches mainly focus on the detection of WIMP-like DM particles in the GeV to TeV mass region as expected from freeze out.

Deep within the gravitational well of a galaxy, an over-abundance of DM is expected. If sufficient over-densities of dark matter particles are located within our galaxy, a detectable flux of secondaries (for example from WIMP annihilation) can be detectable. The expected reaction rate depends on $\rho_\chi^2(\vec{x})$, thus regions of over-density like the center of the galaxy should show an enhanced reaction rate. The highest DM density and therefore flux of decay products is expected from the galactic center. The expected signal is highly dependent on the model of the dark matter halo density profile. Furthermore indirect detection relies critically on the knowledge and modelling of the interactions of the secondary particles with the galactic environments, i.e. the gas distribution of the galaxy and the halo, the magnetic field and the interstellar radiation field.

The produced Standard Model particles could be charged (fermions) or electrically neutral (photons or neutrinos). The potential messengers heralding WIMP annihilation are anti-matter particles, synchrotron radiation of the produced charged secondaries, neutrinos and gamma rays. Only muon neutrinos ν_μ are reconstructed via the weak interaction and production of muons, producing Cherenkov light (but so far no excess of neutrinos has been observed - but thus a limit can be set). For high-energetic γ -rays and neutrinos, the direction to the source can be identified relatively easy. Positrons (and other charged cosmic rays) diffuse through the galaxy and the halo as they interact with the local matter and the magnetic field. High energetic positrons thermalize quickly due to inverse Compton-scattering off cosmic microwave background photons and synchrotron radiation in the galactic magnetic field. This restricts the detectable flux to regions a few kpc nearby. Within this reach, the galactic center as most likely region of DM annihilation is located. Thus they yield no information about the location of their origin. Another channel for indirect dark matter detection are anti-protons, which are expected as well in DM annihilations and can travel much longer distances than positrons. During their passage of the interstellar medium they are expected to create additional secondary signals which should be observable if the anti-protons travel

through regions outside the galactic plane. On top of the expected signal in each channel, ordinary physics happening in the galaxy provides a background. Standard astrophysical processes are responsible for a large flux of high energetic γ -rays from the center of our galaxy which constitute a serious background. Although a theoretical forecast the amount of neutrinos produced in DM annihilation in galactic or extra-galactic sources is too small to be detectable, WIMP DM annihilation in the center of the sun could potentially generate a detectable flux of mono-energetic high energy neutrinos. The neutrino telescopes Antares and IceCube placed upper limits on the muon flux from the sun which corresponds to the favoured decay channel of Kaluza-Klein type WIMPs (and on a spin dependent cross-section from the assumed WIMP capture rate in the sun). Neutrino detection is done with large area detectors, which detect neutrinos via leptons produced in a charged interaction. Detection of charged particles is done with satellites or ISS based detectors (e.g. AMS-02).

Dark matter particle annihilation can proceed via several decay channels, resulting in mono-energetic γ -rays. This mono-energetic lines are readily distinguishable from astrophysical sources and would serve as smoking gun evidence for DM annihilation. On top of these mono-energetic lines, the hadronic ($b\bar{b}$) and leptonic ($\mu\bar{\mu}$) decay channels will contribute continuous γ -ray spectra.

A continuum of γ -rays from inverse Compton-scattering on the galactic radiation field and synchrotron radiation from interactions with the galactic magnetic field dwells in the background. The synchrotron radiation is detectable by cosmic microwave background experiments. The inverse Compton scattering of these leptons on photons of the cosmic microwave background or the starlight results in MeV to GeV γ -rays and is accessible by instruments like Fermi LAT. In general the detection of photons is done via pair production in satellites (e.g. Fermi-LAT) or ground based air Cherenkov telescopes (e.g. MAGIC, HESS, CTA).

Several experiments like the PAMELA satellite, the Fermi LAT satellite, and others delivered constraints on DM models. For example PAMELA measured the ratio of positrons to electrons as well as the anti-proton to proton ratio up to energies in the few 100th-GeV-range. An anomalous positron excess has been detected while the measured anti-proton to proton ratio is in agreement with standard secondary production models of cosmic ray propagation in the galactic medium. Through this asymmetry DM models could be constrained, as they usually predict symmetric leptonic and hadronic secondary production. Standard astrophysics still offers many explanations for the positron excess, like nearby young pulsars or supernova remnants.

Before concluding this section it must be mentioned, that the interpretation as a clear signal for DM annihilation is not possible because of too little statistics or too large astrophysical systematic uncertainties.

Another and new way which opens the possibility of observing the phenomenon of DM, which seem to have no effects except gravitational, is the observation of gravitational waves as done in the detection by LIGO (in September 2015).

1.7.3. Dark Matter Production

Expecting DM particles to couple weakly to standard model particles it should be able to produce them in high energetic (SM-) particle collisions, what is called dark matter production. This fact is used to search for DM in particle colliders (like the LHC at CERN), requiring the collider to reach energies at least high enough to pair produce possible massive DM particles.

It is argued that the detection of particles beyond the Standard Model in collider experiments cannot resolve the question about the nature of the astronomically observed dark matter conclusively.

If the dark matter particle has a mass in the range of a few tens of GeV up to the maximum energy of the collider (≈ 13.8 TeV for the Large Hadron Collider - LHC), it can produce such a particle, and would deliver a good sensitivity for low mass DM particles. Unfortunately, it is impossible to determine the life-time of a produced neutral particle in a collider experiment if the life-time exceeds a collider specific value. Because a DM candidate needs to be stable on time scale of the universe $10^{10} \text{ y} \approx 3 \cdot 10^{17} \text{ s}$, and the particle detectors dimensions are about 3 m (what corresponds to 10^{-7} s by assuming speed of light), this results in a difference of 10^{24} orders of magnitude. Thus the LHC can provide only a dark matter particle candidate within a quite narrow mass range, since a collider experiment cannot probe the required stability of the particle. Also hadron colliders (like LHC) have very little sensitivity for DM candidates coupling to leptons.

Since particle physics detectors detect particles via the electromagnetic interaction, but DM particles do not interact via electromagnetic interaction (**dark!**), they do not leave any signature in the detector, but carry away energy and momentum, what results in a clear signature, the missing energy \cancel{E}_T .

In general there are two different detection scenarios. The first one is the direct production of two DM particles leaving the detector without signal ($\rightarrow \cancel{E}_T$). This method has less sensitive to the underlying DM model, allowing to put direct limits on the mass and interaction. The second scenario is the production of non-Standard Model particles (typical scenario for LSP in SUSY type models) decaying into DM candidates, with a signature in hadronic activity and \cancel{E}_T . ("LSP" means lightest supersymmetric particle.)

Because neutrinos do not interact with detectors and leave similar signal like DM particles (in context of missing transverse energy), they make up an irreducible background, which needs to be well understood. Events with $\gamma + Z_0 \rightarrow \nu\nu$ decays are the largest background contribution.

1.7.4. Axion Searches

Being a suited candidate for CDM, as pseudoscalar particle with very low mass (properties explained in 1.8.3), being neutral and extraordinarily weakly interacting, an axion (a) can be produced by the interaction of two photons

$$\gamma + \gamma \rightarrow a. \quad (36)$$

If one of the photons is a virtual one, this is known as the Primakoff effect. In an external electromagnetic field, this may result in the mixing of photons and axions. The conversion of an axion in a strong magnetic field due to the Primakoff effect and the subsequent detection of the resulting photon opens the field for the experimental search for the axion. The very weakly coupled axion is also very light because axion couplings and mass are proportional (see also 1.8.3). Three types of experiments are currently employed in the search for the axion: Photon regeneration experiments, axion helioscopes and resonator cavities.

Photon regeneration is best described by the catchy phrase "shining light through walls" experiments. Examples are the BFRT experiment, the BMV experiment and the GammeV experiment. Generally this methods do not rely on either astrophysical or cosmological sources. However the confirmation of the existence of a particle in the laboratory does not prove it is responsible for the effects of DM in the Universe. Before and behind a wall, magnetic fields are applied. In absence of axions (or ALPs), the light detector should measure no light. If axions (or ALPs) exist, such an experiment produces axions coherently by shining a LASER beam through a strong magnetic field and reconvert the produced axions in a collinear magnetic field on the other side of an optical barrier. Due to their low interaction rate, the axions could pass through the wall.

Axion helioscopes try to detect the axions produced in the core of the Sun (i.e. when X-rays scatter in strong electric fields) by converting them back to photons in a strong magnetic field. In the core of the Sun, axions would be produced with a thermal spectrum of a mean energy of ≈ 4.2 keV. By pointing a light detector behind an opaque shield permeated by a magnetic field into the direction of the sun, conversions of axions to photons are expected within this volume. An example for this method is the CAST experiment - the CERN Axion Solar Telescope.

The third technique is the resonant (and very weak) conversion of (dark matter) axions to radio-frequency photons in a microwave cavity permeated by a strong magnetic field. The shortcomings of this method is the fact, that only one resonance frequency can be checked at a time. This turns the measurement of a broader range of axion masses in a time consuming process. Today's most sensitive microwave cavity experiment is the ADMX experiment, which searches the galactic dark matter halo for resonant axions with a cold microwave cavity and has excluded optimistic axion models in the μeV range.

Also dark matter cryogenic detectors (like CDMS; or EDELWEISS which set coupling and mass limits) have searched for electron recoils that would indicate axions. Others like UORE and XMASS also set limits on solar axions, or XENON100, which set the best coupling limits to date and excluded some parameters.

There are also theories, that axions may be produced within neutron stars, by nucleon-nucleon bremsstrahlung. The subsequent decay of axions to gamma rays allows constraints on the axion mass to be placed from observations of neutron stars in gamma-rays using the Fermi LAT.

1.8. Dark Matter (Particle) Candidates

Within the previous sections, it has been shown that viable dark matter candidates must satisfy several conditions: They must interact very weakly with baryons and electromagnetic radiation, their relic density must be in agreement with the DM energy density and they must be non-relativistic (cold) to be allowed by the observed large scale structure of the Universe. From the point of particle physics, well motivated ideas of particle physics beyond the Standard Model which present viable candidates for dark matter exist, to mention just a few i.e. supersymmetry, extra dimensions and axions.

It should be noted that the presented list of candidates is by no means complete. Many other theories can provide candidates for dark matter.

Before presenting some viable candidates it should be reviewed, that some models has already been excluded in the course of the discussion in the previous sections, as there are the baryonic dark matter like MACHOs (as mentioned in section 1.3.4) and also a non-baryonic standard model candidate, the neutrino because it would act as hot dark matter that could not explain structure formation in the early universe and furthermore, the upper limit for its contribution to the normalized energy density is too small. Additional it shall be noted for MACHOs, even if they are objects like red and white dwarfs (which are not completely dark), the rotational curves of the galaxies cannot be explained by MACHOs. This amplifies the impact of the evidence celestial dynamics provide to the hypothesis of non-baryonic dark matter. In particular, as the predominant part of dark matter in our galaxy must be non-baryonic in the absence of MACHOs, the chance to detect it in direct or indirect searches is enhanced. Also the MOND theory has been excluded - see the end of the section Bullet Cluster at page 13.

Although there is no evidence for the particle character of dark matter, there are some well motivated approaches from the particle physic point of view. It seems straightforward to attribute DM to the existence of a neutral stable thermal relic particle, i.e. a particle which was in thermal equilibrium with all other particles in the early Universe for temperatures above its mass.

Generally, DM relics are considered to be produced in the early Universe in (at least) two distinct ways. One possibility involves DM particles generated in processes taking place in thermal equilibrium, generically referred to as thermal production (TP) with the relics produced this way called thermal relics. On the other hand, non-thermal production (NTP), will refer to processes taking place outside of the thermal equilibrium, and the resulting relics are called non-thermal relics. Focusing on the first class of processes, they include the freeze-out of relics from thermal equilibrium, or their production in scatterings and decays of other particles in the plasma.

While some DM candidates are created just to solve the DM problem, others emerge quite naturally from solutions to long standing problems in particle physics. In this latter category, notable candidates include the axion, which emerges from the Peccei-Quinn (PQ) solution to the strong CP problem and the neutralino which emerges from a supersymmetric solution to the gauge hierarchy problem. In cases such as these and others, the relic abundance of DM along with DM detection rates are calculable in terms of fundamental parameters, and thus subject to experimental searches and tests.

An overview of several well-motivated DM candidates in the mass vs. detection cross section plane is presented in figure 16. On the vertical axis a typical order of magnitude detection cross section associated with each type of candidate is shown. Just for reference, a SM neutrino with mass of order 0.1 eV and weak interaction strength of order $10^{-36} \text{ cm}^2 = 1 \text{ pb} \simeq 1 \text{ GeV}^{-2}/3.92$ is shown, although such a candidate would constitute hot DM (HDM) and thus does not meet the need (of its velocity not exceeding the escape velocity in galaxies) for cold relics (as mentioned before).

1.8.1. WIMP

Weakly interacting massive particles as non-baryonic cold DM are considered as one of the best candidates for DM. In figure 16 the box marked "WIMP" represents "generic" weakly interacting massive particle candidates as thermal relics. Their mass can lie in the range between a few GeV (below which it would overclose the Universe) and some ≈ 100 TeV from unitarity constraints. Their detection cross section is limited from above by direct DM search limits. As some properties have already been mentioned in section 1.7.1, it shall be mentioned again, that the strongest limits come from direct detection experiments like the Xenon100 experiment and the LUX experiment. A firm lower limit on the other hand does not really exist and can only be estimated on the basis of some kind of theoretical arguments of "naturalness". The underlying theories of WIMP DM require a discrete symmetry. The fact that the relic density obtained from thermal freeze out, which leads to a mass and cross section known from the electroweak theory (WIMP miracle), is an aesthetic argument and briefly explained in the following. In the early Universe WIMP particles χ are assumed to be in thermal equilibrium at temperature $T \gtrsim m_\chi$. For sufficiently high temperatures, such as those existing in the early Universe, the dark matter particle and its antiparticle would have been both forming from and annihilating into lighter particles. The relic density n_χ of a WIMP can be calculated with the Boltzmann equation:

$$\frac{dn_\chi}{dt} = -3Hn_\chi - \langle \sigma_{ann} v \rangle (n_\chi^2 - n_{eq}^2) \quad (37)$$

with n_χ the WIMP number density, n_{eq} the equilibrium density, H the Hubble constant and $\langle \sigma_{ann} v \rangle$ the thermal averaged WIMP annihilation cross-section times WIMP relative velocity. The Boltzmann equation can be solved only numerically, not analytically. As can be seen in the equation above (37), the change in density with time originates from several contributions. The first comes with the expansion of the universe (represented by the Hubble constant H) and dilutes the WIMP density n_χ . The next contribution is due to the annihilation of WIMPs, what reduces the WIMP density n_χ . And, although the WIMP density n_χ gets enhanced through the production of WIMPs from particles from the equilibrium n_{eq} , the number of produced WIMPs decreases exponentially with the Boltzmann factor $e^{-m_\chi/T}$ (because the number of particles with enough energy to create a pair of these particles decreases). As the Universe expanded and cooled, the average thermal energy of these lighter particles decreased and eventually became insufficient to form a dark matter particle-antiparticle pair. So the term "WIMP" is given to a

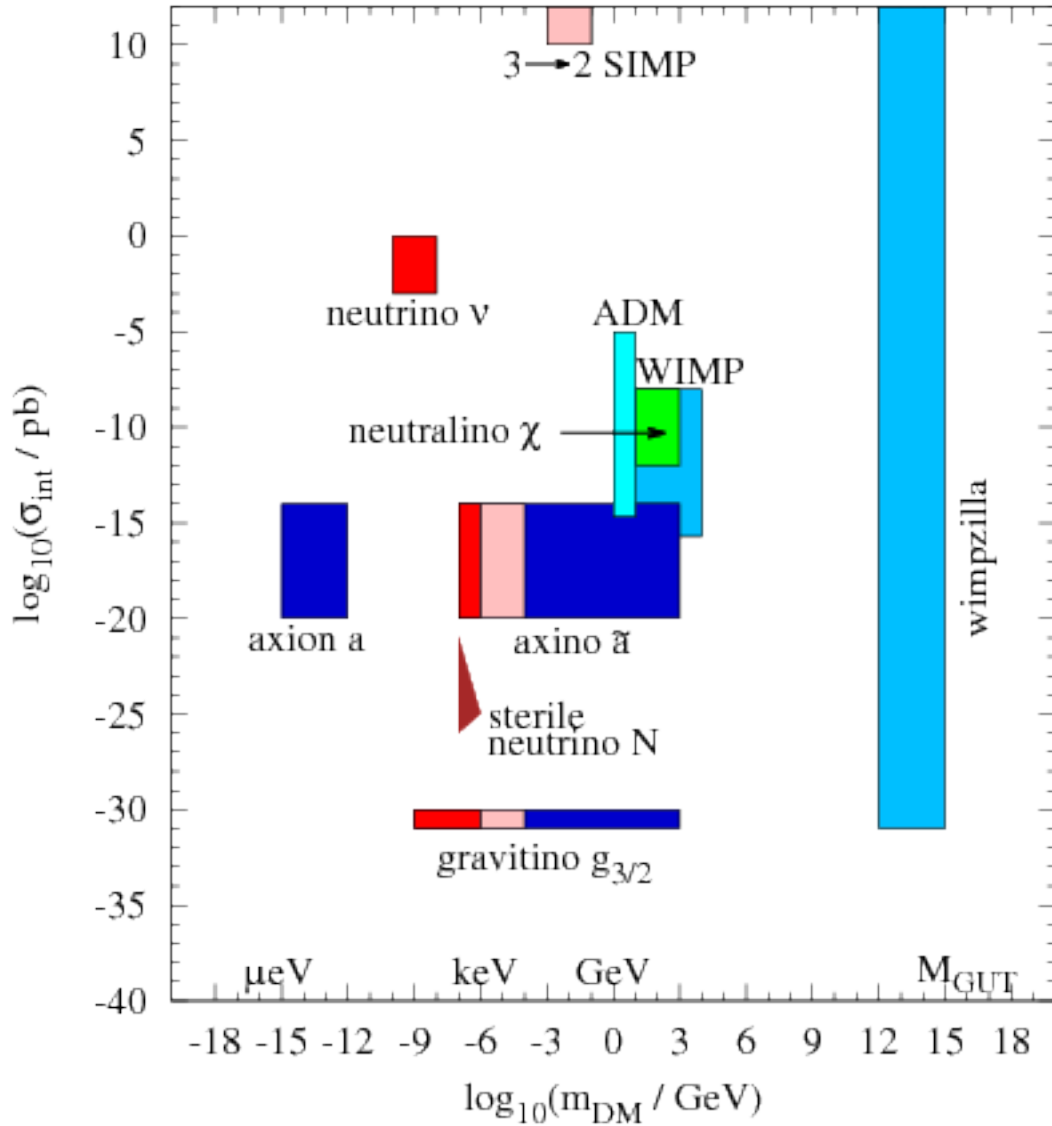


Figure 16: Several well-motivated candidates of DM are shown in the log-log plane of DM relic mass and σ_{int} representing the typical strength of interactions with ordinary matter. The red, pink and blue colors represent HDM, WDM and CDM, respectively. Figure taken from [30].

dark matter particle that was produced by falling out of thermal equilibrium with the hot dense plasma of the early universe. The annihilation of the dark matter particle-antiparticle pairs, however, would have continued, and the number density of dark matter particles would have begun to decrease exponentially. Eventually, however, the number density would become so low that the dark matter particle and antiparticle interaction would cease, and the number of these particles would remain (roughly) constant as the Universe continued to expand. This point with the temperature T_{fr} , where the Hubble term becomes dominant (a co-moving (expanding) volume) and the number density becomes effectively constant is the *freeze-out* point. This time (or energy) is $\approx m_\chi$ and the energy is below the energy required to pair produce a DM particle pair. The $\chi\chi$ pair is no longer in equilibrium and freezes out. Particles with a larger interaction cross section would continue to annihilate for a longer period of time, and thus would have a smaller number density when the annihilation interaction ceases.

Based on the current estimated abundance of dark matter in the Universe, if the dark matter particle is such a relic particle, the interaction cross section governing the particle-antiparticle annihilation can be no larger than the cross section for the weak interaction (order $\approx 10^{-36} \text{ cm}^2$ ($= 1 \text{ pb}$), Fermi scale). If this model is correct, the dark matter particle would have the properties of the WIMP. The cross section required to match the observed DM density in the universe leads to a cross section similar to that known from weak interaction (pb), assuming (here Fermi Theory) this would lead to a required DM of $\mathcal{O}(\text{GeV})$.

Because supersymmetric (for a brief explanation see sec. 1.8.4) extensions of the standard model of particle physics readily predict a new particle with these requested properties, this apparent coincidence is known as the "*WIMP miracle*", and a stable supersymmetric partner has long been a prime WIMP candidate.

Concluding this section, the main theoretical characteristics of a WIMP are that it interacts only through the weak nuclear force and gravity, or possibly other interactions with cross-sections no higher than the weak scale, and a large mass compared to standard particles. Because of their lack of electromagnetic interaction with normal matter, WIMPs would be dark and invisible through normal electromagnetic observations. Because of their large mass, they would be relatively slow moving and therefore "cold". Their relatively low velocities would be insufficient to overcome the mutual gravitational attraction, and as a result WIMPs would tend to clump together.

1.8.2. Asymmetric Dark Matter (ADM)

Another type of dark matter relic is called asymmetric dark matter (ADM) and can be produced via mechanisms similar to those which generate the baryon asymmetry. In this case, in contrast to the standard WIMP scenario, one postulates both DM and anti-DM particles where an asymmetry can develop between the two. In the early Universe, only the number density difference between the two (asymmetric component) remains after the annihilation of the symmetric components of DM and anti-DM. In this case, the relict abundance Ω_{dm} of ADM is set by the asymmetry in their initial populations, and not by the thermal freeze-out:

$$\Omega_{dm} \sim \eta_{dm} m_{dm}, \quad \eta_{dm} = \frac{n_{dm} - n_{\overline{dm}}}{s}, \quad (38)$$

with the entropy density s . Therefore the mass m_{dm} is related to the Ω_b/Ω_{dm} ratio [30]

$$m_{dm} = \frac{\eta_b}{\eta_{dm}} \cdot \frac{\Omega_{dm}}{\Omega_b} \cdot m_p, \quad (39)$$

with the proton mass m_p as typical baryon.

Some examples of ADM include technibaryons, mirror dark matter, scalar neutrinos, pure higgsinos and others. If the ADM is self-interacting or decaying, then various astrophysical signatures may arise. For example, decaying ADM might explain the cosmic positron excess or produce signatures in the gamma-ray sky.

1.8.3. Axion

Moving down the vertical axis (in fig. 16), the axion is a well known example of a *non-thermal* relic candidate for dark matter. It was postulated by the Peccei-Quinn theory in 1977 ([37]) to resolve the strong CP problem as a hypothetical elementary particle. (In particle physics, the strong CP problem is the puzzling question of why quantum chromodynamics (QCD) does not seem to break the CP-symmetry (there is no experimentally known violation), although according to QCD there could be a violation of CP symmetry in the strong interactions.) It prevents CP violation via an additional Peccei-Quinn symmetry, which breaks below the scale f_a (the axion decay constant). CP violating terms are allowed in \mathcal{L}_{QCD} but would result in an electric dipole moment of the neutron (NEDM), which has not been observed yet (Fine-tuning problem!).

On a more technical level, during the evolution of the universe it cools down below f_a and the axion appears as the pseudo-Nambu-Goldstone-Boson that results from the spontaneously broken Peccei-Quinn symmetry. However, the non-trivial QCD vacuum effects (e.g., instantons) spoil the Peccei-Quinn symmetry explicitly and provide a small mass for the axion. The coupling of axions to matter is $\propto f_a^{-1}$. Its interaction strength is strongly suppressed relative to the weak strength by a factor $(m_W/f_a)^2$ (where $f_a \approx 10^{11}$ GeV - the PQ breaking scale), resulting in its very light mass. As the axion radiation is an additional channel to transport energy out of stars, a too strong coupling would result in a too fast cooling of stars and supernovae. Astronomical observations set limits: $f_a > 10^7$ GeV and on the axion mass $m_a < 1$ eV. If it exists and has a low mass within a specific range, they are of interest as a possible component of cold dark matter.

As pseudoscalar particle, an axion can be produced by the interaction of two photons (as mentioned in 1.7.4 eq. (36)). If one of the photons is a virtual one, this effect is known as the Primakoff effect. In an external electromagnetic field, this may result in the mixing of photons and axions by the Lagrangian:

$$\mathcal{L}_{a\gamma\gamma} = g_{a\gamma} a \vec{E} \cdot \vec{B}. \quad (40)$$

The coupling constant $g_{a\gamma}$ is defined as:

$$g_{a\gamma} = \frac{\alpha g_\gamma}{\pi f_a} \quad (41)$$

with the electromagnetic fine structure constant α , the axion decay constant f_a and a constant g_γ which contains the dependence on the axion model. The scale of PQ symmetry breaking f_a is required to be $f_a \gtrsim 10^9$ GeV, otherwise supernovae cool too quickly. [30]

Beside the classic axion from the Peccei-Quinn symmetry, similar light particles exist in other theories, collectively called *axion like particles* (ALPs). ALPs may be observable, despite its small couplings, via the Primakoff effect (see 1.7.4), i.e. the conversion of an ALP to a photon in a magnetic field. So far, no ALPs were observed.

Some theorists claim, that any theory of DM which neglects the axion stands a good chance of being incomplete, as physicists have often considered either WIMP-only or axion-only theories of CDM for many years. In a SUSY extension of the SM (as explained briefly later), the newly measured Higgs boson mass can be in accord with theory, but then there is no solution for the strong CP problem. Nature seems to need both.

To complete this section it shall be described in short, why the model of axions was not applied for this work since it is a search for physics beyond the standard model. Because the CRESST-II detector Lise, which data was analysed, has a threshold of 300 eV and axions are expected in the sub-eV range, it would be unnecessary to set a limit or rather to transform the calculated limit (for Lise) in an axion parameter. There are other experiments (like XENON) which are better suited for the corresponding energy-range.

1.8.4. SUSY

Supersymmetry (SUSY) is the only non-trivial extension of the standard model (SM), as the Algebra of Supersymmetry is the only non-trivial extension of the Poincaré group and is a generalization of the space-time symmetries found in quantum field theory that allows the transformation of fermions (particle with half spin) into bosons (particles with integer spin), and vice versa like:

$$Q|\text{Fermion}\rangle = |\text{Boson}\rangle \quad \text{and} \quad Q|\text{Boson}\rangle = |\text{Fermion}\rangle . \quad (42)$$

An extension of the Standard Model is the minimal supersymmetric model (MSSM), in which each SM particle has a supersymmetric partner, squarks and the supersymmetric partners of the gauge bosons, gauginos. These partners should have the same mass as the SM particle. The simple MSSM extension has additional 120 parameters. But because no supersymmetric particles have been observed, or the mass of SUSY particles is different to the mass of the SM particles, the "SUSY is broken", what requests a breaking scenario. If the supersymmetry breaking mechanism is soft and the corresponding SUSY-breaking mass is in the range of a few TeV, the stability of the gauge hierarchy can be maintained.

A new form of parity is introduced, the so-called R-parity, which is a discrete symmetry (\mathbb{Z}_2) with a multiplicative quantum number $R = (-1)^{3B+L+2s}$ which is conserved (s is spin, B is baryon number, and L is lepton number). It prevents the proton decay and

at the same time ensures the stability of the the lightest supersymmetric particle (LSP) (can not decay into SM particles). This further results in SM particles having $R=+1$ and SUSY particles having $R=-1$ and SUSY particles being allowed to be produced only in pairs.

SUSY offers a solution to most of the remaining problems from the SM, whereof here three examples are mentioned. Starting with a excellent candidate for dark matter, the LSP, the Neutralino, a mixture of the neutral supersymmetric partners of the gauge bosons (a superposition of bino, photino and higgsino, the SUSY partners of the SM gauge bosons). Further, with SUSY the evolution of the three fundamental coupling constants meet at a single point with time, the grand unification scale (GUT). And the third example is the intrinsic relation to time-space of SUSY, which local invariance leads to a spin-2 particle, the graviton. Also the gravitino, the spin 3/2 SUSY-partner of the graviton, could act as a candidate for DM, interacting only via gravity and not weakly interacting. Even more candidates are allowed with introduction of SUSY models, e.g. the spin-1/2 axino \tilde{a} , the SUSY partner of the axion and the spin-0 saxion s .

It also provides a framework for the unification of particle physics and gravity possibly allowing an explanation of the gauge hierarchy of the electroweak scale to the Planck energy scale.

The axino is an example of an extremely-weakly interacting massive particle (E-WIMPs, or alternatively super-WIMPs or FIMPs (for feebly interacting massive particles)). The axino mass is strongly model dependent. In the case where \tilde{a} is the stable LSP, then it could comprise at least part of the DM. Axinos can be either thermal or non-thermal relics, or both, since they can be produced in both thermal and non-thermal processes. Depending on various conditions, they may comprise hot, warm or cold relics, or some combinations of say warm and cold DM.

The gravitino \tilde{G} , is another well-motivated example of an E-WIMP and shares several properties to the axino. It is a neutral Majorana fermion whose couplings to ordinary particles (and sparticles) are strongly suppressed - this time by the square of the Planck scale, $\approx (m_W/M_P)^2$. Like the axino, relic gravitinos can have contributions from both thermal and non-thermal processes, and they can be either hot, warm or cold DM.

1.8.5. Dark Photons (Vector Particles)

Just like ordinary matter couples to a long-range force known as "electromagnetism" mediated by particles called "photons", dark matter could couple to a new long-range force known (henceforth) as "dark electromagnetism", mediated by particles known (from now on) as "dark photons". (Another possibility could be, that DM couples to a relatively strong short-range force that could have interesting consequences for structure on small scales. [38])

One brief explanation would be imagining that there is a completely new kind of photon, which couples to dark matter but not to ordinary matter. The long-range gauge force is coupled to DM, in the form of a new unbroken abelian field, dubbed the $U(1)_D$ "dark photon" (V , hidden photons, A' , ...). So there can be dark electric fields, dark magnetic fields, dark radiation, etc. The dark matter itself consists half of particles with

dark charge +1, and half of antiparticles with dark charge -1. For these particles and antiparticles to all not annihilate into dark photons, there is a range of possibilities for which the dark matter does not annihilate very efficiently. For example, if the mass of the individual dark matter particles was sufficiently large, their density would be very low, and they just would not ever collide. Alternatively, if the strength of the new force was extremely weak, it just would not be that effective in bringing particles and antiparticles together. But this attitudes were already discussed in previous sections for similar problems.

For DM particles weighing several hundred times the mass of the proton, there should be about one DM particle per coffee-cup-sized volume of space. The strength of the dark electromagnetic force can be characterized by the dark fine-structure constant $\hat{\alpha}$. In comparison that ordinary electromagnetism is characterized by the ordinary fine-structure constant $\alpha = 1/137$. In a first approach, just considering to stop the DM particles from annihilating away, it turns out, that the upper limit on the dark fine-structure constant would be about the same. [38] It is remarkable that such large values were allowed.

However, a little more properties about the DM is known, like it is close to collisionless. If they would collide very often, all sorts of things would happen to the shape of galaxies and clusters and would be in contradiction to observations. Taking this into account another limit on the strength of dark electromagnetism can be estimated. Interactions should be sufficiently weak that dark matter particles do not "cool off" by interacting with each other in galaxies and clusters. That turns into a more stringent bound on the dark fine-structure constant of about an order of magnitude smaller, at $\hat{\alpha} < 10^{-3}$.

Further it can not be stated with perfect confidence that the DM really is effectively non-interacting. If a model like this is right, and the strength of dark electromagnetism is near the upper bound of its allowed value, there might be very important consequences for the evolution of large-scale structure. At the moment, it is a little bit hard (for calculational reasons) to figure out what those consequences actually are. What is proposed is the possibility, that DM is really a plasma, and to understand how structure forms, one needs to consider dark magnetohydrodynamics, what is a non-trivial task.

The idea of new forces acting on dark matter is by no means new. But what is exciting about dark photons is that they are much more natural from a particle-physics perspective. Typical models of quintessence and long-range fifth forces invoke scalar fields, which are comfortable to work with, but which by all rights should have huge masses, and therefore not be very long-range at all. In comparison is the possibility of considering the dark photons massless, like the ordinary photon, and that the dark photon comes from a gauge symmetry, also just like the ordinary photon, its properties are therefore completely natural.

Some physicists proposed not just dark photons, but a barrellfull of new dark fields and interactions ([39]), showing that these models manage to evade all sorts of limits one might worry about, from getting the right relic abundance to fitting it with constraints from primordial nucleosynthesis and the cosmic microwave background.

The model mentioned before would actually be simpler, because of the possible im-

pacts of this new long-range force in the dark sector on observable cosmological dynamics. Another difference between dark electromagnetism and a scalar force is that electromagnetism has both positive and negative charges and thus, both attractive and repulsive forces. (Scalar forces tend to be simply attractive, and get all mixed up with gravity.) So much more than a single species of dark matter could be imagined. For example what if two different types of stable particles exist that carried dark charge? Then there could be dark atoms, what would not be far from dark chemistry, what further would not let dark biology far behind.

(Of course the new U(1) symmetry could come from some string or GUT model, which would be another interesting thing to think about.) Correlating, there would also be a dark background radiation. But the dark sector (dark matter + dark radiation) decouples relatively early on (temperatures of order 10 GeV). After that, energy gets dumped into ordinary photons from other standard-model particles, but not into the dark photons; so soon, the dark temperature is lower than the ordinary temperature and that is why there is no problem with BBN or the CMB.

From here on a little more technical details are considered. Dark matter detectors discussed in section 1.7.1, which primarily probe elastic scattering of WIMPs on nuclei are also precise probes of light, weakly coupled, particles that may be absorbed by the detector material (for dark photon DM with mass in the ≈ 0.01 -100 keV range). This specific model of dark photons is the minimal model of dark matter comprised of a long-lived vector state V (dark photons) generated through inflationary perturbations in an initial dark photon condensate, or possibly other non-thermal mechanisms. The relevant parameters for this model are the mixing angle κ and the mass of the dark photon m_V . The analysis presented in this thesis addresses the model of a very light dark photon field as a (pseudo) vector $g_V V_\mu \bar{\psi} \gamma_\mu \psi$ (a (pseudo) vector too is: $g_A \mathcal{A}_\mu \bar{\psi} \gamma_\mu \gamma^5 \psi$) with ψ the the electron field, g_i parametrizes the dimensionless couplings, and V (and \mathcal{A}) are the fields of metastable but very long lived DM. The case discussed in this work corresponds to $g_V = e\kappa$, and the light mass m_V is protected by gauge invariance. Dark Photons can be super-WIMPs and they can be dark matter through non-thermally generated abundance.

Although freeze-out in this scenario is similar to that in the standard WIMP scenario, the long-range DM-DM interactions implied by the unbroken $U(1)_D$ may lead to considerably different DM phenomenology in the current Universe, and in particular in galactic halos. In this scenario, dark-matter halos are composed of an equal mixture of χ and $\bar{\chi}$.

More generally, a dark photon is any spin-1 boson associated with a new U(1) gauge field. That is, any new force of nature that arises in a theoretical extension of the Standard Model and generally behaves like electromagnetism. Unlike ordinary photons, these models often feature a dark photon that is unstable or possess non-zero mass, rapidly decaying into other particles such as electron-positron pairs. They may also interact directly with the known particles, like electrons or muons, if said particles are charged under the new force.

Dark photons would theoretically be detectable via their mixing with ordinary photons

(and subsequent effect on the interactions of known particles) what is the topic of the analysis carried out in this work, with results presented in chapter 4. Some works has already shown, that the coupling constant of the dark photon to electrons, $e\kappa$ (= coupling to all charged particles), can be probed to exquisitely low values, down to mixing angles as low as $\kappa \approx \mathcal{O}(10^{-15})$. [40] Some constraints and their descent for this model in the mentioned region are explained briefly.

In the simplest form of these theories the extra $U(1)_D$ gauge field mixes with the SM $U(1)$ hypercharge gauge field (see eq. (43)) with an additional kinetic term $(-\frac{\kappa}{2}F_{\mu\nu}V^{\mu\nu})$ in the Lagrangian, eq. (44). This mixing term provides a portal from the dark sector to the charged particles of the SM, with the mediators called dark photons denoted by (Vector) V_μ .

$$SU(3)_c \otimes SU(2)_L \otimes \overbrace{U(1)_Y \otimes U(1)_D}^{\text{via } \kappa} \quad (43)$$

It shall be noted, that this work concentrates on the Stuckelberg-type mass (eq. (45)) for the vector field of the model of direct detection of V, because m_V can be added easier, rather than being induced via the Higgs mechanism. [40] (Equally applying to the Higgsed version (the existence of a Higgs field charged under this $U(1)$) this also opens up additional possibilities for achieving the required cosmological abundance of V.)

The lagrangeian containing this effective kinetic mixing of strength κ between the dark photon (V) and photon (A) with respective field strengths $F_{\mu\nu}$ and $V_{\mu\nu}$, is

$$\mathcal{L} = -\frac{1}{4}F_{\mu\nu}^2 - \frac{1}{4}V_{\mu\nu}^2 - \frac{\kappa}{2}F_{\mu\nu}V^{\mu\nu} + eJ_{em}^\mu A_\mu, \quad (44)$$

where J_{em} is the electromagnetic current. The mentioned Stückelberg case (with a "hard photon mass") is:

$$\mathcal{L} \supset -\frac{1}{2}m_V V_\mu^2. \quad (45)$$

For the case where $m_V > 2m_{dm}$, the dark photons could quickly decay into a pair of DM particles. If the self interaction is strong enough, the dark matter can form a bound state with the dark photon being the mediator of dark matter self interaction. Two cases for the mass m_V with different properties are considered. If $m_V > 1$ MeV, the dark photon plays the roll of the mediator of the force of dark matter self interaction. And if the DM can form such a bound state, high luminosity colliders (like Belle II, SeaQuest, SHiP) could be used to study the property of this state(s). For $m_V < 1$ MeV, the here interesting region (because of the detectors), the dark photon can easily be cosmologically stable, and play the roll of dark matter. DM detectors (sensitive to electron recoils) can be used to detect both solar dark photon and dark photon dark matter. In principle, all the detectors designed for detecting axion DM can be used to detect dark photon DM.

Direct detection experiments such as CRESST-II, XENON10, XENON100 and XENON1T are able to place a very strong constraint on the dark photon mixing angle, down to

$\mathcal{O}(10^{-15})$, assuming that dark photons comprise the dominant fraction of dark matter (figure 32). This sensitivity to dark photon dark matter exceeds the indirect bounds derived from stellar energy loss considerations over a significant fraction of the available mass range.

Constraints to this model can be derived from two sides, first from astrophysical objects (stars), and second by energy injection from γ -rays (contributions to the diffuse photon background) originating from $V \rightarrow 3\gamma$ decays below the $e^+ + e^-$ -threshold. For the case, that dark photons contribute to a significant fraction of the dark matter cosmological abundance, the nowadays DM experiments are sensitive enough to compete with stellar energy loss bounds for $m_V > 10$ eV.

Requirements for stability of the V 's on the cosmological time scales can be derived from decays of sub-MeV Dark Photons, such as it should be light, below $2m_e$, what prevents the $V \rightarrow e^+e^-$ decay and shall have a small $\kappa \ll 1$, to slow down $V \rightarrow 3\gamma$. (This allows the vectors to have a lifetime greater than the Universe.)

(Diffuse) Gamma rays and CMB limits exclude Dark Photon DM heavier than \approx few 100 keV in the (m_V, κ) parameter space. Other important astrophysical limits are aspects of stellar emission (for the mentioned Stückelberg case), and also from horizontal branch (HB - appendix A.7) stars and red giants (RG), which are independent of the relic density of dark photon DM. [40] These astrophysical constraints on the mixing parameter κ can be seen in the figure(s) of the results of this work in chapter 4 as shaded regions. For the direct detection of solar Dark Photons (probably) liquid scintillators are again best suited. For Horizontal Branch (HB) stars, a $0.8M_\odot$ -star, which has an energy loss limited to 10% of the HB's luminosity ($L_{HB} = 60L_\odot$), is considered. [40] The sensitivity to larger m_V can be extended from constraints derived from RG stars. A categorization of the different types of stars can be seen in figure 17, for example the Horizontal Branch stars (HB) with a helium burning core.

Astrophysical limits are strong, but direct detection (for example CRESST, Xenon) can probe uncharted territory. The sensitivity of current direct detection experiments already excludes dark photon dark matter with a thermally generated abundance.

As shown in [40], matter effects are not very important (if $m_V \geq E_{th}$ the photoelectric threshold, some eV - depending on the material) and the problem reduces to the absorption of a massive non-relativistic particle with $e\kappa$ coupling to electrons. (The astrophysics bounds, on the other hand, are often derived in the regime $E_V \gg m_V$.)

An important aspect for the detection comes from the photo-ionization cross sections of ordinary photons. Because it can be huge, say, 10^7 bn, these compensating factor makes up for a tiny coupling $\kappa \ll 10^{-10}$ (and renders V stable on cosmological time-scale) and the absorption of \approx keV vectors can be looked for in electron band.

The Dark Photon absorption in comparison to a photon (massless, carrying momentum $|\vec{q}| = \omega$) comes from the non-relativistic dark vector carrying a negligibly small momentum $|\vec{q}| = m_V v_{dm} \approx \mathcal{O}(10^{-3})\omega$ (mass m_V), where v_{dm} is the dark photon velocity. Because both the photon wavelength and the DM Compton wavelength are much larger than the linear dimension of the atom, this difference has little effect on the absorption rate. In exact calculations for Dark Photon absorption (including medium effects) it can

be shown, that the absorption rate is given by the imaginary part of the polarization functions.

With all the mentioned properties, an approximation for the relation between the absorption cross sections is

$$\sigma_V(E_V = m_V) v_V \simeq \kappa^2 \sigma_\gamma(\omega = m_V) c, \quad (46)$$

where v_V is the velocity of the incoming DM particle (this relation is not exact and needs corrections) [40].

Also from [40] the absorption rate used for the calculated limit in chapter 4 is given by

$$\text{Rate per atom} \simeq \frac{\rho_{dm}}{m_V c^2} \cdot \kappa^2 \sigma_\gamma(\omega = m_V) c, \quad (47)$$

where ρ_{dm} is the local galactic DM energy density.

In comparison to axion-like-particle DM dark photon DM has certain advantages (with respect to direct detection), for example because of the absence of the V-decay to two photons, which removes the constraint from monochromatic X-ray lines (stringent constraint on axion-like keV-scale DM). Furthermore, the cross section for dark photons is significantly enhanced for small masses, relative to the cross section for absorption of axion-like particles.

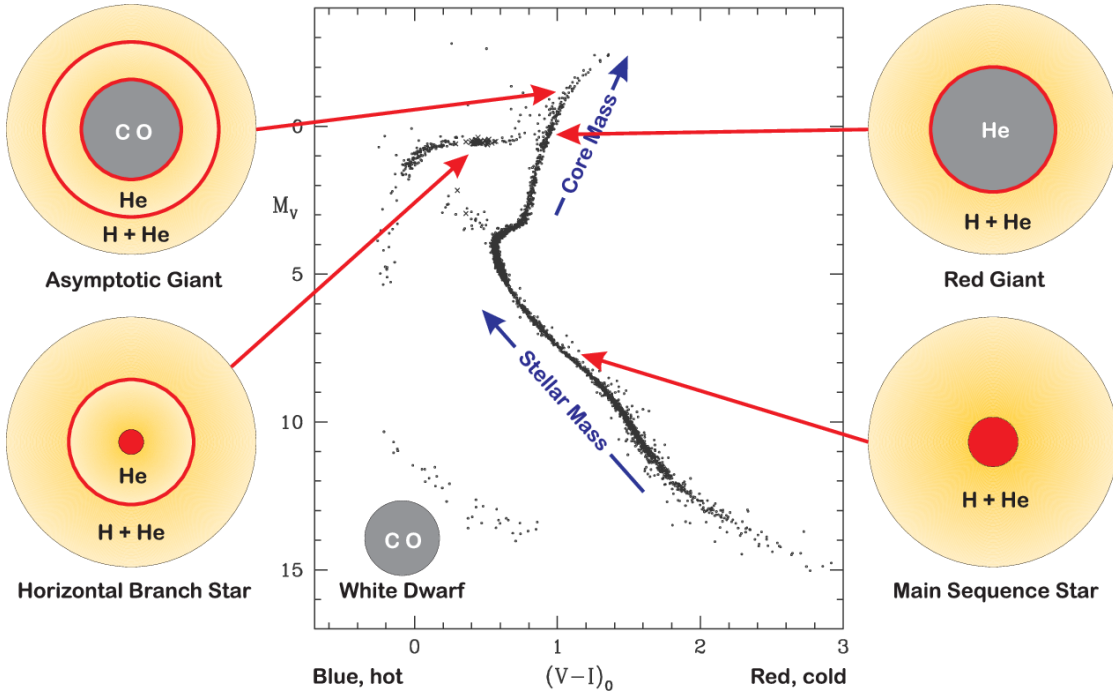


Figure 17: Schematic Globular Cluster color-magnitude diagram. The structure of stars corresponding to the different branches of the diagram are indicated. Figure taken from [41]

1.8.6. Alternative Theories

Many theorists have presented imaginable scenarios and theories in which additional to the space-time, which appears to consist of three space and one time dimension, further dimensions reveal themselves at higher energy scales. As examples of theories with extra dimensions string theory and M-theory shall be noted, which may be the best candidates for a consistent theory for quantum gravity and for the unification of all interactions. Such theories seem to require seven additional extra dimensions at least.

Finally, a wimpzilla (also represented in fig. 16) is an example of a nominally non-thermal relic. There are constraint on Ω_{dm} from the CMB which limit the maximum mass of a dark matter particle m_{dm} if it is a thermal relic of the early Universe. But there is still a possibility to evade this limit, and conceive super-heavy particles with masses $m_{dm} > 10^{10}$ GeV, if these particles were never in thermal equilibrium during freeze-out. If this is the case, then their relic abundance is not dependent on their annihilation cross-section but on their production cross-section. However, they have to be stable enough to contribute to the present day matter density. Cosmic rays at energies above the Greisen-Zatsepin-Kuzmin (GZK) cut-off observed by the AGASA experiment deliver the main motivation for superheavy DM particles. While it is not motivated by particle physics, it represents an alternative type of relic that can be produced in the early Universe by 1. classical gravitational effects, 2. through non-perturbative quantum effects during preheating, 3. from vacuum fluctuations in a first-order phase transition, or in addition, 4. under some circumstances it can also have a thermal population ([30]). Also like the most DM candidates suggested so far, Wimpzilla DM rely on exact or almost exact discrete symmetries. In contradiction to the AGASA result recent measurements of the ultra high energy cosmic ray spectrum confirm the GZK cut-off. An example is the AUGER experiment, which does not observe cosmic rays above the GZK cut-off, what states that the main motivation for superheavy dark matter has gone.

1.9. Conclusion

In all these sections in this chapter it has been shown, that the dark sector, i.e. dark matter might be complicated, with a rich phenomenology all its own, but so far without a satisfying solution. The Λ CDM is a nice, simple starting point for a theory of dark matter. But there are plenty of ideas, and some promising theories for DM were outlined, including the one most important for this work - dark photons. It is very tempting to think that observed deviations from the predictions of Λ CDM are due to some interesting new physics in the dark sector.

Still - all there is today are "minimal" properties ("minimal" means that the particles are cold and basically non-interacting with each other) and upper limits, but no firm conclusions. It is certainly possible that there is a lot of interesting physics going on in the dark sector, but is just too subtle for scientists to have noticed yet. So on the one hand it is important for theorists to propose specific, testable models of non-minimal dark sectors, so that on the other hand observers have targets to shoot for when trying to constrain just how interesting the darkness really is.

2. The CRESST Experiment

CRESST is an experiment designed for the direct detection of dark matter and is an acronym for Cryogenic Rare Event Search with Superconducting Thermometers. It is located in hall A of the Laboratori Nazionali del Gran Sasso (LNGS) underground laboratory between the towns of L'Aquila and Teramo in Italy, on average 1400 meters underground. Together with multiple passive shielding layers to reduce the background, the Gran Sasso massive is the first layer, serving to shield the setup against cosmic radiation (but due to the presence of natural radionuclides in the rock it is itself a source of radioactivity). Other background sources to the DM-particle-nucleus elastic scattering can be natural and induced radioactivity near the detector. Not only dark matter particles but also muons, neutrons, electrons, photons and alpha particles will interact in the detector.

Because a very low interaction probability is anticipated for dark matter particles massive detectors are needed to obtain a measurable interaction rate. Further the apparatus has to be decoupled from ambient vibrations and so, first of all, the cryostat hangs from a 20 cm thick wood plate which rests on air dampers. Secondly, to reduce the effect of vibrations created inside the cryostat from boiling cryogenic liquids, the detectors in the cold box are mounted onto a spring loaded support hanging from the cold finger. A sketch of the experimental setup of the CRESST-II Cryostat with the various (passive) shielding layers can be seen in figure 18.

The setup allows for the installation of up to 33 detector modules (*detector carousel*). From the inside out figure 18 shows the "cold box" surrounded by a 14 cm thick inner shield made of high-purity copper and a 20 cm outer shield made of lead, both to absorb electromagnetic radiation from the environment of the experiment. To eliminate radon contamination of surfaces close to the detectors, the next layer is the radon box, an air tight aluminium container, flushed by nitrogen gas (and maintained at a slight overpressure in order to prevent radon from penetrating the shielding). Outside the radon box, a muon veto is installed and the outermost shield is a 50 cm neutron moderator made from polyethylene. The muon veto system is installed inside the neutron moderator, suppressing the remaining neutron flux dominated by neutrons induced by muons in the lead of the shielding.

Because the momentum transfer of the neutron to a proton is maximal as their masses are similar, hydrogen-rich compounds are most effective for the purpose of neutron shielding. This is the reason for the large neutron stopping power of hydrogen-rich materials like water or polyethylene, with both materials roughly having the same density ($\approx 1 \text{ g/cm}^3$). The advantage of polyethylene (PE) is, that it is solid at room temperature, thus a neutron shielding around a given detector setup is easier to build and maintain with PE than with water. Unfortunately, both materials contain isotopes which allow (α, n)-reactions for rather low incident α energies.

Although the background is highly suppressed due to locating the experiment underground, using passive shielding layers, increasing radio-purity and applying a simultaneous read-out of light and phonon channel, one of the main parts of the remaining background, originates from neutron nuclear recoils which have a characteristic similar

2. THE CRESST EXPERIMENT

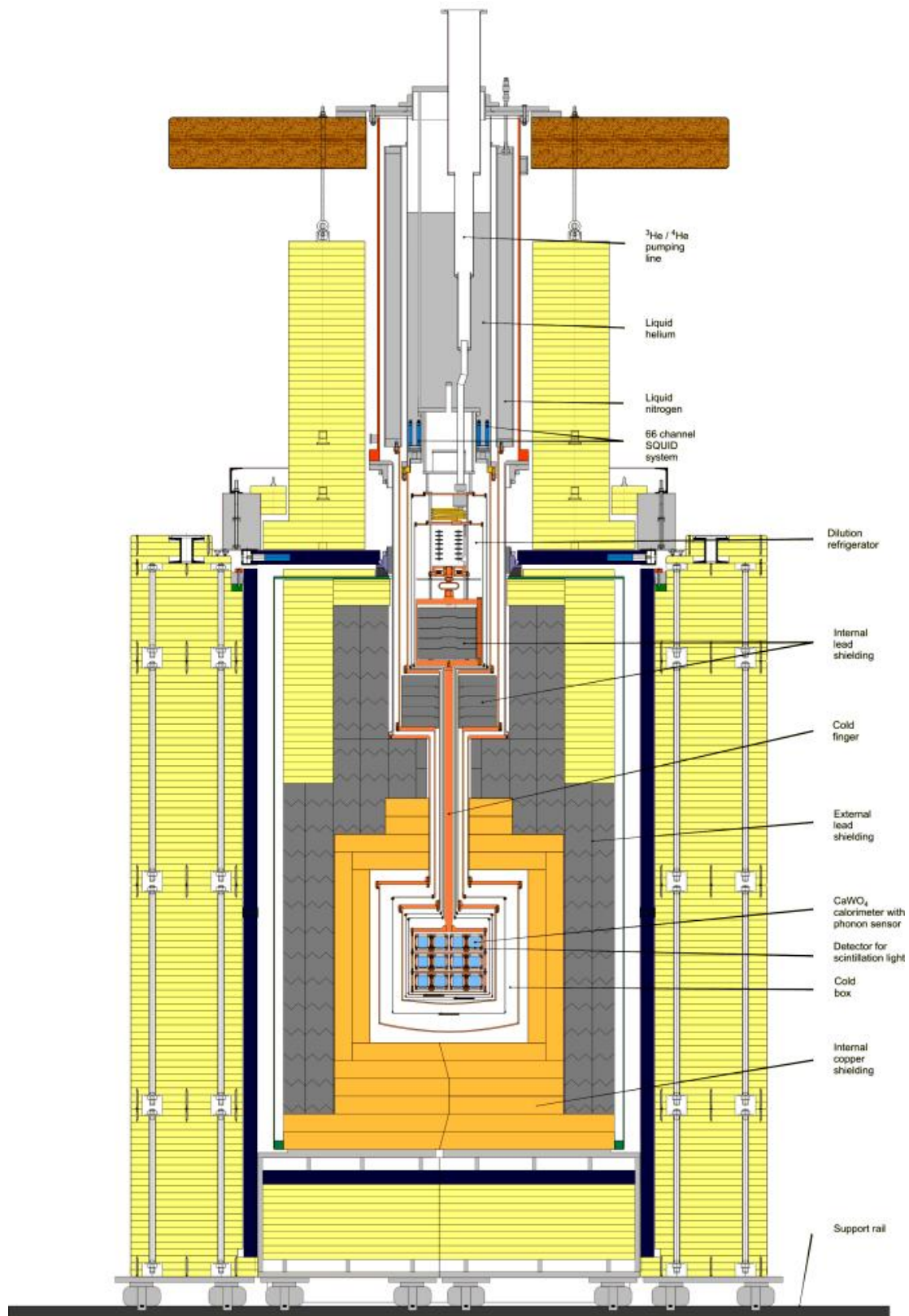


Figure 18: This figure shows a sketch of the experimental setup of the CRESST-II Cryostat, taken from [42].

to WIMP nuclear recoils. These neutrons that might reach the detectors can be produced by spontaneous fission of heavy elements, by (α, n) -reactions on light nuclei, or by muons. If they are produced outside the PE shielding (moderator for neutrons with energies up to some MeV), they have a very low contribution to the background, but if they are produced inside the shielding or the detector itself, then they can contribute to the background more significantly.

Because it is anticipated that the recoil energy of the struck nucleus is small, with most of the events in the keV region and below the detectors are operated in $^3\text{He}/^4\text{He}$ dilution refrigerators at about 10-15 mK, where superconducting phase transition thermometers (tungsten films) become superconducting, offering the ability to observe these small energy deposits.

As mentioned a little bit more detailed in section 1.7.1, in this energy region, detectors are prone to a wide variety of background events, what requests a proper discrimination of the spurious events. This is achieved due to the simultaneous read-out of two independent signal channels of the detector, since a particle scattering off a nucleus in the detector produces heat in the form of phonons and additional scintillation light. This also allows to discriminate the various sources of the energy deposition via the ratio of the two signal strengths.

The discrimination of the particle type becomes possible by the *light yield* of a given event in the detector. If energy is deposited by a recoiling nucleus, the light is *quenched*, compared to an energy deposit by an electron or by a lighter particle, where less scintillation light is produced in the crystal. Because the produced amount of light differs for different kinds of particles, most common backgrounds (e.g. electron recoils, alpha events, ...) can be eliminated. This is a very efficient way of *active* background discrimination, achieved using this so-called light yield, which is defined as the fraction of light and heat energy as discrimination parameter, showed in figure 19.

The horizontal bands in this schematic drawing (figure 19) shown in the light yield - energy plane are the mentioned results from the different event types. Per definition the light yield is normalized to 1 for gamma radiation with an energy of 122 keV (^{57}Co , calibration source), what results in a light yield of β 's and γ 's (electron recoils) of about 1. For α particles the light yield is about 0.22 and for nuclear recoils (O, Ca, W) it is even lower (0.1 - 0.02). [43] Due to finite detector resolution, these bands can be separated to some extent.

The achieved high resolution in combination with total energy measurement and high sensitivity, what made cryodetectors being the natural instrument for the direct detection of dark matter, can also be used to search for signatures of other models like dark photons (done in this work, sec. 1.8.5), but can also open completely other fields, for example observations of low energy neutrino scattering, (neutrinoless) double beta decay, detection of large biomolecules, and the detection of microfractures. More details on the light yield, the resolution, the calibration, cuts (quality cuts, coincidence cuts, rise-time cuts) and further properties can be found in [44] and [45].

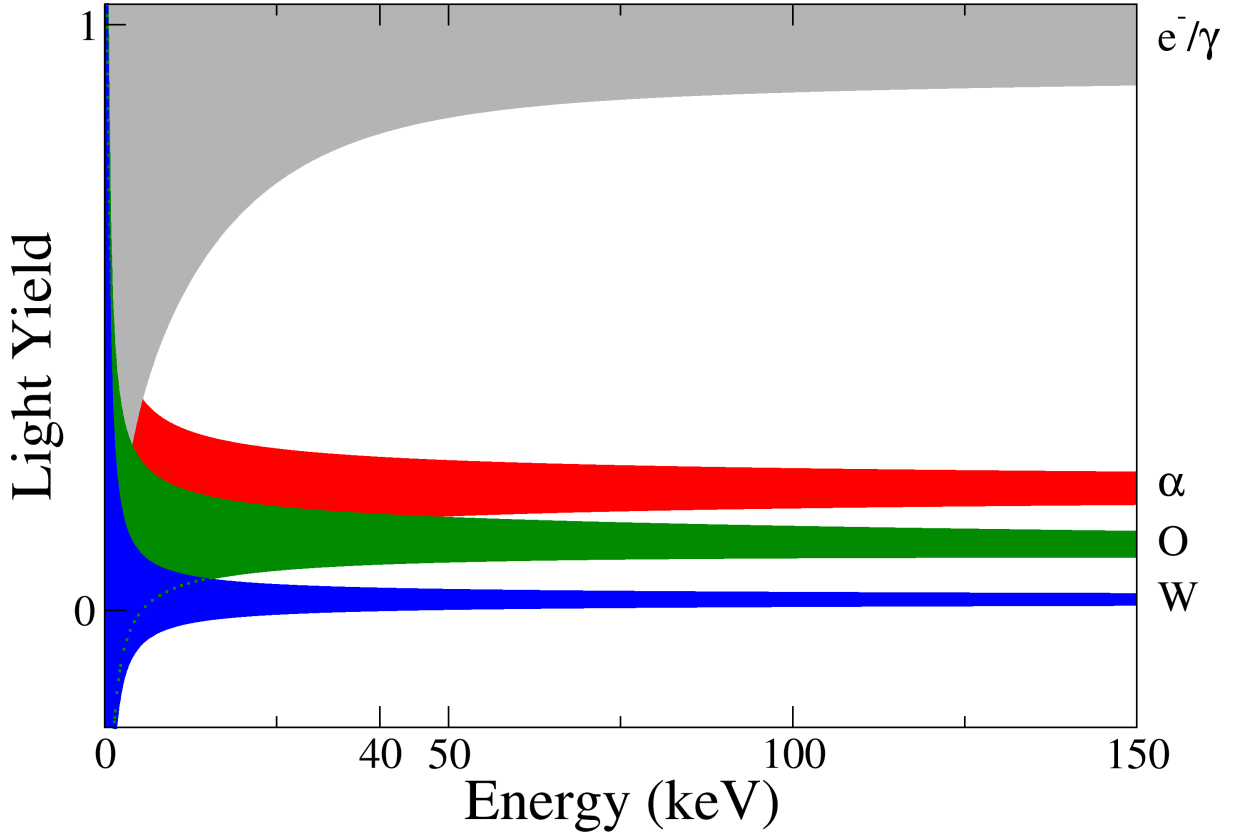


Figure 19: This figure shows a schematic drawing of the horizontal bands resulting from different event types in the light yield-energy plane, taken from [43].

2.1. Phases

The data for the analysis of this work are taken from the **CRESST-II Phase 2** run detector module **Lise**, the other phases are just mentioned briefly.

In CRESST-I sapphire crystals (Al_2O_3) were used as target material, it started in 1999 and published data for WIMP cross section in 2003.

2.1.1. CRESST-II

For this phase scintillating CaWO_4 crystals (more details see sec. 2.2) as absorbers were developed, in which as for sapphire a particle interaction produces mainly heat in the form of phonons. Additional to CRESST-I is the two channel read out (added the detection of scintillation light), and the integration of the carrier of the 33 detector modules (detector carousel) plus the SQUID system. The statistical fluctuations were reduced and the energy resolution improved.

In CRESST-II Phase 1 detector modules with a mass of ≈ 300 g were installed, a total net exposure of about 730 kg days was collected (complete data set) and it was operating from 2009 till 2011.

For the next run, the extended dark matter run CRESST-II Phase 2 (began in July

2013 and ended in August 2015) 18 detector modules of four different module designs were installed. The final module composition in the detector carousel were 12 modules of the conventional design, 2 modules with stick design, 2 modules with carrier design and 2 modules with silicon beaker design. Lise, where the data for this work are taken from, is a type of the conventional design.

As light detector, which is also operated as cryogenic calorimeter, a light absorber (usually silicon on sapphire) was combined with a second thermometer.

In general for all designs both detectors are mounted close to each other forming a detector module and are enclosed in a scintillating and reflective housing for an efficient light collection.

As already mentioned, the temperature sensors are superconducting phase transition thermometers (transition edge sensors - **TES**), consisting of thin tungsten films evaporated onto a surface of the absorbers. A small temperature rise leads to a relatively large increase in resistance, because the thermometers are stabilized in the transition from the normal conducting to the superconducting phase.

A schematic sketch of the conventional design (Lise) can be seen in figure 20.

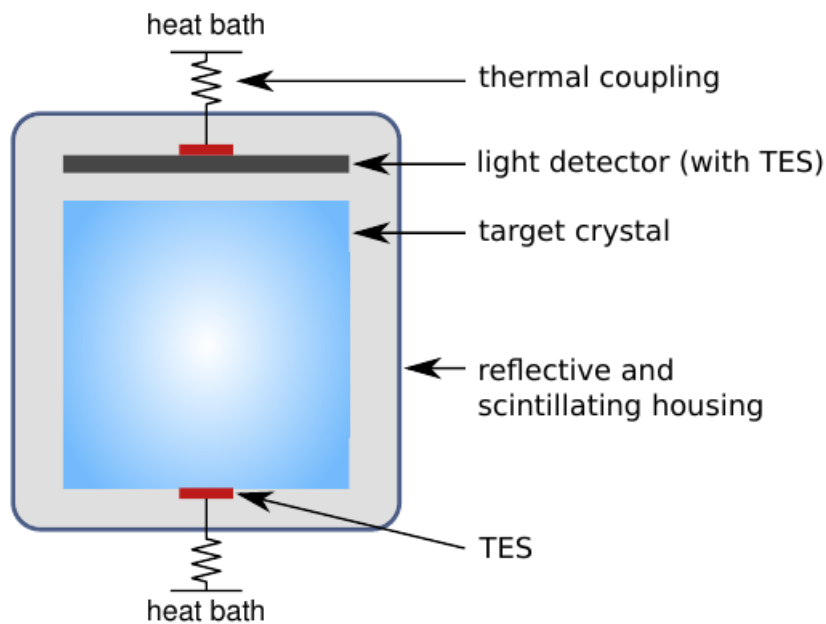


Figure 20: This figure shows a schematic sketch of the conventional design of the CRESST-II detector module, taken from [43].

Figure 20 shows, that a module consists of a phonon detector (CaWO_4 single crystal) and a light detector (Si or Si on Al_2O_3). They are mounted together in a reflective and scintillating housing. Both detectors are equipped with a tungsten TES, which then is read-out with a squid system. Thus the heat and the simultaneously produced light signal can be recorded together.

Because in the conventional module both detectors are held by non-scintillating bronze clamps which might lead to a difficult background contribution due to surface α decays,

large efforts were put into radon prevention to reduce this background.

A picture of the Lise-type module can be seen in figure 21.

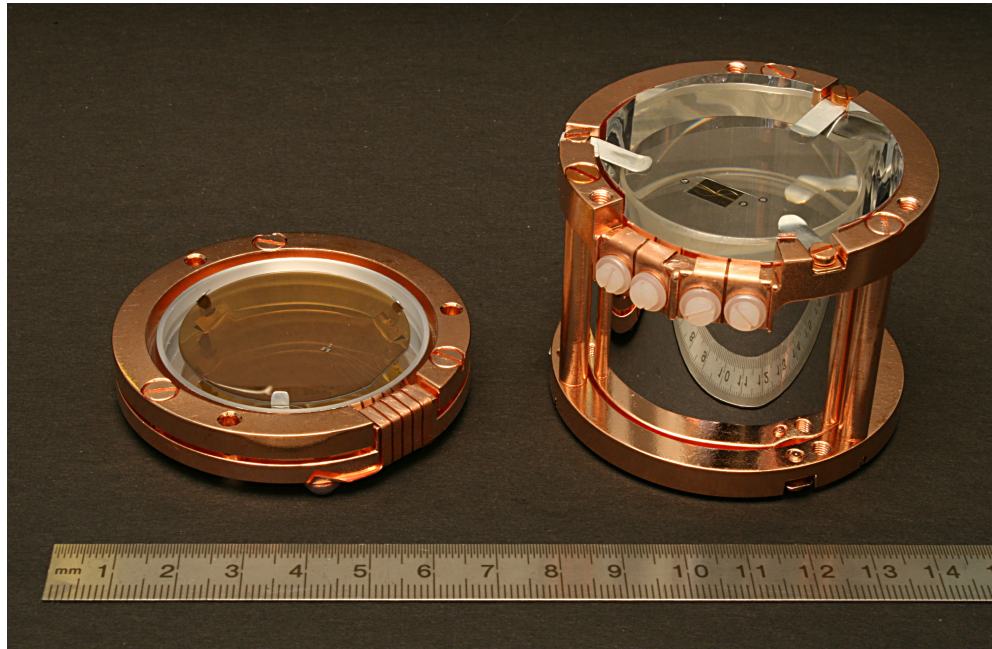


Figure 21: This is a picture of the Lise detector module (conventional design), on the left is the light absorber for scintillation-light detection, with a silicon-on-sapphire disc with a diameter of 40 mm and a thickness of 500 μm , and on the right is the phonon detector, where on top are the three clamps (bright) holding the crystal and the W-thermometer (TES, dark rectangle) on top of the CaWO_4 -crystal, taken from [43].

Lise had the lowest threshold (for nuclear recoils) in CRESST-II Phase 2 of ≈ 0.3 keV (solely arising from a superior performance of the phonon detector). In comparison to the module "TUM40" (stick design; the module with the best overall performance of CRESST-II Phase 2) the radio-purity of the commercial crystal installed was worse by a factor of ≈ 2 below 40 keV. The whole data set of Lise had an exposure of 52 kg days and due to the excellent threshold extends the exclusion limit for the first time down to the sub-GeV region.

2.1.2. CRESST-III

CRESST-III Phase 1 started in June 2016, where ten newly designed detector modules (including crystals with a mass of only ≈ 25 g each) are installed. Due to the decreased mass the sensitivity will be significantly increased and the detectors are expected to reach thresholds below 100 eV allowing a further investigation of signatures in the low-mass region.

2.2. Calcium tungstate CaWO_4

Calcium tungstate, also known as Scheelite, named after Karl Wilhelm Scheele (1742 - 1786), a Swedish chemist, is an example of an inherently fluorescent mineral. The crystal structure consists of tetrahedral WO_4^{2-} anions bonded to calcium Ca^{2+} cations ionically, distributed throughout the lattice. The crystal morphology is typically dipyramidal.

Each calcium atom shares corners with eight adjacent WO_4 tetrahedra. Each tungsten is bound primarily covalent to four oxygen atoms to form a tetrahedron slightly squashed ($\approx 7\%$) along the c -axis. The structure can be seen in figure 22 with the value for the lattice parameters a and c at a temperature of 300 K. CaWO_4 has a molecular weight of 287.93 g, is an intrinsic scintillator with high light yield and high thermal quenching temperature.

Regardless of the physical appearance of Scheelite, all samples have a characteristic intense blue-white fluorescence when stimulated by short-wave UV-radiation. The fluorescence in Scheelite is caused by transitions of electrons within the tetrahedral tungstate anion. [46]

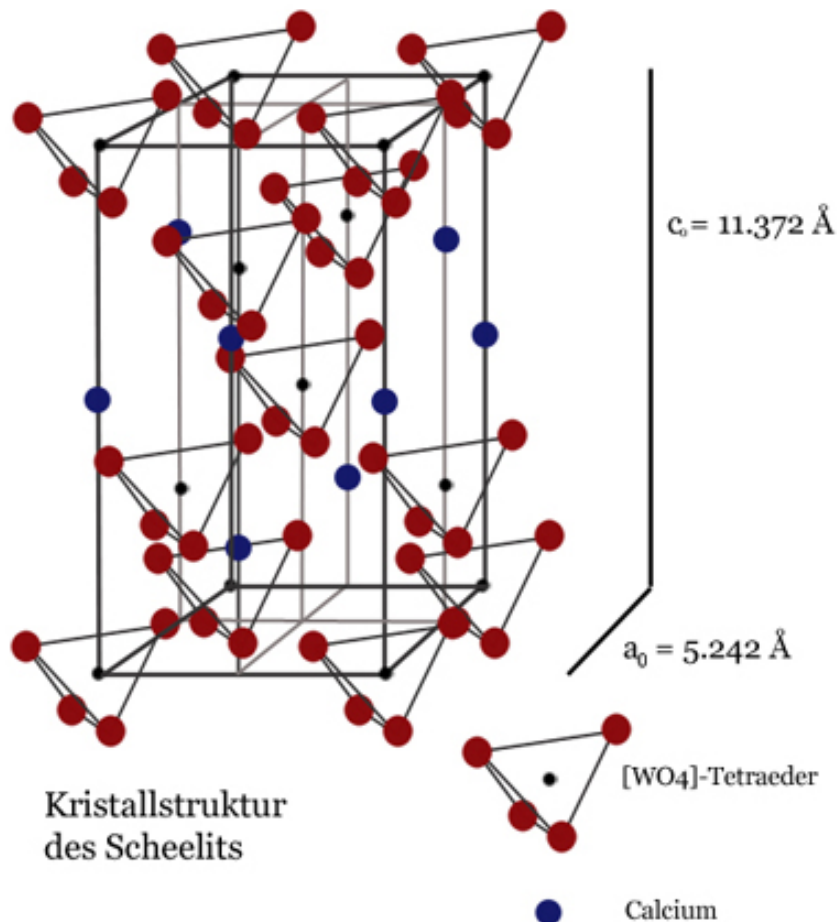


Figure 22: The structure of CaWO_4 , taken from [47].

3. Statistics

This chapter gives an explanation of the basic principles and fundamental concepts of the statistic methods necessary for the data analysis of this work. The aim was to calculate an (unbinned) 90% frequentist upper limit for the data of the CRESST-II Phase 2 Lise detector module. And for the search for physics beyond the standard model convert this limit on the dark photon mixing κ (section 1.8.5). A basic overview is given on what the frequentist probability, a probability density function (pdf), a test statistic, hypothesis testing, a maximum (extended) likelihood (ratio) is, and what in the context of frequentist likelihood ratio a 90% upper limit means.

Statistics can be seen as a branch of mathematics or as a mathematical body of science that pertains to the collection, analysis, interpretation or explanation, and presentation of data and it is concerned with the use of data in the context of uncertainty and decision making in the face of uncertainty. Probability is useful to help explain this uncertainty and variation/variability.

The mathematical theory of probability has a history dating back at least to the 17th century, and several different definitions of probability have been developed. A great discovery of twentieth century physics was the probabilistic nature of physical phenomena at atomic scales, described in quantum mechanics. Like other theories, the theory of probability is a representation of probabilistic concepts in formal terms. The central objects of probability theory are random variables, stochastic processes, and events: mathematical abstractions of non-deterministic events or measured quantities that may either be single occurrences or evolve over time in an apparently random fashion. There have been at least two successful attempts to formalize (modern) probability, namely the *Kolmogorov* formulation and the *Cox* formulation. The axiom system presented by Kolmogorov combined the notion of sample space (introduced by Richard von Mises) and measure theory. In Kolmogorov's formulation, sets are interpreted as events and probability itself as a measure on a class of sets. In Cox's theorem, probability is taken as a primitive (that is, not further analysed) and the emphasis is on constructing a consistent assignment of probability values to propositions.

The following definitions and formalism are in terms of set theory as formulated in 1933 by Kolmogorov ([48]).

Probability theory considers measures that assign to the whole set the size 1 ($P(S) = 1$), and considers measurable subsets to be events whose probability is given by the measure. Taking a set S called the *sample space* (which relates to the set of all possible outcomes in classical sense) consisting of a certain number of elements (leaving the interpretation open for the moment). (A set is a collection of some elements, whereat capital letters are often used to denote a set. To define a set all the elements can simply be listed in curly brackets, for example the set of integers, $\mathbb{Z} = \{\dots, -3, -2, -1, 0, 1, 2, 3, \dots\}$.) To each subset A of S (set A is a subset of set S if every element of A is also an element of S , written as $A \subset S$) one assigns a real number $P(A)$ called a **probability**. $P(A)$, quantified as a number between 0 and 1 (where 0 indicates impossibility and 1 indicates certainty), is the measure of the **likelihood** that an event (from a sample space) will occur ($0 \leq P(A) \leq 1$). A variable that takes on a specific value for each element of the

set S is called a *random variable*. The individual elements may each be characterized by several quantities, in which case the random variable is a multicomponent vector.

A *Probability Model* lists the possible outcomes of the experiment and the associated probability of each outcome displayed in a table, by a graph, or by a formula (section 3.2).

3.1. Interpretation of probability

Although any function can be called by definition a probability function, which satisfies the axioms defining probability ([48], [49]), it must still be specified how to interpret the elements of the sample space and how to assign and interpret the probability values. Commonly used in data analysis are two main interpretations of probability, called *objective* and *subjective* probability. (Some prefer to categorize in "physical" and "evidential" probabilities.)

Used among other things for assigning statistical errors to measurements, the most important is that of **relative frequency** (objective). The other interpretation (subjective probability) is also used, e.g. to quantify systematic uncertainties. When it comes to practical application however, there are two major competing categories of probability interpretations, whose adherents possess different views about the fundamental nature of probability:

- The most popular version of objective probability is **frequentist** probability, which claims that the probability of a random event denotes the relative frequency of occurrence of an experiment's outcome, when repeating the experiment (very often). This interpretation considers probability to be the relative frequency "in the long run" of outcomes. (A modification of this is *propensity probability*, which interprets probability as the tendency of some experiment to yield a certain outcome, even if it is performed only once.)

In the frequentist interpretation, probabilities are discussed only when dealing with well-defined random experiments (or random samples). Physical probabilities, which are also called objective or frequency probabilities, are associated with random physical systems such as roulette wheels, rolling dice and radioactive atoms. As mentioned above, an event is defined as a particular subset of the set of all possible outcomes of a random experiment (called the sample space of the experiment). In such systems, a given type of event (such as a die yielding a six) tends to occur at a persistent rate, or "relative frequency", in a long run of trials. For any given event, only one of two possibilities may hold: it occurs or it does not. The relative frequency of occurrence of an event, observed in a number of repetitions of the experiment, is a measure of the probability of that event. This is the core conception of probability in the frequentist interpretation. Physical probabilities either explain, or are invoked to explain, these stable frequencies. The two main kinds of theory of physical probability are frequentist accounts and propensity accounts.

Frequentist probability, frequency interpretations or frequentism is a standard interpretation of probability, it is empirical, defined by a ratio from an infinite series of trials, what can be understood as a very natural interpretation for scientific experiments, but from the mathematical point of view there are doubts of the convergence properties of the non-mathematical series.

If n_t is the total number of trials and n_x is the number of trials where the event x occurred, the probability $P(x)$ of the event occurring is the relative frequency and, as the number of trials is increased, one might expect the relative frequency to become a better approximation of a "true frequency", with the claim, that in the "long run", as the number of trials approaches infinity, the relative frequency will converge exactly to the true probability:

$$P(x) = \lim_{n_t \rightarrow \infty} \frac{n_x}{n_t}. \quad (48)$$

The development of the frequentist account was motivated by the problems and paradoxes of the previously dominant viewpoint, the classical interpretation. In the classical interpretation, probability was defined in terms of the principle of indifference, based on the natural symmetry of a problem (e.g. the probabilities of dice games arise from the natural symmetric 6-sidedness of the cube). This classical interpretation stumbled at any statistical problem that has no natural symmetry for reasoning.

- The other main interpretation, subjective probability, considers degrees of belief (or "*bias*"). All practical "subjective" probability interpretations are so constrained to rationality as to avoid most subjectivity. Real subjectivity is repellent to the sciences, which strive for results independent of the observer and analyst. The historical roots of this concept extended to such non-numeric applications as legal evidence.

Subjectivists assign numbers per subjective probability, i.e. as a degree of belief, interpreted as, "the price at which you would buy or sell a bet that pays 1 unit of utility if E, 0 if not E". The most popular version of subjective probability is **Bayesian** probability, which includes expert knowledge as well as experimental data to produce probabilities. The expert knowledge is represented by some (subjective) *prior probability* distribution. These data are incorporated in a likelihood function, whereat the product of the prior and the likelihood, normalized, results in a *posterior probability* distribution that incorporates all the information known to date. Bayesian probability is a quantity that is assigned to represent a state of knowledge, or a state of belief.

The elements of the sample space correspond to hypotheses or propositions, i.e. statements that are either true or false. (When using subjective probability the sample space is often called the hypothesis space.) One interprets the probability associated with a hypothesis as a measure of degree of belief: $P(A)$ = degree of belief that hypothesis A is true.

One of the many applications of *Bayes' theorem* (see eq. (49)) is Bayesian inference, a particular approach to statistical inference. With the Bayesian probability interpretation the theorem expresses how a subjective degree of belief should rationally change to account for evidence. Bayesian inference is fundamental to Bayesian statistics.

It is named after Thomas Bayes (1701-1761), who provided an equation that allows new evidence to update beliefs. It was further developed by Pierre-Simon Laplace, who first published the modern formulation. Sir Harold Jeffreys put Bayes' algorithm and Laplace's formulation on an axiomatic basis. Jeffreys wrote that Bayes' theorem "is to the theory of probability what the Pythagorean theorem is to geometry".

Bayes' theorem is stated mathematically as the following equation

$$P(A | B) = \frac{P(B | A) P(A)}{P(B)}, \quad (49)$$

where A and B are events and $P(B) \neq 0$. $P(A)$ and $P(B)$ are the probabilities of observing A and B without regard to each other, $P(A | B)$ is a conditional probability, the probability of observing event A given that B is true and $P(B | A)$ is the probability of observing event B given that A is true.

Here $P(A)$ (or $P(\text{theory})$) represents the **prior probability** that the theory is true, and $P(B | A)$ (or $P(\text{data} | \text{theory})$), called the **likelihood**, is the probability, under the assumption of the theory, to observe the data which were actually obtained. The **posterior probability** that the theory is correct after seeing the result of the experiment is then given by $P(A | B)$ (or $P(\text{theory} | \text{data})$). The prior probability for the data $P(B)$ (or $P(\text{data})$) says how one's degree of belief should change in the light of experimental data.

Summarising these two mentioned main categories in short:

- For the frequentist approach a hypothesis is a proposition (which must be either true or false), so that the frequentist probability of a hypothesis is either one or zero. In Bayesian statistics, a probability can be assigned to a hypothesis that can differ from 0 or 1 if the true value is uncertain.
- In the Bayesian view, a probability is assigned to a hypothesis, whereas under frequentist inference, a hypothesis is typically tested without being assigned a probability.
 - The frequentist "school" of statistics restricts itself to making statements of the form "probability of the data given the hypothesis". The definition of probability in this context is based on a limit of frequencies of various outcomes. In that sense it is objective.

- The Bayesian "school" of statistics allows one to make statements of the form "probability of the hypothesis given the data", which requires a prior probability of the hypothesis. Often the definition of probability in this context is a "degree of belief".

Clearly the probabilities based on such models can never be determined experimentally with perfect precision. The basic tasks of classical statistics are to estimate the probabilities (assumed to have some definite but unknown values) given a finite amount of experimental data, and to test to what extent a particular model or theory that predicts probabilities is compatible with the observed data.

The relative frequency interpretation is straightforward when studying physical laws, which are assumed to act the same way in repeated experiments. The validity of the assigned probability values can be experimentally tested. This point of view is appropriate, for example, in particle physics, where repeated collisions of particles constitute repetitions of an experiment, but the concept of relative frequency is more problematic for unique phenomena (such as the big bang).

As an interpretation, the frequentist method is not in conflict with the mathematical axiomatization of probability theory, rather, it provides guidance for how to apply mathematical probability theory to real-world situations. It offers distinct guidance in the construction and design of practical experiments, especially when contrasted with the Bayesian interpretation. As to whether this guidance is useful, or is inclined to misinterpretation, has been a source of controversy. (Particularly when the frequency interpretation of probability is mistakenly assumed to be the only possible basis for frequentist inference.) The Jeffreys-Lindley paradox shows how different interpretations, applied to the same data set, can lead to different conclusions about the 'statistical significance' of a result.

The beauty of probability theory is, that it is applicable regardless of the interpretation of probability that is used (i.e., in terms of long-run frequency or degree of belief). Probability theory provides a solid framework to study random phenomena. It starts by assuming axioms of probability, and then building the entire theory using mathematical arguments.

3.2. Probability density function

Any random variable will take a certain values with a certain probability. The function that controls these probabilities is in general called the probability mass function (pmf) in the context of discrete random variables (random variables that take values on a discrete set), while the **probability density function (p.d.f.)** is used in the context of continuous random variables (important for this work) as the relative likelihood for this random variable to take on a given value.

The value of the pdf at a certain value of the random variable will give a point on the graph of the pdf for that variable. For finding the probability in the continuous case, one can find that area under the curve of the pdf between two points on the range of the random variable. In addition to the (pmf and) pdf there is another important concept, or

function, called the *Cumulative Distribution Function* (cdf). The cdf ($F_X(x)$) is defined all over the real line regardless whether the variable is discrete or continuous, and it is given by

$$F_X(x) = P(X \leq x) , \quad (50)$$

where the right-hand side represents the probability that the random variable X takes on a value less than or equal to x .

On the other hand, the cumulative distribution function describes the probability that the random variable is no larger than a given value; the probability that the outcome lies in a given interval can be computed by taking the difference between the values of the cumulative distribution function at the endpoints of the interval. The cumulative distribution function is the antiderivative of the probability density function provided that the latter function exists.

The probability of the random variable falling within a particular range of values is given by the integral of this variable's density over that range - that is, it is given by the area under the density function but above the horizontal axis and between the lowest and greatest values of the range. The probability density function is nonnegative everywhere, and its integral over the entire space is equal to one (eq. (55)).

With F_X (the cdf) of X , the pdf is:

$$f_X(x) = \int_{-\infty}^x f_X(u) du , \quad (51)$$

and (if f_X is continuous at x)

$$f_X(x) = \frac{d}{dx} F_X(x) . \quad (52)$$

So to calculate the probability that a continuous r.v. X falls into an interval (a,b) ($[a,b)$, $(a,b]$, $[a,b]$) by the definition of CDF and the fundamental theorem of calculus, one has to integrate the PDF over the appropriate range

$$P(a < X \leq b) = F(b) - F(a) = \int_a^b f(x) dx . \quad (53)$$

Intuitively, one can think of $f_X(x)dx$ as being the probability of X falling within the infinitesimal interval $[x, x + dx]$

$$\text{probability to observe } x \text{ in the interval } [x, x + dx] = f_X(x)dx . \quad (54)$$

$f(x)$ is the density of the distribution near a specific value x . In the relative frequency interpretation, $f_X(x)dx$ gives the fraction of times that X is observed in the interval $[x, x + dx]$ in the limit that the total number of observations is infinitely large. The p.d.f. $f(x)$ is normalized such that the total probability (probability of some outcome) is one,

$$\int_S f(x) dx = 1, \quad (55)$$

where the region of integration S refers to the entire range of x , i.e. to the entire sample space.

In fact, $F(x)$ is usually defined as the probability to obtain an outcome less than or equal to x , and the p.d.f. $f(x)$ is then defined as $\partial F/\partial x$. For the 'well-behaved' distributions (i.e. $F(x)$ everywhere differentiable) typically encountered in data analysis, the two approaches are equivalent. (Note that the units of $f(x)$ are $[\text{units}(X)]^{-1}$, so for example if X is in cm, then $f(x)$ is in cm^{-1} .)

This distinction between parameters (p , later θ or $\boldsymbol{\theta}$) and observables (x or \boldsymbol{x}) is important, because it directly relates to the function expression of the object: a probability density function is unit normalized with respect to its observables, but not with respect to its parameters (eq. (55) can also be written as $\int_S f(p; x) dx = 1$). Observables are measured quantities, while parameters are degrees of freedom in the model.

3.2.1. Quantile

A useful concept related to the cumulative distribution is the so-called **quantile of order α** (or p ; or **α -point**; or p -Quantile $Q(p)$). The quantile x_α (or p) is defined as the value of the random variable x such that $F(x_\alpha) = \alpha$, with $0 < \alpha < 1$. Demonstrative the quantile is a threshold. That is, the quantile is simply the inverse function of the cumulative distribution (eq. (51), figure 23)

$$x_\alpha = F^{-1}(\alpha). \quad (56)$$

With reference to a continuous and strictly monotonic distribution function, for example the cumulative distribution function (eq. (51)) $F_X: R \rightarrow [0, 1]$ of a random variable X , the quantile function Q returns a threshold value x (or x_α) below which random draws from the given c.d.f would fall p percent of the time. In terms of the distribution function F , the quantile function Q returns the value x such that

$$F_X(x) := \Pr(X \leq x) = p. \quad (57)$$

The cdf ($F(x)$) gives the p values as a function of the q values, while the quantile function Q does the opposite, giving the q values as a function of the p values ($Q = F^{-1}$).

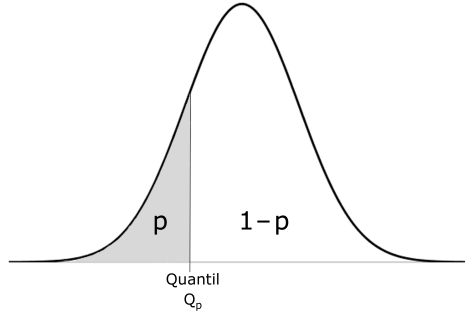


Figure 23: The p -quantile, with $p \in (0, 1)$, is the value of a r.v., which splits its quantity in two sections, left of the p -quantile is p ($= 100 \cdot p\%$); on the right-hand side the remaining $1-p$ ($= 100 \cdot (1 - p)\%$).

3.3. Statistical tests, Hypotheses

A widely used procedure to establish discovery (or exclusion) (or distinguishing events of interest (signal) from other types (background)) in particle physics is based on a frequentist significance test using a likelihood ratio as a test statistic. In addition to parameters of interest (**POI**) such as the rate of the signal process, the signal and background models will contain in general *nuisance parameters* (NUI) whose values are not taken as known *a priori* but rather must be fitted from the data.

The goal of a statistical test is to make a statement about how well the observed data stand in agreement with given predicted probabilities, i.e. a **hypothesis**. The hypothesis under consideration is traditionally called the **null hypothesis**, H_0 , which could specify, for example, a probability density $f(x)$ of a random variable x . If the hypothesis determines $f(x)$ uniquely it is said to be **simple**; if the form of the p.d.f. is defined but not the values of at least one free parameter θ , then $f(x; \theta)$ is called a **composite hypothesis**. In such cases the unknown parameter or parameters are estimated from the data (see sections 3.4 and 3.5.3).

A statement about the validity of H_0 often involves a comparison with some alternative hypotheses, H_1, H_2, \dots . The values could, for example, represent n repeated observations of the same random variable, or a single observation of a n -dimensional variable. In order to investigate the measure of agreement between the observed data and a given hypothesis, one constructs a function of the measured variables called a **test statistic** $t(\mathbf{x})$ (or often also denoted as $\lambda(\mu)$ where μ is the POI of θ - see sec. 3.4 and 3.6).

Often one formulates the statement about the compatibility between the data and the various hypotheses in terms of a decision to accept or reject a given null hypothesis H_0 . This is done by defining a **critical region** for t . Equivalently, one can use its complement, called the **acceptance region**. If the value of t actually observed is in the critical region, one rejects the hypothesis H_0 ; otherwise, H_0 is accepted. The critical region is chosen such that the probability for t to be observed there, under assumption of the hypothesis H_0 , is some value α , called the significance level of the test (compare sec. 3.2.1). There is thus a probability of α to reject H_0 if H_0 is true. This is called an **error**

of the first kind. An **error of the second kind** takes place if the hypothesis H_0 is accepted but the true hypothesis was not H_0 but rather some alternative hypothesis H_i .

From here on (and in the further sections) a vector of data $\mathbf{x} = (x_1, \dots, x_n)$ is considered, from which one would like to construct a one-dimensional test statistic $t(\mathbf{x})$ so as to distinguish between two simple hypotheses H_0 and H_1 . The best test statistic in the sense of maximum power for a given significance level (or selection efficiency) is given by the **likelihood ratio** (compare with eq. (62) and 71)

$$t(\mathbf{x}) = \frac{f(x|H_0)}{f(x|H_1)}. \quad (58)$$

In order to construct this, however, it is necessary to know $f(x|H_0)$ and $f(x|H_1)$.

The (upper) limit calculated in the analysis of this work (more see sec. 3.6) shall not be confused with the statistical significance of an observed signal quantified by means of a p-value or its equivalent Gaussian significance (σ -range). In particle physics one usually converts the p-value into an equivalent significance, Z , defined such that a Gaussian distributed variable found Z standard deviations above its mean has an upper-tail probability equal to p . That is, $Z = \Phi^{-1}(1-p)$, where Φ^{-1} is the quantile (inverse of the cumulative distribution, eq. (51) and (56) and figure 23) of the standard Gaussian (see also sec. 3.2.1). It shall be noted, that some authors define this relation using one-sided and some other a two-sided fluctuation of a Gaussian variable (for example for two-sided: a 5σ significance corresponding to $p = 5.7 \cdot 10^{-7}$).

3.4. Parameter estimation

Considering the situation where one has made n measurements of a random variable x whose p.d.f. $f(x)$ is not known. The central problem of statistics is to infer the properties of $f(x)$ based on the observations $\mathbf{x} = x_1, \dots, x_n$. Specifically, one would like to construct functions of the x_i to estimate the various properties of the p.d.f. $f(x)$. Often one has a hypothesis for the p.d.f. $f(x; \theta)$ which depends on an unknown parameter θ (or parameters $\boldsymbol{\theta} = (\theta_1, \dots, \theta_m)$, containing the POI and the NUI). The goal is then to construct a function of the observed x_i to estimate the parameters.

A function of the observed measurements x_1, \dots, x_n which contains no unknown parameters is called a **statistic**. In particular, a statistic used to estimate some property of a p.d.f. (e.g. its mean, variance or other parameters) is called an **estimator**. The estimator for a quantity θ is usually written with a hat, $\hat{\theta}$, to distinguish it from the true value θ whose exact value is (and may forever remain) unknown.

If $\hat{\theta}$ converges to θ in the limit of large n , the estimator is said to be **consistent**. Here convergence is meant in the sense of probability, i.e. for any $\varepsilon > 0$, one has

$$\lim_{n \rightarrow \infty} P(|\hat{\theta} - \theta| > \varepsilon) = 0. \quad (59)$$

Consistency is usually a minimum requirement for a useful estimator.

The procedure of estimating a parameter's value given the data \mathbf{x} is called **parameter fitting** (more in sec. 3.5.3).

Since an estimator $\hat{\theta}(x_1, \dots, x_n)$ is a function of the measured values, it is itself a random variable.

When observing a signal, one may see evidence for a special type of signal event, the number n_s of which can be treated as a Poisson variable with mean ν_s . In addition to the signal events, however, one will find in general a certain number of background events n_b . Suppose this can also be treated as a Poisson variable with mean ν_b , which will be assumed for the moment to be known without error. The total number of events found, $n = n_s + n_b$, is therefore a Poisson variable with mean $\nu = \nu_s + \nu_b$. The probability to observe n events is thus

$$f(n; \nu_s, \nu_b) = \frac{(\nu_s + \nu_b)^n}{n!} e^{-(\nu_s + \nu_b)}. \quad (60)$$

More on this see section 3.5.2.

The next task is to give some measure of the statistical uncertainty of the estimates. If the entire experiment is repeated a large number of times (with n measurements each time) each experiment would give different estimated values for the parameters. One way of summarizing how widely spread they will be is with the *variance* (or standard deviation) of the estimator. Often the result of a measurement is given as the estimated value of a parameter ($\hat{\theta}$) plus or minus (\pm) one standard deviation, or with asymmetric error (more see sec. 3.5.3). In graphs the error is often displayed as error bar.

The statistical errors (i.e. the standard deviations) are expressed via the inverse of the covariance matrix V^{-1} .

In the case of a sufficiently large data sample, one can estimate V^{-1} by evaluating the second derivative with the measured data and the ML (next sec.) estimates $\hat{\theta}$. This is the usual method for estimating the covariance matrix when the likelihood function is maximized numerically. For example, the routines MIGRAD and HESSE in the program **MINUIT** (see sec. 3.5.3) [50] determine numerically the matrix of second derivatives of $\log L$ using finite differences, evaluate it at the ML estimates, and invert to find the covariance matrix. In cases of doubt one should check the results with a Monte Carlo study.

It turns out in many applications to be too difficult to compute the variances analytically, and a Monte Carlo study usually involves a significant amount of work. In such cases one typically uses the *Rao-Cramer-Frechet (RCF) inequality*, also called the information inequality, which gives a lower bound on an estimator's variance. (This inequality applies to any estimator, not only those constructed from the ML principle.)

3.5. The method of maximum likelihood

Considering a random variable x distributed according to a p.d.f. $f(x; \theta)$. Supposing the functional form of $f(x; \theta)$ is known, but the value of at least one parameter θ (or parameters $\boldsymbol{\theta} = (\theta_1, \dots, \theta_m)$) are not known. The method of **maximum likelihood (ML)** is a technique for estimating the values of the parameters given a finite sample of data \boldsymbol{x} .

Under the assumption of the hypothesis $f(x; \theta)$, including the value of θ , the probability for the first measurement to be in the interval $[x_1, x_1 + dx_1]$ is $f(x; \theta)dx_1$. Since the measurements are all assumed to be independent, the probability to have the first one in $[x_1, x_1 + dx_1]$, the second in $[x_2, x_2 + dx_2]$, and so forth is given by

$$\text{probability that } x_i \text{ in } [x_i, x_i + dx_i] \text{ for all } i = \prod_{i=1}^n f(x_i; \theta)dx_i . \quad (61)$$

If the hypothesized p.d.f. and parameter values are correct, one expects a high probability for the data that were actually measured. Conversely, a parameter value far away from the true value should yield a low probability for the measurements obtained. Since the dx_i do not depend on the parameters, the same reasoning also applies to the following function L

$$L(\theta) = \prod_{i=1}^n f(x_i; \theta) , \quad (62)$$

called the **likelihood function**. (Note that this is just the joint p.d.f. for the x_i , although it is treated here as a function of the parameter θ . The x_i , on the other hand, are treated as fixed (i.e. the experiment is over).) The likelihood function is the probability of observing the data as a function of θ . In informal contexts, "likelihood" is often used as a synonym for "probability." In statistics, a distinction is made depending on the roles of outcomes vs. parameters. *Probability* is used before data are available to describe possible future outcomes given a fixed value for the parameter (or parameter vector). *Likelihood* is used after data are available to describe a function of a parameter (or parameter vector) for a given outcome.

Sometimes the density function for the value x of \mathbf{x} for the parameter value θ is written as $f(x|\theta)$, what should not be confused with $L(\theta|x)$ which should not be considered a conditional probability density.

With this motivation one defines the maximum likelihood (ML) estimators for the parameters to be those which *maximize* the likelihood function. As long as the likelihood function is a differentiable function of the parameters $\theta_1, \dots, \theta_m$, and the maximum is not at the boundary of the parameter range, the estimators are given by the solutions to the equations

$$\frac{\partial L}{\partial \theta_i} = 0 , \quad i = 1, \dots, m . \quad (63)$$

If more than one local maximum exists, the highest one is taken. As with other types of estimators, they are usually written with hats, $\hat{\theta} = (\hat{\theta}_1, \dots, \hat{\theta}_m)$, to distinguish them from the true parameters θ_i whose exact values remain unknown.

The motivation for the ML principle presented does not necessarily guarantee any optimal properties for the resulting estimators. The ML method turns out to have many advantages, among them ease of use and the fact that no binning is necessary.

3.5.1. The log-likelihood function

Rather than using the likelihood function as defined in equation (62) it is usually more convenient to use its logarithm. Since the logarithm is a monotonically increasing function, the parameter value which maximizes L will also maximize $\log L$. The logarithm has the advantage that the product in L is converted into a sum, and exponentials in f are converted into simple factors (very useful for example when using the Poisson distribution which contains two terms that can easily overflow on computers). The (natural logarithm of the likelihood function (62), called) **log-likelihood function** is thus

$$\log L(\theta) = \sum_{i=1}^n \log f(x_i; \theta) . \quad (64)$$

As mentioned above, by numerically maximizing the log-likelihood function, one obtains values for θ where the statistical errors are the square roots of the variance. These have been estimated by computing (numerically) the matrix of second derivatives of the log-likelihood function with respect to the parameters, and then inverting to obtain the covariance matrix.

In the large sample limit, the log-likelihood function takes on the form

$$\log L(\hat{\theta}) = \log L_{max} \quad (65)$$

3.5.2. Extended maximum likelihood

As explained in the context of equation (60) it is often the case that the number of observations n in the sample is itself a Poisson random variable with a mean value ν . The result of the experiment can be defined as the number n and the n values x_1, \dots, x_n . The likelihood function is then the product of the Poisson probability to find n and the usual likelihood function for the n values of \mathbf{x}

$$L(\nu, \theta) = \frac{\nu^n}{n!} e^{-\nu} \prod_{i=1}^n f(x_i; \theta) = \frac{e^{-\nu}}{n!} \prod_{i=1}^n \nu f(x_i; \theta) . \quad (66)$$

This is called the **extended likelihood function**. It is really the usual likelihood function, however, only now with the sample size n defined to be part of the result of the experiment. One can distinguish between two situations of interest, depending on whether the Poisson parameter ν is given as a function of θ or is treated as an independent parameter (the case in this work).

The situation of interest is where there is no functional relation between ν and θ . Taking the logarithm of eq. (66) and setting the derivative with respect to ν equal to zero gives the estimator

$$\hat{\nu} = n , \quad (67)$$

as one would expect. By setting the derivative of $\log L(\nu, \theta)$ with respect to the θ_i equal to zero, one obtains the same estimators $\hat{\theta}_i$ as in the usual ML case. So the situation is

essentially the same as before, only now a quantity which depends on both n and $\hat{\theta}$ will contain an additional source of statistical fluctuation, since n is regarded as a random variable.

In some problems of this type, however, it can still be helpful to use the extended likelihood function. Often the p.d.f. of a variable x is the superposition of several components,

$$f(x; \boldsymbol{\theta}) = \sum_{i=1}^m \vartheta_i f_i(x; \boldsymbol{\xi}_i), \quad (68)$$

whereat $\boldsymbol{\theta}$ contains the parameters $\boldsymbol{\vartheta} = (\vartheta_1, \dots, \vartheta_m)$ and $\boldsymbol{\xi}_i$ and the goal is to estimate the ϑ_i representing the relative contributions of each component. Suppose that the p.d.f.s $f_i(x)$ are all known (as supposed for the analysis for this work). Here the parameters ϑ_i are not all independent, but rather are constrained to sum to unity. The addition rule above is involved with finding the probability of i or $i+1$. The emphasis here is on "or", i.e. when one or the other will occur. Each probability rule is related to some kind of events. The addition rule is involved with disjoint or if one will occur than the other.

In the usual case without the extended likelihood function, this can be implemented by replacing one of the coefficients, e.g. ϑ_m , by $1 - \sum_{i=1}^{m-1} \vartheta_i$, so that the p.d.f. contains only $m-1$ parameters. One can then construct the likelihood function and from this find estimators for the ϑ_i .

The problem can be treated in an equivalent but more symmetric way using the extended likelihood function (66). Taking the logarithm and dropping terms not depending on the parameters gives

$$\log L(\nu, \boldsymbol{\vartheta}, \boldsymbol{\theta}) = -\nu + \sum_{i=1}^n \log \left(\sum_{j=1}^m \nu \vartheta_j f_j(x_i; \boldsymbol{\theta}) \right). \quad (69)$$

By defining $\mu_i = \vartheta_i \nu$ as the expected number of events of type i , the log-likelihood function can be written as a function of the m parameters $\boldsymbol{\mu} = (\mu_1, \dots, \mu_m)$

$$\log L(\boldsymbol{\mu}) = -\sum_{j=1}^m \mu_j + \sum_{i=1}^n \log \left(\sum_{j=1}^m \mu_j f_j(x_i) \right). \quad (70)$$

The parameters $\boldsymbol{\mu}$ are no longer subject to a constraint, as were the components of $\boldsymbol{\vartheta}$. The total number of events n is viewed as a sum of independent Poisson variables with means μ_i . The estimators $\hat{\mu}_i$ give directly the estimated mean numbers of events of the different types. This is of course equivalent to using the ML estimators $\hat{\vartheta}_i$ for the fractions along with the estimator $\hat{\nu} = n$ for the single Poisson parameter ν . Now, however, all of the parameters are treated symmetrically. Furthermore, the parameters μ_i are often more closely related to the desired final result.

3.5.3. Fitting a model to data

For (numerical) convenience and because it is more robust for low statistics fits (and it can also be performed on unbinned data) the **negative** log of the likelihood (**NLL**) is often used, and in comparison to estimating parameters by maximizing the (log) Likelihood, it is equivalently *minimizing* $-\log(L)$. The standard tool in High Energy Physics to perform the minimization and error analysis since decades is **MINUIT**, and also RooFit (explained in the next chapter) delegates the minimization task to the ROOT implementation of MINUIT in the class TMinuit. RooFit is therefore more of a data modelling package rather than a fitting package.

After creating the $-\log(L)$ (NLL) from the pdf and the given dataset it is given to MINUIT, which minimizes it (with respect to the floating parameters) by computing the best-fit parameter values and estimate the errors on the parameters of the pdf, including correlations between the parameters. (As mentioned before the variance is estimated from 2nd derivative of $-\log(L)$ at minimum (Rao-Cramer-Frechet inequality).)

The errors based on the MINUIT error matrix take account of all the parameter correlations, but not the non-linearities. After the error matrix has been calculated the parameter errors printed by MINUIT are the square roots of the diagonal elements of the matrix. MINUIT was written by CERN staff physicist Fred James in the 1970s and in the early 2000s he started a project for a new MINUIT, which is an optional package (*minuit2*) in the ROOT release. [50]

In the following a very short description of the functionality and some of the most important routines of MINUIT is given.

- MIGRAD

This routine performs a local function minimization using a modified version of the Davidson-Fletcher-Powell switching method. It finds the function minimum via calculating the function gradient, then follow to a (local) minimum, recalculate the gradient, and iterate until the minimum is found. The number of function calls required depends greatly on the number of floating parameters, the distance from the function minimum and the shape of function. For all but the most trivial scenarios it is not possible to automatically find reasonable starting values of parameters, so it is necessary to supply "reasonable" starting values for the parameters, because there may exist multiple (local) minima in the likelihood. Also one may need to supply a "reasonable" initial step size in parameters.

- HESSE

The HESSE routine calculates the full second-derivative matrix of the user function using a finite difference method. This is often used to improve upon the result obtained by MIGRAD. It also gives symmetric error. It is valid in assumption that the likelihood is locally parabolic and it requires roughly N^2 likelihood evaluations (with N = number of floating parameters).

- MINOS

It was (probably) the first program to calculate parameter errors taking into account both parameter correlations and non-linearities. The MINOS error intervals are in general **asymmetric**, and may be expensive to calculate especially if there are a lot of free parameters and if the problem is very non-linear. Its error analysis can result in different errors than obtained using MIGRAD or HESSE methods. MINOS can only operate after a good minimum has already been found, and the error matrix has been calculated. So MINOS normally follows MIGRAD (and HESSE).

Sometimes fits do not converge because, e.g. MIGRAD is unable to find a minimum, or HESSE finds negative second derivatives (which would imply negative errors). The most common problems are usually numerical precision and stability problems, but the underlying cause of fit stability problems is usually by highly correlated parameters in the fit. To put things right one can try to fix a parameter; if parameters are highly correlated, fixing one to a reasonable value can help improve the convergence property of a fit.

Furthermore, if a fitted parameter value is close to a boundary, errors will become asymmetric (and possibly incorrect). For example: a fraction parameter is only defined in the range $[0,1]$. MINUIT maps finite range parameter to an internal infinite range using an $\arcsin(x)$ transformation. So one has to be careful with bounds. If boundaries are imposed to avoid a region of instability, one should look into other parametrizations that naturally avoid that region. And if boundaries are imposed to avoid "unphysical", but statistically valid results, one should consider not imposing the limit and dealing with the "unphysical" interpretation in a later stage. Also a special care should be taken when fitting small data samples.

3.6. Wilks' Theorem

This theorem is based on the ratio of likelihoods. As mentioned before (sec. 3.3, and eq. (58)) a **likelihood ratio test** is in general a statistical test used to compare the goodness of fit of two models, one of which (the null model, H_0) is a special case of the other (the alternative model, H_1). The test is based on the likelihood ratio (eq. 58 and (71)), which expresses how many times more likely the data are under one model than the other. It is often denoted by λ (or $\lambda(\theta_i)$) and is defined as

$$\lambda = \frac{L(H_0)}{L(H_1)}, \quad (71)$$

where the null and alternative hypotheses for convenience are written in terms of fixed values of a notional parameter θ : $H_0 : \theta = \theta_0$, $H_1 : \theta = \theta_1$. The likelihood ratio is small if the alternative model is better than the null model and the likelihood ratio test rejects the null hypothesis if the value of this statistic is too small. How small is too small depends on the significance level of the test, i.e., on what probability of Type I

error is considered tolerable. Low values of the likelihood ratio mean that the observed result was less likely to occur under the null hypothesis as compared to the alternative. High values of the statistic mean that the observed outcome was nearly as likely to occur under the null hypothesis as the alternative, and the null hypothesis cannot be rejected. (A likelihood interval can be used without claiming any particular coverage probability; as such, it differs from confidence intervals.)

This likelihood ratio, or equivalently its logarithm, can then be used to compute a p-value, or compared to a critical value to decide whether to reject the null model in favour of the alternative model. When the logarithm of the likelihood ratio is used, the statistic is known as a log-likelihood ratio statistic, and the probability distribution of this test statistic, assuming that the null model is true, can be approximated using **Wilks' theorem**.

This is a convenient result, found by Samuel S. Wilks, stating that as the sample size n approaches ∞ , the test statistic $-2\log(\lambda)$ (eq. (72)) for a nested model will be asymptotically chi-squared distributed (χ^2) with degrees of freedom (**df**) equal to the difference in dimensionality of θ_0 and θ_1 , when H_0 holds true. [51] This means that for a great variety of hypotheses, a practitioner can compute the likelihood ratio λ for the data and compare $-2\log(\lambda)$ to the χ^2 value corresponding to a desired statistical significance as an approximate statistical test.

That is, in short, each of the two competing models, the null model and the alternative model, is separately fitted to the data and the log-likelihood recorded. The test statistic (often denoted by D) is twice the log of the likelihoods ratio, i.e., it is twice the difference in the log-likelihoods

$$\begin{aligned} D &= -2\ln(\lambda) = -2\ln\left(\frac{L(H_0)}{L(H_1)}\right) = 2\ln\left(\frac{L(H_1)}{L(H_0)}\right) \\ &= 2\left[\ln(L(H_1)) - \ln(L(H_0))\right] \end{aligned} \tag{72}$$

The alternative model (with more parameters) will always fit at least as well - i.e., have the same or greater log-likelihood - than the model with fewer parameters (here null), resulting in $0 \leq \lambda \leq 1$ (eq. (71)). Whether the fit is significantly better and should thus be preferred is determined by deriving the probability or p-value of the difference D . Where the null hypothesis represents a special case of the alternative hypothesis, the probability distribution of the test statistic is approximately a χ^2 distribution with degrees of freedom equal to $df_{\text{alt}} - df_{\text{null}}$ ([52]), respectively the number of free parameters of models alternative and null.

The results of Wilks generalize to more than one parameter of interest. If the POI can be explicitly identified with a subset of the parameters $\theta_r = (\theta_1, \dots, \theta_r)$, then the distribution of $-2\ln\lambda(\theta_r)$ follows a noncentral χ^2 distribution for r -degrees of freedom.

Wilks' theorem assumes that the true but unknown values of the estimated parameters are in the interior of the parameter space, but this can be violated for some special models.

4. Analysis (Software), discussion and results

With the level of knowledge on likelihoods and p.d.f.s from chapter 3, the model to apply must be clearly defined (and normalized over the range of interest of the observable) in order to fit the model to the data, what is explained in 4.1.

After explaining how the data were handled and analysed and the model was fitted in section 4.2, the calculation of the limit and also the limit on the dark photon mixing κ (eq. (47)) is explained in section 4.3. Some further technical details are discussed in section 4.4 as well as a flowchart of the algorithm is given.

To make a statement about the calculated result and its quality, the used algorithm had to be tested, what was done with Monte Carlo simulations (pseudo data), explained in 4.5.

To complete this chapter all the results available in figures are presented for clarity in section 4.6.

4.1. The model

To define the likelihood according to (62) or rather (66) and (68) in order to use it for the fit, first the pdf has to be defined.

The limit for the Lise data should be given over an specific energy range, what is for dark photons in relation with m_V in [keV/c²]. So the observable, the (continuous r.v.) x from chapter 3, now belongs to the **energy**, but for simplicity is still denoted as x in this chapter. The first step is to choose the interesting range of the data (energy), because this determines amongst other things which and how many components for the model are necessary. The upper border was chosen to be 40 keV (" x_{up} " in the following), because above there are strong astrophysical limits (but already at above ≈ 1 keV other experiments (for example XENON100 and XENON1T) give limits better to some order of magnitude). The border on the low side was given by the threshold of the detector module (see sec. 2.1.1) and was 0.3 keV (" x_{low} ").

In the resulting range the model was chosen to consist of five types of events ($f_i(x)$, with $i = 1, 2, 3, 4, 5$), i.e. a signal and four background components. What is exactly meant by "signal" is explained later (sec. 4.3). The signal and three components of the background are represented with **Gauss**-peaks (normal distribution), in the following denoted as f_G , and the remaining background component is a **constant** (uniform distribution) f_C .

The probability density of the normal distribution is:

$$f_G = f(x | \mu, \sigma) = \frac{1}{\sqrt{2\pi}\sigma} e^{-\frac{(x-\mu)^2}{2\sigma^2}}, \quad (73)$$

where μ is the mean (here the position) or expectation of the distribution (and also its median and mode) and σ is its standard deviation (and σ^2 the variance) and are for clarity later denoted as $\boldsymbol{\xi} = (\mu, \sigma)$ and $f(x | \mu, \sigma) = f(x | \boldsymbol{\xi})$. f_G as represented in (73) is normalized to unit area for $x_{-\infty} < x < x_{+\infty}$.

The probability density function of the continuous uniform distribution (often abbreviated $U(x_{\text{low}}, x_{\text{up}})$) is:

$$f_C = f(x) = \begin{cases} \frac{1}{x_{\text{up}} - x_{\text{low}}} & \text{for } x_{\text{low}} \leq x \leq x_{\text{up}}, \\ 0 & \text{for } x < x_{\text{low}} \text{ or } x > x_{\text{up}}. \end{cases} \quad (74)$$

With this form f_C is normalized to 1 in the relevant range.

To model the shape of the data also the form of the **efficiency** of the detector module has to be taken into account, affecting all five components multiplicative in the pdf. Multiplicative in the sense of "and" in the meaning of probability. (For CRESST-II a detailed description of the data acquisition, readout, and the procedures for controlling detector stability, as well as reconstructing the deposited energy from the measured pulses can be found in [53] and [54].) The model for the efficiency ($\varepsilon(x) = \varepsilon$) is

$$\varepsilon(x \mid st, amp, \tau) = \begin{cases} st \cdot \left(1 - amp \cdot e^{-\frac{x}{\tau}}\right) & \text{for } x \geq x_{\text{low}}, \\ 0 & \text{for } x < x_{\text{low}} \end{cases} \quad (75)$$

and was separately fitted to determine its three parameters st , amp and τ . This can be seen in figure 24.

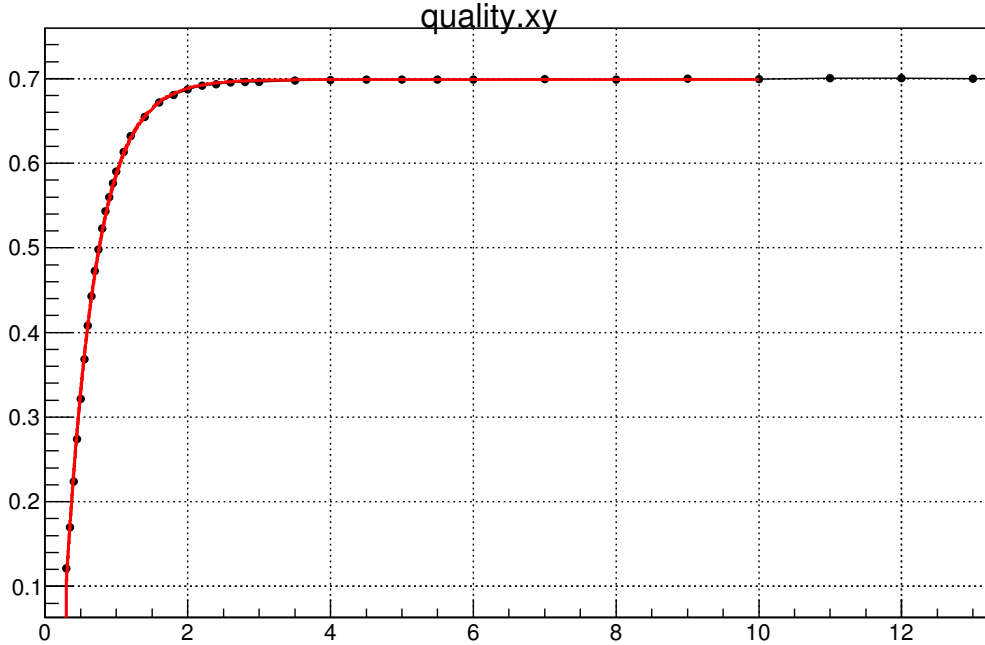


Figure 24: Shape and fit (red) (of (75)) of the efficiency of the detector module Lise, with energy on the x-axis in [keV] and with the threshold of $x_{\text{low}} = 0.3$ keV.

In comparison with (73) and (74), which are normalized per definition to unit area within a fixed range ($x_{\text{low}} < x < x_{\text{up}}$, or $x_{-\infty} < x < x_{+\infty}$), the normalization of each

component of the pdf (eq. (55)) has to be performed extra, because of the multiplication with the efficiency $\varepsilon(x)$. With the equations (73), (74) and (75) the p.d.f. of the model can be represented as

$$f(x; \boldsymbol{\theta}) = \sum_{i=1}^5 \vartheta_i \frac{\varepsilon(x) f_i(x; \boldsymbol{\xi}_i)}{\int_{x_{\text{low}}}^{x_{\text{up}}} \varepsilon(x) f_i(x; \boldsymbol{\xi}_i) dx} = \varepsilon(x) \sum_{i=1}^5 \vartheta_i \frac{f_i(x; \boldsymbol{\xi}_i)}{\int_{x_{\text{low}}}^{x_{\text{up}}} \varepsilon(x) f_i(x; \boldsymbol{\xi}_i) dx}, \quad (76)$$

whereat the ϑ_i are not independent but rather have to sum to unity, the (vector) $\boldsymbol{\theta}$ containing all the parameters to be fitted: $\boldsymbol{\vartheta} = (\vartheta_1, \dots, \vartheta_5)$ and $\boldsymbol{\xi}_i$, which are the parameters of each Gaussian model component ($= 0$ for f_C). The normalization (of each component) is taken into account in the denominator of eq. (76).

The integrals for normalization of the two different types of components are

$$\begin{aligned} \int_{x_{\text{low}}}^{x_{\text{up}}} \varepsilon(x) \cdot f_C(x) dx &= \int_{x_{\text{low}}}^{x_{\text{up}}} st \cdot \left(1 - amp \cdot e^{-\frac{x}{\tau}}\right) \cdot Const dx = \\ &= st \cdot Const \cdot \left[\int_{x_{\text{low}}}^{x_{\text{up}}} dx - amp \int_{x_{\text{low}}}^{x_{\text{up}}} e^{-\frac{x}{\tau}} dx \right] = \\ &= st \cdot \underbrace{Const}_{=\frac{1}{x_{\text{up}} - x_{\text{low}}}} \cdot \left[x_{\text{up}} - x_{\text{low}} + amp \cdot \tau \left(e^{-\frac{x_{\text{up}}}{\tau}} - e^{-\frac{x_{\text{low}}}{\tau}} \right) \right] = \\ &= st \cdot \left[1 + \frac{amp \cdot \tau}{x_{\text{up}} - x_{\text{low}}} \left(e^{-\frac{x_{\text{up}}}{\tau}} - e^{-\frac{x_{\text{low}}}{\tau}} \right) \right] \end{aligned} \quad (77)$$

for the constant component, and

$$\begin{aligned} \int_{x_{\text{low}}}^{x_{\text{up}}} \varepsilon(x) \cdot f_G(x) dx &= \int_{x_{\text{low}}}^{x_{\text{up}}} st \cdot \left(1 - amp \cdot e^{-\frac{x}{\tau}}\right) \cdot \frac{1}{\sqrt{2\pi}\sigma} e^{-\frac{(x-\mu)^2}{2\sigma^2}} dx = \\ &= \frac{st}{\sqrt{2\pi}\sigma} \left[\int_{x_{\text{low}}}^{x_{\text{up}}} e^{-\frac{(x-\mu)^2}{2\sigma^2}} dx - amp \int_{x_{\text{low}}}^{x_{\text{up}}} e^{-\frac{x}{\tau}} e^{-\frac{(x-\mu)^2}{2\sigma^2}} dx \right] = \\ &= \frac{st}{2} \left[\operatorname{erf} \left(\frac{\mu - x_{\text{low}}}{\sqrt{2}\sigma} \right) - \operatorname{erf} \left(\frac{\mu - x_{\text{up}}}{\sqrt{2}\sigma} \right) - \right. \\ &\quad \left. - amp e^{\frac{\sigma^2 - 2\mu\tau}{2\tau^2}} \left(\operatorname{erf} \left(\frac{x_{\text{up}}\tau - \mu\tau + \sigma^2}{\sqrt{2}\tau\sigma} \right) - \operatorname{erf} \left(\frac{x_{\text{low}}\tau - \mu\tau + \sigma^2}{\sqrt{2}\tau\sigma} \right) \right) \right] \end{aligned} \quad (78)$$

for the Gaussian components, where erf is the Gauss error function.

4.2. Likelihood fit

The model (76) defined in section 4.1 was fitted to data via an unbinned likelihood fit (explained in the previous chapter), with the data treated as $\mathbf{x} = (x_1, \dots, x_n)$, with n number of events. Because the number of events ($n = n_{sig} + n_{bkg}$, with $n_{bkg} = n_{bkg,1} + n_{bkg,2} + n_{bkg,3} + n_{bkg,4}$) per component are also parameters to be fitted, the *extended* likelihood (section 3.5.2; eq. (66)) had to be used. Each component (n_i) is distributed according to a Poisson distribution and therefore their sum (n) is also Poisson distributed. With the pdf (76) the extended likelihood can be written as

$$L(\mathbf{x}|\nu, \boldsymbol{\theta}) = \frac{\nu^n}{n!} e^{-\nu} \prod_{i=1}^n f(x_i; \boldsymbol{\theta}) . \quad (79)$$

Inserting (76) gives

$$L(\mathbf{x}|\nu, \boldsymbol{\theta}) = \frac{\nu^n}{n!} e^{-\nu} \prod_{i=1}^n \varepsilon(x_i) \sum_{j=1}^5 \vartheta_j \frac{f_j(x_i; \boldsymbol{\xi}_j)}{\int_{x_{low}}^{x_{up}} \varepsilon(x) f_j(x; \boldsymbol{\xi}_j) dx} , \quad (80)$$

with the conditions

$$\sum_k \vartheta_k = 1 , \quad (81)$$

and accordingly

$$\vartheta_k = \frac{s_k}{\nu} \quad \text{with} \quad \sum_k s_k = \nu . \quad (82)$$

The three Gaussian components of the background were characterised to belong to specific iron (^{55}Fe) and copper (Cu fluorescence) lines ([45]), and can be seen in the energy spectrum (after cuts - explained in [44] and [45]) in figure 28 and 29. The iron background peaks resulted from a accidental illumination of the detector module Lise with an iron source (installed to calibrate the light detector of a close-by detector module) and contributed the two peaks Fe- K_α at ≈ 6.0 keV and Fe- K_β at ≈ 6.6 keV in the spectrum. The third one originates from the shielding of the detector module with its peak in the data at: Cu: ≈ 8.1 keV (copper K_α escape line). This three positions of the peaks are the μ in eq. (73). For the fit the allowed range of values of the μ_i had to be restricted, because otherwise the routines (Minuit2, Migrad) could not find the correct minimum because of possible overlaps or rather distinguishing between the peaks. Further restrictions were implemented on the n_i , the number of events of each component, to be priori positive (or zero). Also the position (μ in eq. (73)) of the signal peak had to be fixed, but this is explained in the following section. (In the energy spectrum there is a peak at 2.7 keV, which probably is due to cosmogenic activation of tungsten, but is controversial so far, because of missing peaks according to tungsten

at higher energies an was therefore not included in the background model.) In the selected, or rather in the energy range from 1.0 to 40 keV an average background level of 13 counts/(keV kg day) was determined. And if the contribution of the ^{55}Fe -source is excluded a value of 8.5 counts/(keV kg day) is obtained.

4.3. Limit

To calculate the 90% upper limit for the data measured with the detector module Lise of CRESST-II Phase 2 (in the defined energy range), Wilks' theorem (eq. (72)) was used:

$$t(\eta) = -2 \log \lambda(\eta) = -2 \log \frac{L(\eta, \hat{\theta})}{L(\hat{\eta}, \hat{\theta})} = 2 \left(\log(L(\hat{\eta}, \hat{\theta})) - \log(L(\eta, \hat{\theta})) \right) \quad (83)$$

with η (later denoted " $n_{sig,UL}$ ") the parameter of interest (POI). $\log(L(\hat{\eta}, \hat{\theta}))$ is the best fit result, received from "Minuit2" via minimizing the NLL (see section 3.5.3), with p free parameters. $\log(L(\eta, \hat{\theta}))$ is the best fit result of the same model, but with $q = p - 1$ free parameters, because of a fixed value for η .

According to Wilks' theorem (section 3.6) $t(\eta)$ shall be χ^2 distributed ($f(t_\eta|\eta) = \chi_k^2(t_\eta)$), with $k = p - q = 1$ degrees of freedom, because the model with less free parameters is a special case of the other one. The "90% upper limit" is the value of $n_{sig,UL}$ for which the c.d.f. of $\chi_1^2(t_\eta)$ is 0.9 ($F(t_\eta) = 0.9 = \alpha$; as explained in sec. 3.2.1). As can be obtained from standard tables or from computer routines, the 90%-Quantile of a χ^2 distribution with one dof is $t_{\eta,90} = 2.705543$.

The procedure is similar to a "peak search". So for every single position (energy value) at which the limit should be calculated the "signal" position (μ of its Gauss peak (73)) had to be fixed. For the signal peak also its parameter σ was fixed to $\sigma_{sig} = 0.062$ keV and resulted in the *resolution* of the detector (energy resolution at zero energy - baseline noise). The limit was chosen to be calculated at 200 positions (energy values) in the range 0.3 keV to ≈ 5 keV and ≈ 9 keV to 40 keV. The range in between (≈ 5 keV to ≈ 9 keV) was spared because of the three mentioned background peaks lying in this range.

So to find the value of $n_{sig,UL}$ for one position a root-finder ("BrentRootFinder") had been used, which had to solve the previous equation (83) rewritten to

$$\underbrace{\log(L(\eta, \hat{\theta}))}_{\text{find}\eta} + \frac{\overbrace{t_{\eta,90}}^{\chi^2\text{-Quantile}}}{2} - \underbrace{\log(L(\hat{\eta}, \hat{\theta}))}_{\substack{\text{best fit} \\ p \text{ free parameters}}} = 0 \quad (84)$$

Here again for the root-finder good initial values were necessary.

To obtain the correct values for the limit, the **exposure** (Expo = mass \cdot time) had

to be taken into account, which was for the Lise module: $Expo = 51.128377$ kg days. Also the effect of the detector efficiency (eq. (75)) had to be corrected, what was done by calculating:

$$\frac{n_{sig,UL}}{X} = \frac{\int_{x_{low}}^{x_{up}} \varepsilon(x) f_G(x) dx}{\underbrace{\int_{x_{low}}^{x_{up}} f_G(x) dx}_{=1}} , \quad (85)$$

and

$$\Rightarrow X = \frac{n_{sig,UL}}{\int_{x_{low}}^{x_{up}} \varepsilon(x) f_G(x) dx} . \quad (86)$$

So the final frequentist 90% upper limit for the Lise data (can be seen in figure 30) was calculated via

$$\text{limit} = \frac{n_{sig,UL}}{Expo \cdot \int_{x_{low}}^{x_{up}} \varepsilon(x) f_G(x) dx} , \quad (87)$$

with $n_{sig,UL}$ the values from the root-finder.

A flow-chart of the algorithm explained in words in this section can be seen in figure 25 (and an explanation of the applied cuts is given at the end of section 4.4).

The limit converted with eq. (47) to the dark photon mixing κ (or $\kappa(m_\nu)$) can be seen in figure 31 (compared with a limit calculated with a Bayesian approach), or additional with astrophysical constraints explained in section 1.8.5 as well as limits from other experiments (XENON) can be seen in figure 32. **It can be seen, that the result from the frequentist approach is in good agreement with the one from a Bayesian approach.** For eq. (47) an isothermal dark matter halo with (a galactic escape velocity of 544 km/s, an asymptotic velocity of 220 km/s and) a dark matter density of $0.3 \text{ GeV}/\text{cm}^{-3}$ was assumed. The annual modulation effect is neglected.

For the photon cross section σ_γ in eq. (47) data from NIST ([55]) and from VUO (Virtual Unified Office, [56]) were combined. Because the data from NIST reach down to 1 keV, but the threshold of Lise is 0.3 keV, data from VUO were added and the final cross section for CaWO_4 can be seen in figure 33. In figure 32 the cyan graph for the Bayesian limit was calculated via a linear interpolation of the data from NIST to energies below 1 keV. In comparison to this, the pink graph was calculated with the combined cross section (NIST and VUO) and yielded a better result.

(For figure 32, a *Flat prior* in the context of Bayesian inference: Simply put, a *flat*/non-informative prior is used when one has little/no knowledge about the data and hence

it has the least effect on outcomes of the analysis (i.e. posterior inference). Roughly speaking, a prior distribution is noninformative if the prior is "flat" relative to the likelihood function. Thus, a prior is noninformative if it has minimal impact on the posterior distribution. Other names for the noninformative prior are vague, diffuse, and flat prior. Many statisticians favour noninformative priors because they appear to be more objective. However, it is unrealistic to expect that noninformative priors represent total ignorance about the parameter of interest.)

4.4. Algorithm

The algorithm was written in C++ and processed via ROOT. ROOT is a modular scientific software framework which provides functionalities to deal with big data processing, statistical analysis, visualisation and storage. It is an object-oriented program and library developed by CERN. It was originally designed for particle physics data analysis and is mainly written in C++ (but integrated with other languages such as Python and R).

At first some attempts were done using RooFit/RooStats. RooFit is a complete toolkit for fitting and data analysis modelling. The RooFit library provides a toolkit for modelling the expected distribution of events in a physics analysis, whereat models can be used to perform unbinned maximum likelihood fits, produce plots, and generate "toy Monte Carlo" samples for various studies. The software was primarily designed as a particle physics data analysis tool, but its general nature and open architecture make it useful for other types of data analysis also. It introduces a granular structure in its mapping of mathematical data model components to C++ objects.

RooStats is a joint project between the LHC experiments and the ROOT team and is a project to create statistical tools built on top of RooFit and distributed in ROOT. The idea was to provide the major statistical techniques as a set of C++ classes with coherent interfaces, so that can be used on arbitrary models and datasets in a common way.

RooFit/RooStats would have had the great advantage of a broad flexibility to test different models and a few analysis techniques. But after several attempts with the root build-in toolkits, problems with the special model of this work (and more complex background models) had been ascertained due to the dependence of the efficiency (75) and sadly could not be eliminated because for a lack of documentation.

The data for this work were given in the form of ROOT-files, with several trees, whereof one were the energy events measured with the Lise detector (see sec. 2.1.1).

At the beginning of the algorithm two cuts (see fig. 25) were applied on the energy events. One necessary to select the range (0.3 to 40 keV) and the other cut depended on the light yield (which was also given in a tree). In the latter cut, it was checked, if the light yield of an event lies inside the central 90% two-sided interval around a mean value which also decreases at the lower energies.

A "two dimensional" fit, incorporating the light yield (LY), would have been of no advantage to the limit for κ (had been ascertained via a previous Bayesian approach), but rather bring new challenges and problems to the fit (additional $L(\text{LY}|\theta')$) and also to the root finder. A detailed explanation on the relation (selection process, cuts, etc.) between the acceptance region in the light yield - energy plane and the energy spectrum given in figure 28 and 29 used for this work can be found in [44] and [45] (there marked as yellow area).

A flowchart of the algorithm of the calculation of the limit is given in figure 25.

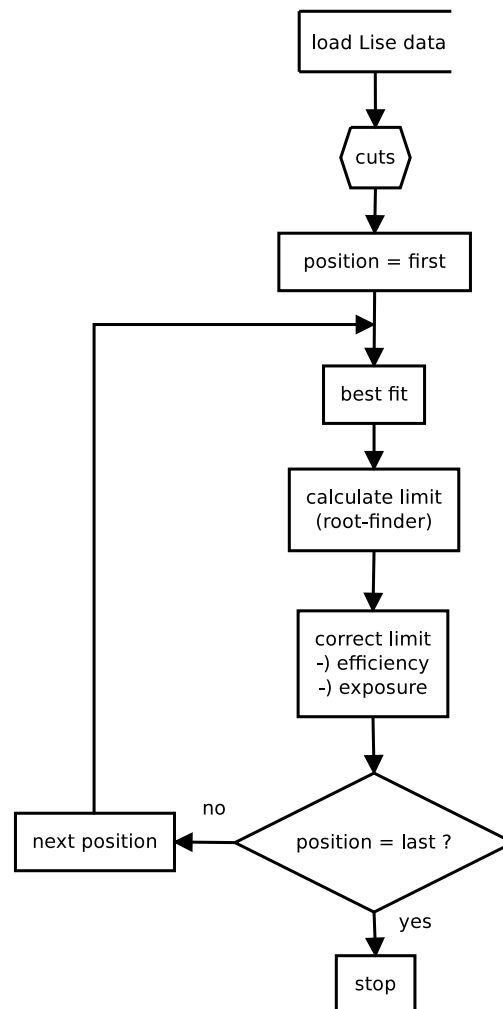


Figure 25: This figure shows the flow-chart of the algorithm to calculate the limit of the Lise data.

4.5. Test-Software

Wilks' theorem states that the true but unknown values of the estimated parameters are in the interior of the parameter space. This can be violated in, for example, random or mixed effects models when one of the variance components is negligible relative to the others. In some such cases, one variance component is essentially zero relative to the others or the models are not properly nested. Therefore the true distribution of this likelihood ratio statistic could be substantially different from the naive χ^2 .

Although the result from the frequentist approach is in good agreement with the one from a Bayesian approach (compare in figure 31 and 32), to make a statement about the calculated result and its quality, the used algorithm had to be tested, what was done with Monte Carlo simulations (pseudo data).

The first step was to create pseudo data ("toy Monte Carlo" data) distributed according to the data measured with the Lise detector module. Therefore each of the 5 components of the model were produced via a poisson process. An example of the lise data, the pseudo data and a fit to the pseudo data is shown in figure 28 (for a signal peak at the low edge of the spectrum) and zoomed in to see the background peaks in figure 29.

The data were created with the signal peak at a fixed position and a specific value for its peak height. Then the limit was calculated with the same procedure as in sec. 4.4 (and 4.3). This was done in a loop of 1000 to 30000 times (runs) for each peak position. A flowchart of the algorithm to control the calculation of the limit is given in figure 26. If the method to calculate the limit was totally correct, then in 90% of the runs the calculated limit values (per position) should be above the adjusted value for the signal peak.

At first it was assumed, that this method could possibly fail for energies below 1 keV because of the decreasing behaviour due to the efficiency and be correct above 1 keV. But for all tested positions (below and above 1 keV) the test software worked and resulted not in an 90%, but in a $\approx 94\%$ (93% - 95%) limit.

Because of this also pseudo data created with several other models were checked: just 1 Gauss peak, Gauss $\cdot \varepsilon$, Gauss + Const and (Gauss + Const) $\cdot \varepsilon$ and all gave a similar result of $\approx 94\%$.

Due to the results from all of this tested models and positions, the used method for calculating a 90% upper limit can be said to be on the side of conservatism.

One direct cause for this can not be determined, but there are several possible reasons:

- the precision of the routines (MINUIT2, MIGRAD) in calculating the parameter estimates and their variances;
- the difference in magnitude of the different components;
- the precision of the root finder
- Wilks' theorem could be on the edge of asymptotic due to the restriction of some parameters, especially for the POI n_{sig} to be positive.

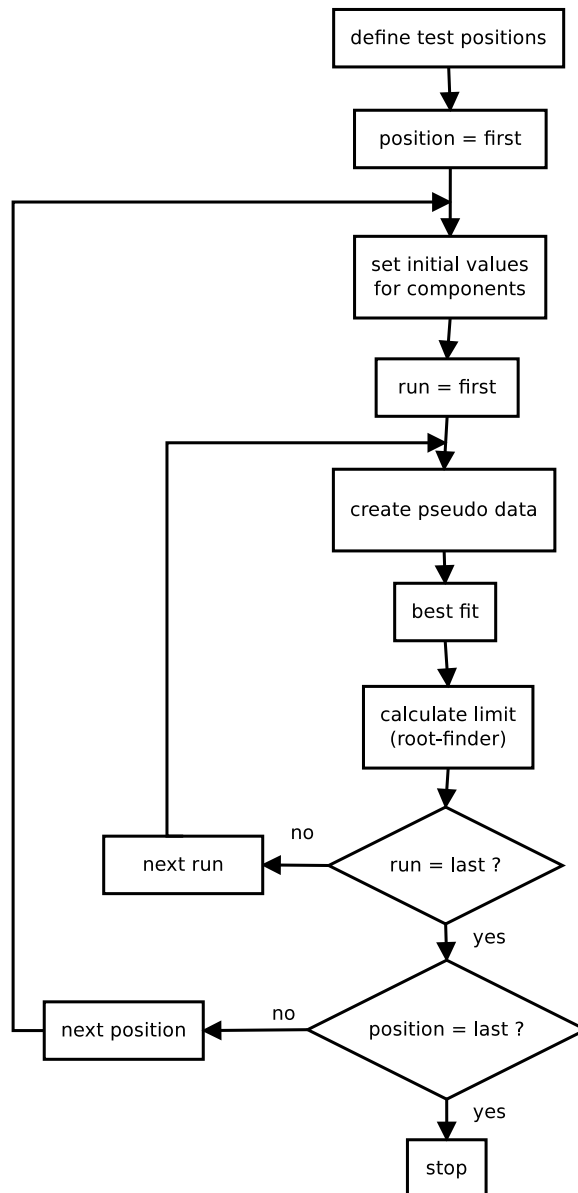


Figure 26: This figure shows the flow-chart of the algorithm to check the calculation of the limit of the Lise data.

Therefore in the next section the attempt to proof, if the distribution of $t(\eta)$ (eq. (83)) follows a χ^2 distribution, as stated by Wilks' theorem, is explained.

4.5.1. Testing the $t(\eta)$ - vs. χ_1^2 - distribution

To check the distribution of the t-values in the used method events were created (in a Poisson process; pseudo data) to form just one Gauss peak. A flowchart of the algorithm to produce the t distribution is given in figure 27.

Two attempts were carried out. At first a Gauss peak containing 10 events and second containing 1000 events, was created. Both attempts were carried out in 100000 runs. The result for both of them with the method explained in the previous chapter was again $\approx 94\%$. For the Gauss peak with 10 events 896907 (of the 100000, 89.6907%) calculated t values were below the χ_1^2 -90%-quantile (2.705543). For the Gauss peak with 1000 events 89.907% were < 2.705543 .

The t distribution for 10 events in the peak, compared with a χ^2 distribution with 1 dof, can be seen in figure 34. The same figure, but zoomed in, with an other binning and also drawn the 90% quantiles of both distributions can be seen in figure 35. The t distribution for 1000 events in the peak compared with a χ_1^2 distribution and both their 90% quantiles can be seen in figure 36. For both attempts a distribution resembling a χ_1^2 distribution can be determined.

Further it can be seen, that the value of the quantile for the Gauss peak with 1000 events is closer to the quantile of the χ_1^2 distribution then in the case with 10 events in the peak. This could be one sign for the asymptotic accuracy of high event rates.

Finally it shall be noted, that this procedure was a simplified approach and easy in computation (because of just one component in the model, what not even demands and extended pdf) for an estimation of the behaviour of the method in order to invest not too much time. Using a more complex model by adding more components (not to mention the model of this work) would require more time, much more power of computing, an optimization of the algorithm in runtime and simplifying the calculation steps, but could proof the asymptotic correctness of the used procedure.

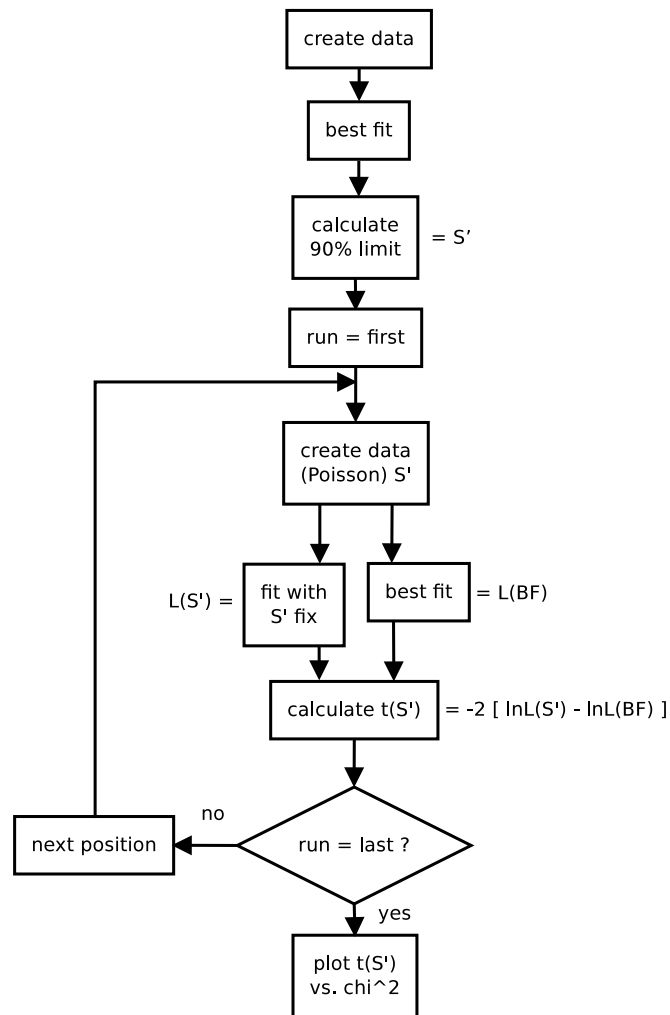


Figure 27: This figure shows the flow-chart of the algorithm to the t distribution of the algorithm.

4.6. Results

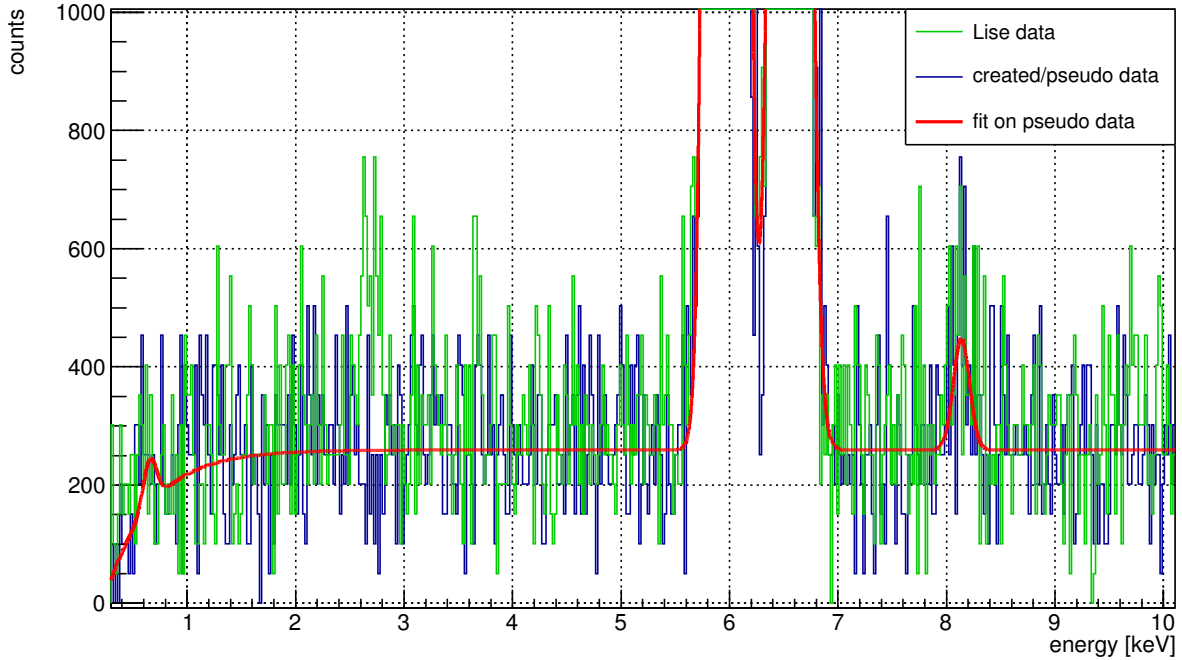


Figure 28: This figure shows the correlation between pseudo data and the data from Lise, a fit to the pseudo data with the signal peak fixed at a value in the low energy region and the decline at low energies caused due to the detector efficiency (eq. (75)). Also the $\text{Fe-}K_\alpha$ (at ≈ 6.0 keV), $\text{Fe-}K_\beta$ (at ≈ 6.6 keV) and the Cu (at ≈ 8.1 keV) peaks can be seen. On the y-axis are the counts per keV. Although an unbinned fit was performed, for the visualization the intern binning of Root should be kept in mind.

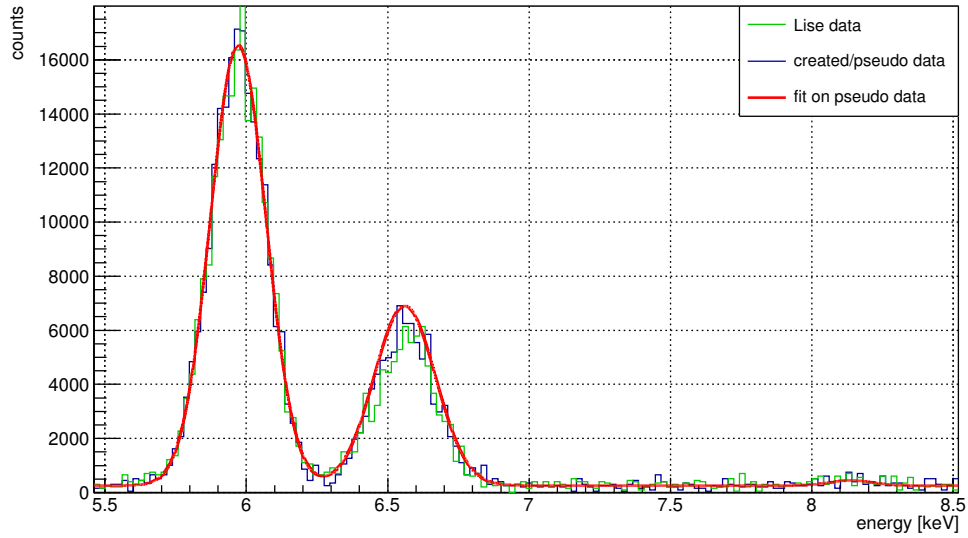


Figure 29: This figure serves to compare the height of the three background peaks - $\text{Fe-}K_{\alpha}$ (at ≈ 6.0 keV), $\text{Fe-}K_{\beta}$ (at ≈ 6.6 keV) and the Cu (at ≈ 8.1 keV). On the y-axis are the counts per keV. Although an unbinned fit was performed, for the visualization the intern binning of Root should be kept in mind.

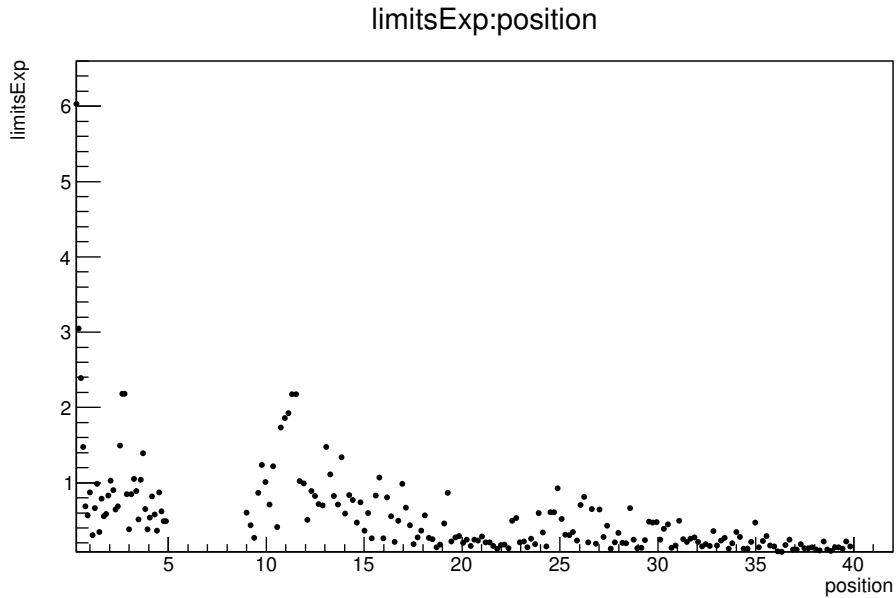


Figure 30: This figure shows the frequentist 90% upper limit for the Lise data on the y-axis, in units per kg days (compare eq. (87)). On the x-axis is the energy in [keV], with the 200 positions (energy values) at which the limit was calculated. The region from ≈ 5 keV to ≈ 9 keV was spared because of the three background peaks lying in this range ($\text{Fe-}K_{\alpha}$ (at ≈ 6.0 keV), $\text{Fe-}K_{\beta}$ (at ≈ 6.6 keV) and the Cu (at ≈ 8.1 keV)).

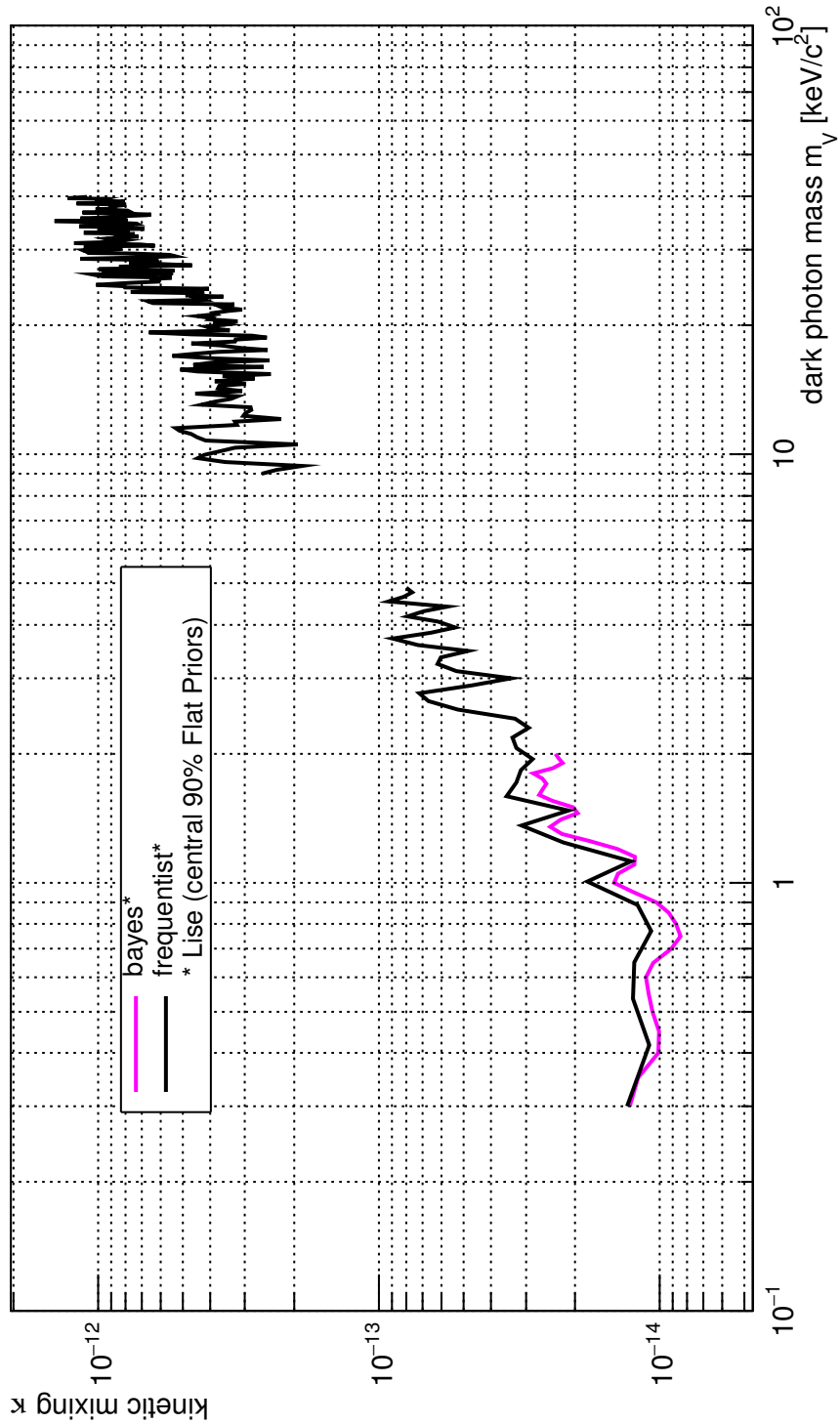


Figure 31: This figure shows the frequentist 90% upper limit on the dark photon kinetic mixing κ (eq. (47)) for the Lise data on the y-axis, over the dark photon mass m_ν on the x-axis compared with a result obtained with a Bayesian approach. The region from ≈ 5 keV to ≈ 9 keV was spared because of the three background peaks lying in this range (Fe- K_α (at ≈ 6.0 keV), Fe- K_β (at ≈ 6.6 keV) and the Cu (at ≈ 8.1 keV)).

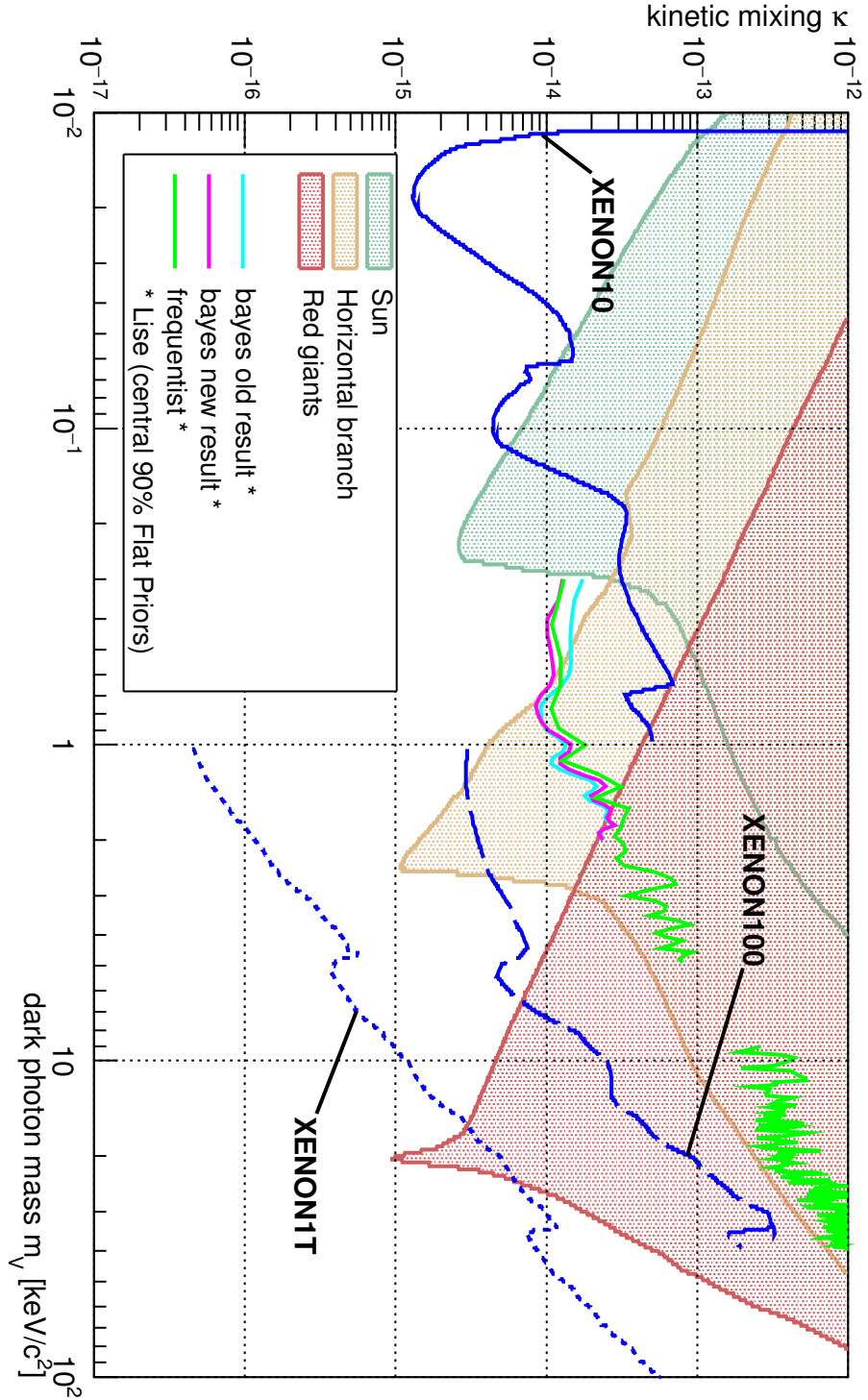


Figure 32: This figure shows the frequentist 90% upper limit on the dark photon kinetic mixing κ (eq. (47)) for the Lise data on the y-axis, over the dark photon mass m_ν on the x-axis, compared with a result obtained with a Bayesian approach. Additional limits obtained with other experiments (XENON) as well as astrophysical constraints from [40] are shown. The region from ≈ 5 keV to ≈ 9 keV was spared because of the three background peaks lying in this range (Fe- K_α (at ≈ 6.0 keV), Fe- K_β (at ≈ 6.6 keV) and the Cu (at ≈ 8.1 keV)).

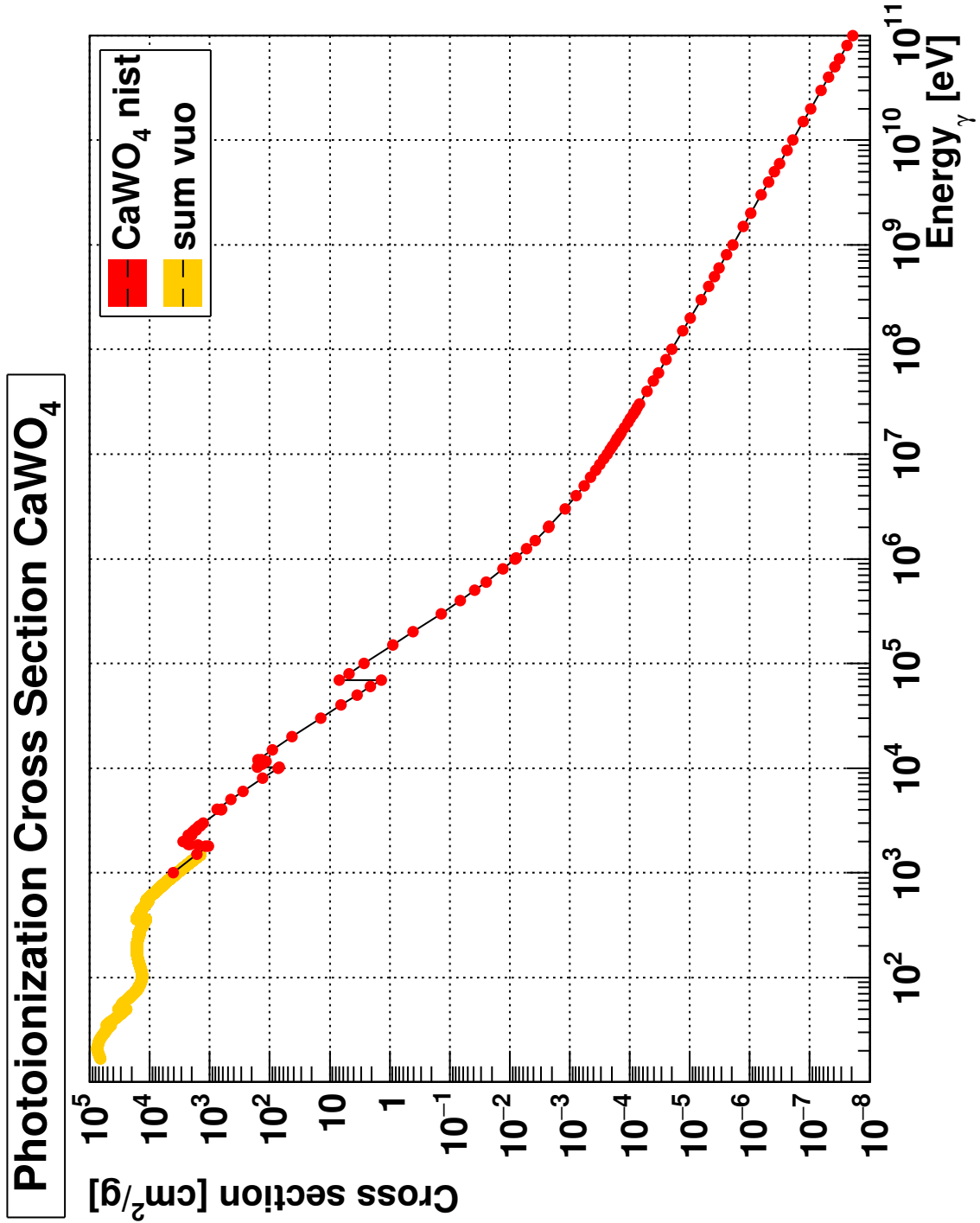


Figure 33: This figure shows the photon cross section (σ_γ) used for the calculation of the dark photon kinetic mixing κ via eq. (47) for CaWO₄ used in the detector module Lise. For the cross section data from NIST (red, [55]) and from VUO (yellow, [56]) were combined.

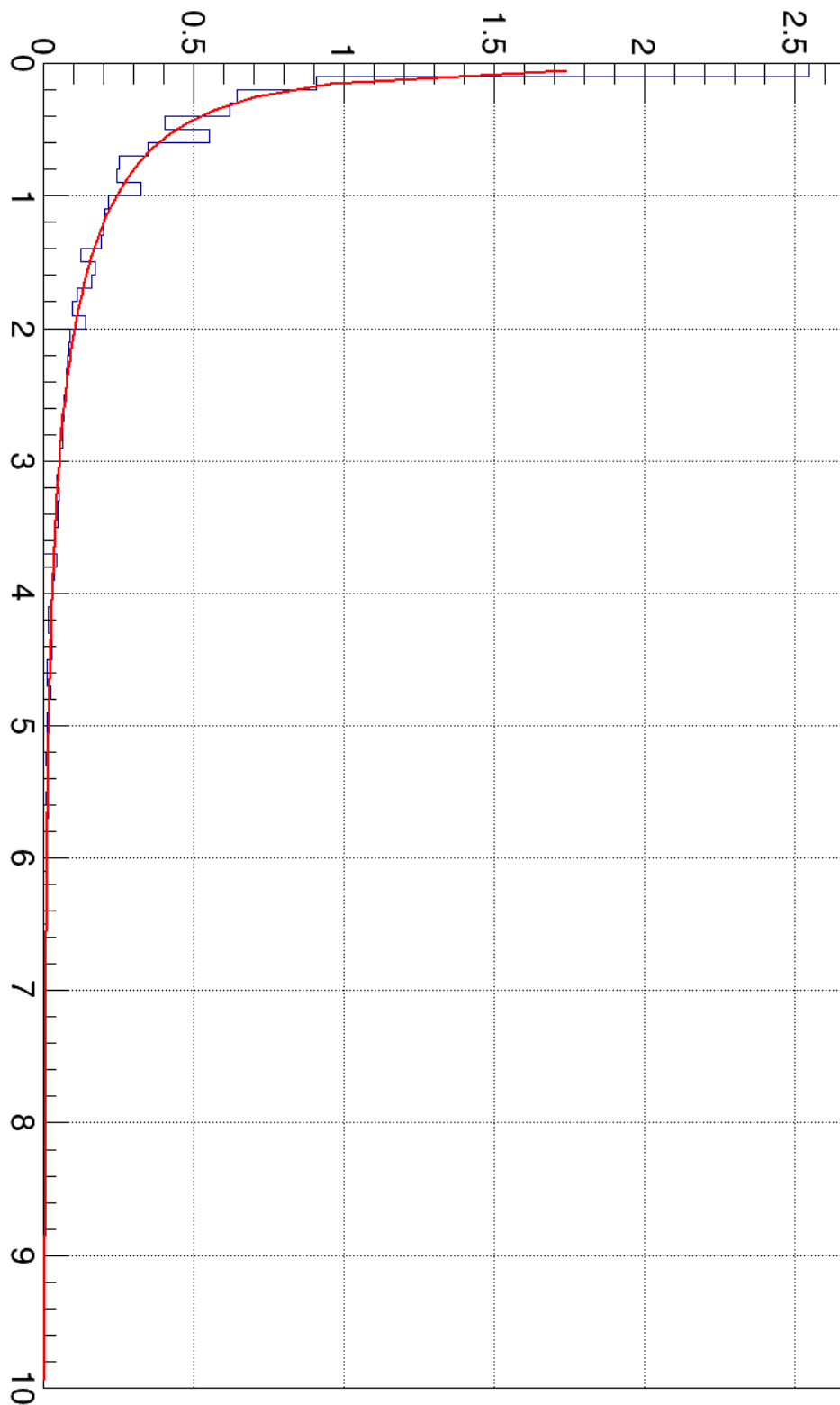


Figure 34: This figure shows the t distribution of the used procedure to calculate the limit for a model of one Gauss peak with 10 events, evaluated with 100.000 runs compared with a χ^2 distribution with 1 dof.

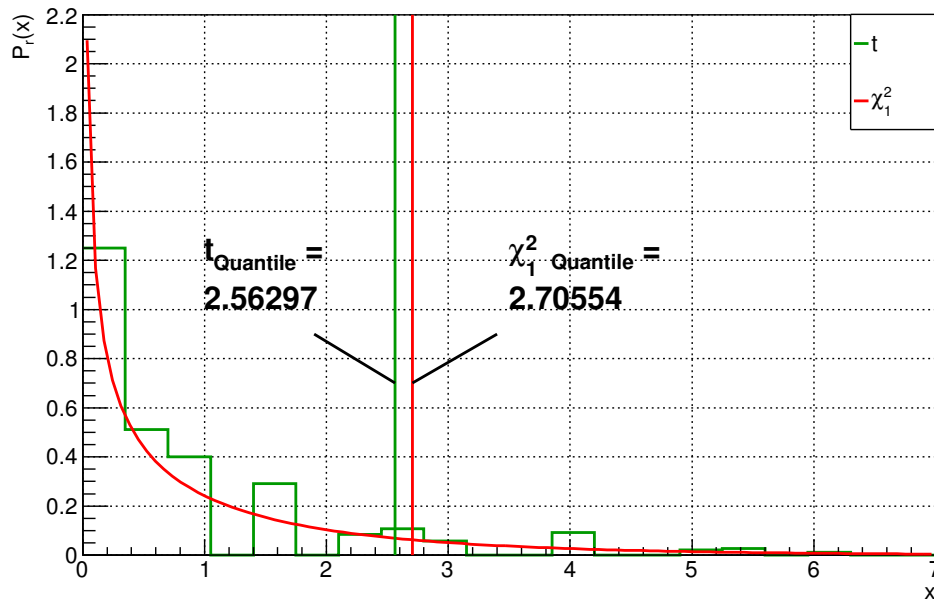


Figure 35: This figure shows the t distribution of the used procedure to calculate the limit for a model of one Gauss peak with 10 events, evaluated with 100.000 runs compared with a χ^2 distribution with 1 dof. It is the same as fig. 34 but zoomed in and given the 90% quantiles for both distributions. For clarity 20 bins were chosen.

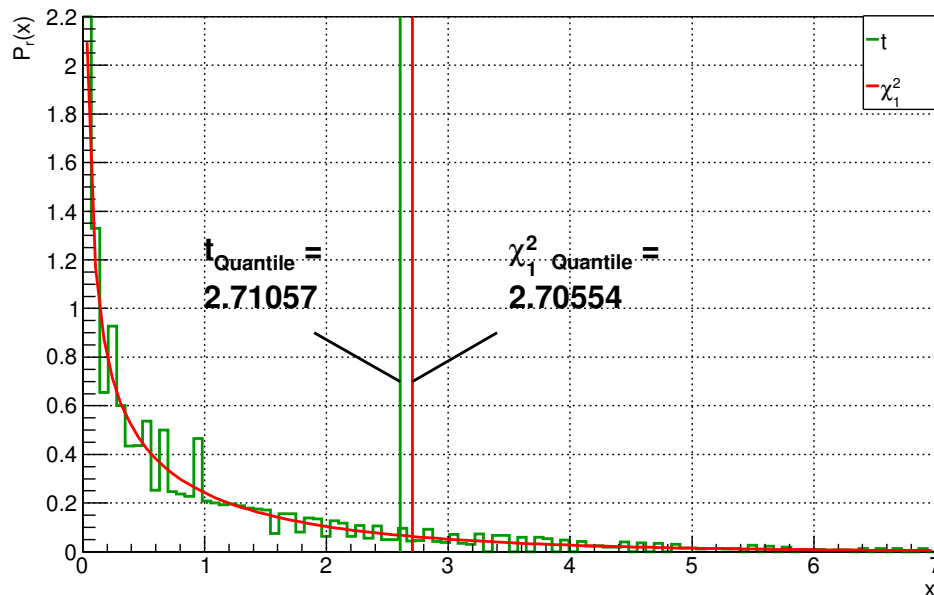


Figure 36: This figure shows the t distribution of the used procedure to calculate the limit for a model of one Gauss peak with 1000 events, evaluated with 100.000 runs compared with a χ^2 distribution with 1 dof and for both distributions the 90% quantiles.

A. Appendix

A.1. Redshift and Doppler Effect

The distinction between redshift and blueshift is simply a matter of whether z is positive or negative. Some redshifts are an example of the Doppler effect. A redshift occurs whenever a light source moves away from an observer. Another kind of redshift is cosmological redshift, which is due to the expansion of the universe, and sufficiently distant light sources (generally more than a few million light years away) show redshift corresponding to the rate of increase in their distance from Earth. Finally, gravitational redshift is a relativistic effect observed in electromagnetic radiation moving out of gravitational fields. Conversely, a decrease in wavelength is called blueshift and is generally seen when a light-emitting object moves toward an observer or when electromagnetic radiation moves into a gravitational field.

A.2. Distance Measurement

Here just a short list and brief explanations are given on how the distance (from earth) to objects in the universe can be measured.

A.2.1. Stellar Parallax

With parallax one can measure the distances to nearby stars. It is $1/2$ angle through which a star's position shifts as earth orbits the sun (actually this only works in determining stellar distances for nearby stars). (The nearest stars are f.e. Alpha Centauri complex (triple-star system) with *Proxima Centauri* at 1.3 pc (4.3 ly) and *Barnard's Star* at 1.8 pc (6.0 ly).) Since stellar parallax fails beyond ≈ 100 parsecs, other methods are necessary.

A.2.2. Standard Candle

If it is known how bright something really is (known as Luminosity or Absolute Brightness) then from how bright it appears (Apparent Brightness) it can be determined how far away it is. This follows simply from the inverse square law, see eq. (1). Supernovae measuring distances to other galaxies. For the biggest distances the Redshift and Hubble's Law are used to measure distances to such objects.

A.2.3. Pulsating Variable Stars

This is a standard candle, which allows us to measure distances out to about 25 million parsecs (25 Mpc), distances in our Galaxy and to nearby galaxies. Examples are *R Lyrae variables* (used to determine distances to globular clusters and size of the Milky Way and that Andromeda is outside the Milky Way), and *Cepheid variables*.

The pulsation period of each of these stars depends on luminosity. Therefore, a measurement of the pulsation period immediately tells the star's luminosity, its apparent brightness can be seen and from the inverse square law, the distance can be determined.

A.3. Cosmology

Astronomy and cosmology became the oldest sciences pursued by mankind. In this modern era, astronomy and cosmology are completely embedded into the framework of physics. The experimental science of astronomy refined its methods and techniques which allowed the ever improving exploration of the Universe. Since the invention of the telescopes, astronomers were able to investigate the Universe to ever increasing ranges. The last century saw the advent of several new messengers observable by astronomers, apart from the visible light, observations throughout the electromagnetic spectrum became possible. Also high energetic particles known as cosmic rays widened the window through which the Universe became observable.

Cosmology is the study of the universe as a whole, including its origin, structure, and evolution. The theoretical framework of **Standard model of cosmology** can be viewed as the sum of: General relativity + cosmological principle + FLRW metric (an expanding universe) + Friedmann equation. The following subsections will give a brief explanation to this components.

A.3.1. General Relativity

General relativity is the description of the large scales of the universe (gravity). Modern scientific cosmology is usually considered to have begun in 1917 with Albert Einstein's publication of his final modification of general relativity in the paper "Cosmological Considerations of the General Theory of Relativity". The Einstein field equations (EFE) (first published by A. Einstein in 1915 as a tensor equation) may be written in the form:

$$\underbrace{R_{\mu\nu} - \frac{1}{2}R g_{\mu\nu}}_{\equiv G_{\mu\nu}} + \Lambda g_{\mu\nu} = \frac{8\pi G}{c^4} T_{\mu\nu}, \quad (88)$$

where $R_{\mu\nu}$ is the Ricci curvature tensor, R is the scalar curvature, $g_{\mu\nu}$ is the metric tensor, Λ is the cosmological constant, G is Newton's gravitational constant, c is the speed of light in vacuum, and $T_{\mu\nu}$ is the stress-energy tensor. $G_{\mu\nu}$ is the Einstein tensor, a specific divergence-free combination of the Ricci tensor and the metric, where $G_{\mu\nu}$ is symmetric. The relationship between the metric tensor and the Einstein tensor allows the EFE to be written as a set of non-linear partial differential equations (i.e. a system of 10 coupled, nonlinear, hyperbolic-elliptic partial differential equations). The EFE obeying local energy-momentum conservation (since Λ is constant, the energy conservation law is unaffected). The left side of eq. (88) represents the curvature of spacetime as determined by the metric; the expression on the right represents the matter/energy content of spacetime. The EFE can then be interpreted as a set of equations dictating

how matter/energy determines the curvature of spacetime. (Note: for sufficiently large Λ a spherical Universe may also expand forever.)

A.3.2. FLRW Metric

The metric of an expanding Universe can be described in short as follows. The Friedmann-Lemaître-Robertson-Walker (FLRW) metric is an exact solution of Einstein's field equations of general relativity. It is proven that the FLRW metric is the only one on a spacetime that is spatially homogeneous and isotropic (this is a geometric result and is not tied specifically to the equations of general relativity). The quantities dx^μ being regarded as the components of an infinitesimal coordinate displacement four-vector, the metric ($g_{\mu\nu}$) determines the invariant square of an infinitesimal line element, often referred to as an interval. Starting with a flat (static) space with the interval often denoted as

$$ds^2 = g_{\mu\nu}dx^\mu dx^\nu . \quad (89)$$

The interval ds^2 (ds the space-time interval) imparts information about the causal structure of spacetime. x^μ are local coordinates, where μ is an index which runs from 0 to 3 (the factors dx^μ are one-form gradients of the scalar coordinate fields x^μ). Coming from spherical coordinates:

$$ds^2 = dt^2 - (dr^2 + r^2d\theta^2 + r^2 \sin^2 \theta d\phi^2) \quad (90)$$

and adding the "scale factor" $R(t)$ (sometimes denoted as a , and \dot{a} for the expansion rate of the universe) containing all of the time dependence for an expanding space delivers:

$$ds^2 = dt^2 - R(t)^2 \cdot (dr^2 + r^2d\theta^2 + r^2 \sin^2 \theta d\phi^2) . \quad (91)$$

And finally the constant k representing the curvature of the space needs to be added:

$$ds^2 = dt^2 - R(t)^2 \cdot \left(\frac{dr^2}{1 - kr^2} + r^2d\theta^2 + r^2 \sin^2 \theta d\phi^2 \right) . \quad (92)$$

where k is the curvature = -1, 0 or 1 for an open, flat or closed Universe ($k > 0$: spherical geometry; $k < 0$: hyperbolic geometry). Then r is unitless and $a(t)$ has units of length. When $k = \pm 1$, $a(t)$ is the radius of curvature of the space, and may also be written $R(t)$. In this case, the Einstein equations lead to the Friedmann equation (see eq. (31)) which governs the expansion of the Universe (with ρ is the energy density).

A.3.3. Friedmann Equation

The solution of Einstein's field equations for general relativity, assuming homogeneous and isotropic distribution of matter and radiation behaving like a perfect, frictionless fluid, describes the evolution of the Universe. This solution for the temporal development of the Universe was first found by Alexander Friedmann (introducing ρ the average density).

For the special case of non-relativistic matter it can be understood with simple Newtonian mechanics: a point mass m is accelerated by gravity at the surface of a sphere of radius R , density ρ , mass $M = \frac{4\pi R^3 \rho}{3}$:

$$H_0^2 = \underbrace{\frac{v^2}{R^2}}_{\text{kinetic energy}} = \underbrace{\frac{8\pi G}{3}\rho}_{\text{- potential energy}} - \underbrace{\frac{k}{R^2}}_{\text{total energy}}. \quad (93)$$

A.4. Milky Way

This section provides briefly some facts about the nowadays state of knowledge about the Milky Way (MW).

In infrared, or far-infrared the structure of a disk and a bulge starts to be revealed, and with modern instrumentation and techniques it is now known, that the MW is a spiral galaxy (compare with fig. 39, 38 and 37) and consists of:

- the Galactic Bulge - which is composed of old stars (population II) and young stars (population I) shaped like a football (about half as wide as long);
- the Galactic Disk - consists old stars (population II) and young stars (population I), gas, and dust and appears in the shape Spiral arms;
- the Galactic Halo - has a spherical shape, includes globular clusters, which contain only old stars (population II) and has a radius of about 65000 light years, whereat it contains neither gas nor dust;
- the Dark Halo - with a radius of 200000 or 300000 light years contains 80%-95% of the mass of the galaxy (dark matter)

Figure 37 is a representation of the Milky Way and its dark matter halo. The Galactic disk is surrounded by a spheroidal halo of old stars and globular clusters, of which 90% lie within 100000 light-years (30 kpc) of the Galactic Center. It results from analysed data from a survey of stars called SEGUE (Sloan Extension for Galactic Understanding and Exploration), which is part of a larger project called the Sloan Digital Sky Survey (SDSS) that uses a 2.5-metre telescope in New Mexico. The stars in the sample ranged from about 13000 to nearly 200000 light years from the galactic centre. The Sun is about 25000 light years from the centre. [57]

A *halo* can be defined as an overdensity (> 200 kpc) with respect to background (and also defines the virial radius), whereas a *sub-halo* is a self-bound object within the virial radius of a halo.

The distance from the Earth (or our solar system) to the galactic nucleus is about 30000 light years and the total mass of the Milky Way can be estimated to $10^{12} \cdot M_{\odot}$.

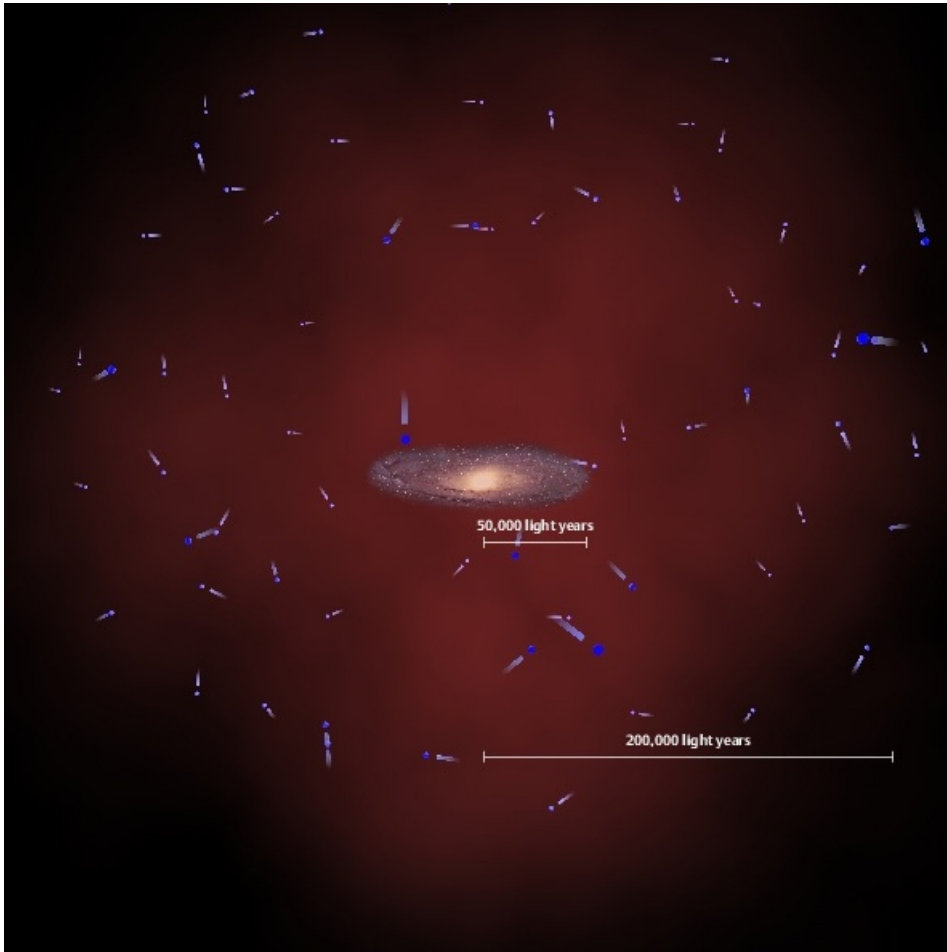


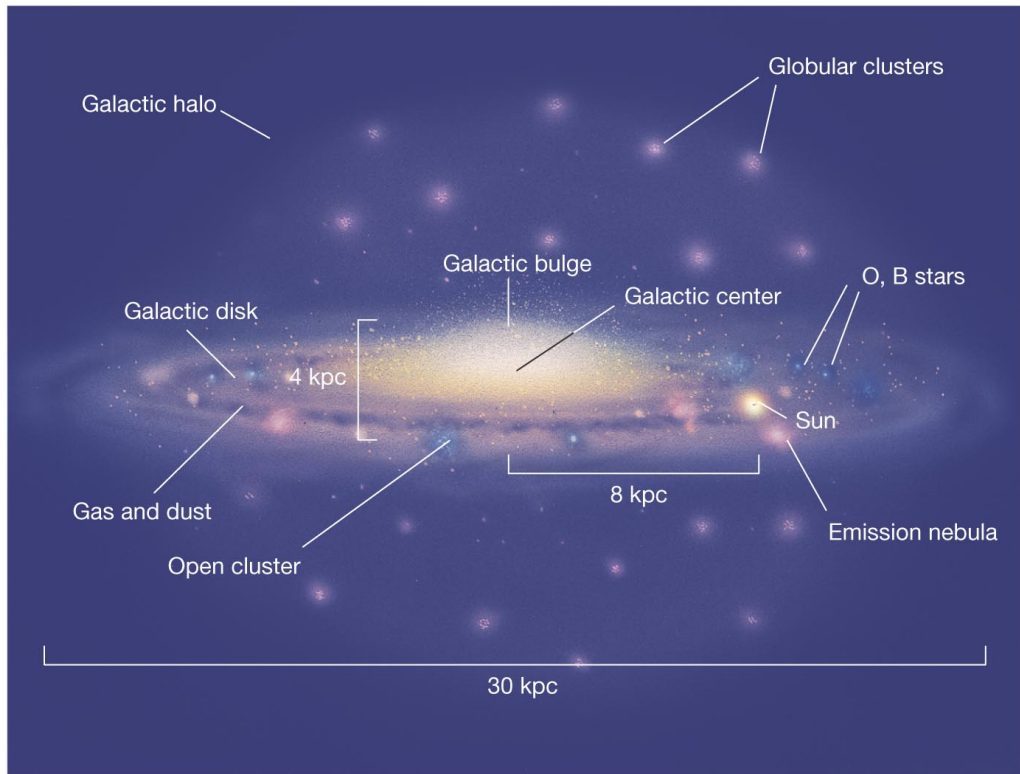
Figure 37: Illustration: Axel Quetz/Max Planck Institute for Astrophysics-Heidelberg/SDSS-II Collaboration that measured the velocities of nearly 2500 stars suggests that the true mass is just under 1 trillion Suns. [57], [58]

The Milky Way has formed as it is through Evolution. The first stars were formed in a very large region of space, with matter spread out in irregular patterns. The first stars (population II) formed more than 10 billion years ago, and collapsed into globular clusters. Huge region of clouds of primordial gas and early stars collapsed into large cloud of matter. The galaxy continued to Evolve, as the slowly spinning cloud collapsed into the disk and the dense core. Leaving behind stars formed early as a halo.

The disk rich in gas and dust formed, from which the Sun (and our solar system) emerged about 5 billion years ago.

The *interstellar medium* is the matter that exists in the space between the star systems in a galaxy. This matter includes gas in ionic, atomic, and molecular form, as well as dust and cosmic rays and consists of 90% hydrogen, 1% dust, 9-10% helium.

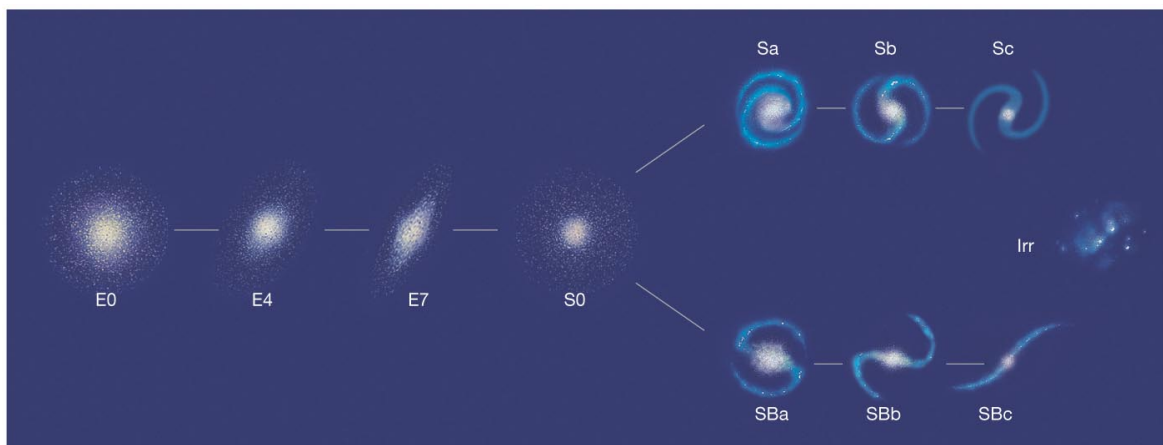
Stars near the galactic Center are found to be in orbits consistent with those expected when orbiting a mass of about 4 million solar masses. Many Astronomers nowadays believe a supermassive black hole is the only explanation for the data. This shall be a



Copyright © 2008 Pearson Education, Inc., publishing as Pearson Addison-Wesley.

Figure 38: Representation of the Milky Way and some of its characteristics. [57], [59]

region of space in which matter has collapsed to the point where nothing can escape - not even light! Many astronomers believe the mass equivalent to $\approx 4 \cdot 10^6$ suns has collapsed to the center of the MW. It is called **Sagittarius A***. Supermassive black holes are now generally accepted to be at the centres of most spiral and elliptical galaxies.



Copyright © 2008 Pearson Education, Inc., publishing as Pearson Addison-Wesley.

Figure 39: Hubble tuning fork diagram. Categorisation of Galaxies. [60]

A.5. Galaxy Clusters

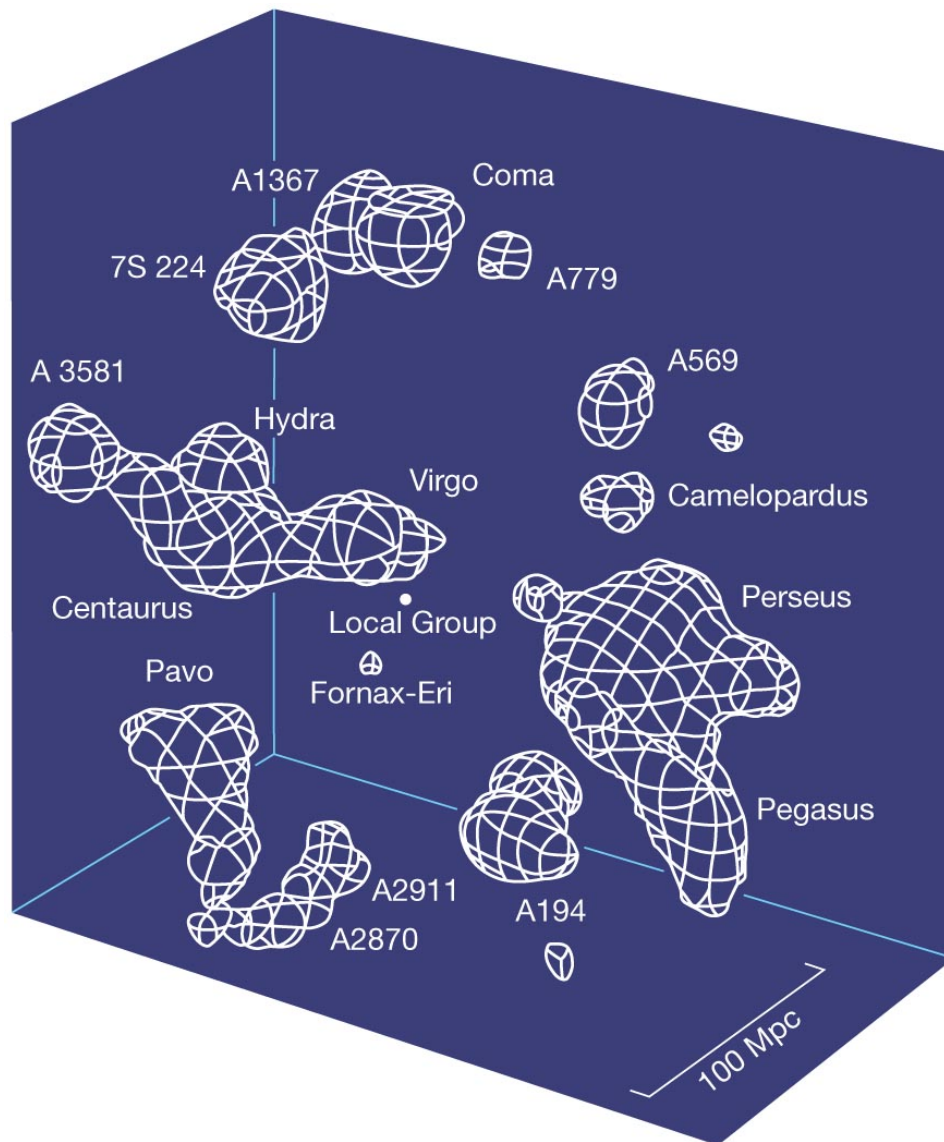
Nearly 50 galaxies populate the local neighbourhood of the Milky Way. These major astronomical objects within about 1 Mpc of the Milky Way Galaxy are bound together by their combined gravity. Such a group of galaxies is called a **galaxy cluster**. Our cluster is called the *Local Group*. The composition of the Local Group (nearly 50 galaxies) consists of 3 spirals (the Milky Way, Andromeda (M31), and M33), irregulars (like the Large Magellanic Cloud and Small Magellanic Cloud), dwarf irregulars or dwarf ellipticals (M32 is a dwarf elliptical near Andromeda (M31)).

The Local Cluster is a galaxy "poor" cluster, what means that there are a relatively small number of galaxies in the Local Group compared to rich clusters (such as Virgo and Coma with thousands of galaxies).

On very large scales the galaxies are not distributed randomly. The huge spaces between galaxy clusters are called *the voids*. Intergalactic space is the physical space between galaxies. Surrounding and stretching between galaxies, there is a rarefied plasma that is organized in a galactic filamentary structure. This material is called the *intergalactic medium* (IGM). "Bubbles" of galaxies surround these unpopulated regions.

Galaxies in clusters often collide, for example the Cartwheel galaxy (where a smaller galaxy has collided with larger one), NGC 2207 and IC 2163 (two spiral galaxies which have swung past each other), or the antennae. These encounters have substantial effects on galaxies, whereby stars glide past one another, with essential no effect on the individual stars, while tidal forces cause bursts of new star formation with major effects on the galaxies themselves. The Andromeda galaxy is approaching the Milky Way at 120 km/s, and will collide in a few billion years.

Galaxy clusters are themselves clustered into *superclusters* like the Virgo Supercluster - a 3 dimensional visualization can be seen in fig. 40. *The Great Wall* is one of the largest known structures in the universe and measures ≈ 200 Mpc in width. In a new way of defining superclusters from 2014 according to the relative velocities of galaxies the local supercluster subsumes the prior defined local supercluster, the Virgo Supercluster, now an appendage of the **Laniakea Supercluster**, which is the galaxy supercluster that is home to the Milky Way and 100,000 other nearby galaxies. [61] It stretched out over 160 megaparsecs (520 million light-years). Superclusters are some of the universe's largest structures and have boundaries that are difficult to define, especially from the inside. Within a given supercluster, most galaxy motions will be directed inward, toward the center of mass, what in the case of Laniakea is called the *Great Attractor*, and influences the motions of the Local Group of galaxies and all others throughout the supercluster. Unlike its constituent clusters, Laniakea is not gravitationally bound and is projected to be torn apart by dark energy. Also Laniakea is shown to be heading in the direction of the Shapley Supercluster, so both Shapley and Laniakea may be part of a even greater complex.



Copyright © 2008 Pearson Education, Inc., publishing as Pearson Addison-Wesley.

Figure 40: Virgo Supercluster in 3D. [62]

A.6. Gas in the Universe

At the beginning of the hunt for dark matter there also were considerations if the gas within galactic clusters (Intracluster Gas) could explain much of the dark matter. It would be only faintly visible, but over large volumes could it add up enough to explain dark matter?

There are several places where gas resides:

- Interstellar medium (between stars within a galaxy) - about 1 atom per cubic cm
- Intergalactic medium (between galaxies within the cluster - intracluster) - about

$10^{-6} \frac{\text{atoms}}{\text{cm}^3}$, or about 1 atom per cubic meter

- Intercluster medium (between galactic clusters) - very little matter

Observations from hot gas came from X-ray emission of Abell 85, a distant galaxy cluster, where gas extends into the space between galaxies, but revealed, that it does not add up sufficiently to solve the missing matter problem (need dark matter). Further evidence of gas external to galaxies came from radio lobes of radio galaxies. These head-tail radio galaxy show what appears to result from galaxies travelling through intergalactic medium. The amount of mass required to bind this gas to the clusters (see the Virgo Cluster) greatly exceeds the total visible mass of the galaxies (more evidence of dark matter).

There is no evidence for such gas beyond the clusters, in the "extraluster" spaces. There is a lot of intracluster gas but **it doesn't come close to accounting for the dark matter.**

A.7. Horizontal Branch

The horizontal branch (HB) is a stage of stellar evolution that immediately follows the red giant branch in stars whose masses are similar to the Sun's. Horizontal-branch stars are powered by helium fusion in the core (via the triple-alpha process) and by hydrogen fusion (via the CNO cycle) in a shell surrounding the core, compare fig. 17. The onset of core helium fusion at the tip of the red giant branch causes substantial changes in stellar structure, resulting in an overall reduction in luminosity, some contraction of the stellar envelope, and the surface reaching higher temperatures.

A.8. Vectors, scalars, and spinors

Mathematically it may look as though all of the fields are vector-valued (in addition to being operator-valued), since they all have several components, can be multiplied by matrices, etc., but physicists assign a more specific physical meaning to the word: a vector is something which transforms like a four-vector under Lorentz transformations, and a scalar is something which is invariant under Lorentz transformations. The B , W_j , and G_a fields are all vectors in this sense, so the corresponding particles are said to be vector bosons. The Higgs field ϕ is a scalar.

The fermion field ψ does transform under Lorentz transformations, but not like a vector should; rotations will only turn it by half the angle a proper vector should. Therefore, these constitute a third kind of quantity, which is known as a spinor.

It is common to make use of abstract index notation for the vector fields, in which case the vector fields all come with a Lorentzian index μ , like so: B^μ , W_j^μ , and G_a^μ . If abstract index notation is used also for spinors then these will carry a spinorial index and the Dirac gamma will carry one Lorentzian and two spinorian indices, but it is more common to regard spinors as column matrices and the Dirac gamma γ_μ as a matrix which additionally carries a Lorentzian index.

A.9. The Lagrangian

Lagrangian field theory applies to continua and fields, which have an infinite number of degrees of freedom. The time integral of the Lagrangian is called the action denoted by \mathcal{S} . The Lagrangian mechanics formalism was generalized further to handle field theory, whereat the independent variable is replaced by an event in spacetime (x, y, z, t) , or more generally still by a point s on a manifold. The dependent variables (q) are replaced by the value of a field at that point in spacetime $\varphi(x, y, z, t)$ so that the equations of motion are obtained by means of an action principle, written as:

$$\frac{\delta \mathcal{S}}{\delta \varphi_i} = 0. \quad (94)$$

The time integral of the Lagrangian L is the action

$$\mathcal{S} = \int L dt. \quad (95)$$

In field theory, a distinction is occasionally made between the Lagrangian L and the Lagrangian density \mathcal{L} , whereat the Lagrangian as a function of generalized coordinates is replaced by a Lagrangian density, a function of the fields in the system and their derivatives, and possibly the space and time coordinates themselves. In field theory, the independent variable t is replaced by an event in spacetime (x, y, z, t) or still more generally by a point s on a manifold. So, simplified, the spatial volume integral of the Lagrangian density is the Lagrangian, in 3 dimensions

$$L = \int \mathcal{L} d^3 \mathbf{x}. \quad (96)$$

Often, a "Lagrangian density" is simply referred to as a "Lagrangian". This density must be integrated over all spacetime to get the action, where the action, \mathcal{S} is a functional of the dependent variables $\varphi_i(s)$ with their derivatives and s itself

$$\mathcal{S}[\varphi] = \int \mathcal{L}(\varphi, \nabla \varphi, \partial \varphi / \partial t, \mathbf{x}, t) d^3 \mathbf{x} dt. \quad (97)$$

Quantum field theories in particle physics, are usually described in terms of \mathcal{L} , and the terms in this form of the Lagrangian translate quickly to the rules used in evaluating Feynman diagrams.

List of Figures

1.	Rotation curve of the typical spiral galaxy M33 (yellow and blue points with errorbars) and the predicted one from distribution of the visible matter (white line). The discrepancy between the two curves is accounted for by adding a dark matter halo surrounding the galaxy. [9]	7
2.	The velocity distribution for the barred spiral galaxy NGC 3198. The dots from the measurement indicate a massive halo, the lines correspond to models with contributions from a halo or a disk. [14]	8
3.	Velocity distribution of the planets within our solar system with the nice $v \propto \frac{1}{\sqrt{r}}$ distribution. [5]	9
4.	A lens of mass M will deflect light from a distant source by an angle $\hat{\alpha}$ dependent on the impact parameter ζ . [5] [17]	12
5.	Composite picture of the bullet cluster. Optical image of the Bullet Cluster (1E 0657-558), overlaid with a X-ray observation (red) and a lensing map (blue). For details see text. Credit: X-ray: NASA/CXC/CfA/M.Markevitch et al.; Optical: NASA/STScI; Magellan/U.Arizona/D.Clowe et al.; Lensing Map: NASA/STScI; ESO WFI; Magellan/U.Arizona/D.Clowe et al. [19] [25]	15
6.	Content of the universe at an age of 380000 a.	17
7.	The anisotropies of the Cosmic microwave background (CMB) as observed by Planck. The CMB is a snapshot of the oldest light in our Universe, imprinted on the sky when the Universe was just 380 000 years old. It shows tiny temperature fluctuations that correspond to regions of slightly different densities, representing the seeds of all future structure: the stars and galaxies of today. [27]	19
8.	The TT power spectrum of the CMB anisotropies as measured by PLANCK. On the upper panel on the vertical axis the band-power estimates \mathcal{D}_l in μK^2 are shown, while the lower panel shows the residuals between measurement and model. The uncertainties include both the statistical instrumental noise and cosmic variance. The red curve is the best-fit Λ CDM model to the data. On the horizontal axis the multipole moment l and the corresponding angular size are shown. Figure taken from [26].	20
9.	Energy matter density content of our current universe.	21
10.	Evolution of density. [28]	22

11. Spectrum of the blackbody radiation at different temperatures T . [29] . . .	23
12. A schematic depiction of the Standard Model of elementary particles, with the three generations of matter (first three columns), gauge bosons in the fourth column, and the Higgs boson in the fifth. [31]	35
13. The missing satellite and "too big to fail" problems. (<i>Left</i>) Projected dark matter distribution (600 kpc on a side) of a simulated, $10^{12}M_{\odot}$ CDM halo (Garrison-Kimmel, Boylan-Kolchin, & Bullock, in preparation). The numerous small sub-halos far exceed the number of known Milky Way satellites. Circles mark the nine most massive sub-halos. (<i>Right</i>) Spatial distribution of the "classical" satellites of the Milky Way. The central densities of the sub-halos in the left panel are too high to host the dwarf satellites in the right panel, predicting stellar velocity dispersions higher than observed. The diameter of the outer sphere in the right panel is 300 kpc; relative to the simulation prediction (and to the Andromeda galaxy) the Milky Way's satellite system is unusually centrally concentrated (Yniguez et al. 2013). [33]	40
14. Feynman diagram with the possible interaction for studying non-gravitational interaction between matter and dark matter. To describe the various approaches the arrow indicating the evolution of time and space needs to be rotated. Fig. taken from [35].	42
15. Example Feynman diagrams contributing to: spin-independent WIMP-quark scattering (a) and WIMP-gluon scattering (b), spin-dependent WIMP-quark scattering (c). Figure taken from [5] and based on [36].	44
16. Several well-motivated candidates of DM are shown in the log-log plane of DM relic mass and σ_{int} representing the typical strength of interactions with ordinary matter. The red, pink and blue colors represent HDM, WDM and CDM, respectively. Figure taken from [30].	52
17. Schematic Globular Cluster color-magnitude diagram. The structure of stars corresponding to the different branches of the diagram are indicated. Figure taken from [41]	61
18. This figure shows a sketch of the experimental setup of the CRESST-II Cryostat, taken from [42].	64
19. This figure shows a schematic drawing of the horizontal bands resulting from different event types in the light yield-energy plane, taken from [43].	66
20. This figure shows a schematic sketch of the conventional design of the CRESST-II detector module, taken from [43].	67

21. This is a picture of the Lise detector module (conventional design), on the left is the light absorber for scintillation-light detection, with a silicon-on-sapphire disc with a diameter of 40 mm and a thickness of 500 μm , and on the right is the phonon detector, where on top are the three clamps (bright) holding the crystal and the W-thermometer (TES, dark rectangle) on top of the CaWO_4 -crystal, taken from [43].	68
22. The structure of CaWO_4 , taken from [47].	69
23. The p -quantile, with $p \in (0, 1)$, is the value of a r.v., which splits its quantity in two sections, left of the p -quantile is p ($= 100 \cdot p\%$); on the right-hand side the remaining $1-p$ ($= 100 \cdot (1 - p)\%$).	78
24. Shape and fit (red) (of (75)) of the efficiency of the detector module Lise, with energy on the x-axis in [keV] and with the threshold of $x_{\text{low}} = 0.3$ keV.	88
25. This figure shows the flow-chart of the algorithm to calculate the limit of the Lise data.	94
26. This figure shows the flow-chart of the algorithm to check the calculation of the limit of the Lise data.	96
27. This figure shows the flow-chart of the algorithm to the t distribution of the algorithm.	98
28. This figure shows the correlation between pseudo data and the data from Lise, a fit to the pseudo data with the signal peak fixed at a value in the low energy region and the decline at low energies caused due to the detector efficiency (eq. (75)). Also the Fe-K_α (at ≈ 6.0 keV), Fe-K_β (at ≈ 6.6 keV) and the Cu (at ≈ 8.1 keV) peaks can be seen. On the y-axis are the counts per keV. Although an unbinned fit was performed, for the visualization the intern binning of Root should be kept in mind.	99
29. This figure serves to compare the height of the three background peaks - Fe-K_α (at ≈ 6.0 keV), Fe-K_β (at ≈ 6.6 keV) and the Cu (at ≈ 8.1 keV). On the y-axis are the counts per keV. Although an unbinned fit was performed, for the visualization the intern binning of Root should be kept in mind.	100
30. This figure shows the frequentist 90% upper limit for the Lise data on the y-axis, in units per kg days (compare eq. (87)). On the x-axis is the energy in [keV], with the 200 positions (energy values) at which the limit was calculated. The region from ≈ 5 keV to ≈ 9 keV was spared because of the three background peaks lying in this range (Fe-K_α (at ≈ 6.0 keV), Fe-K_β (at ≈ 6.6 keV) and the Cu (at ≈ 8.1 keV)).	100

31. This figure shows the frequentist 90% upper limit on the dark photon kinetic mixing κ (eq. (47)) for the Lise data on the y-axis, over the dark photon mass m_V on the x-axis compared with a result obtained with a Bayesian approach. The region from ≈ 5 keV to ≈ 9 keV was spared because of the three background peaks lying in this range (Fe- K_α (at ≈ 6.0 keV), Fe- K_β (at ≈ 6.6 keV) and the Cu (at ≈ 8.1 keV)).	101
32. This figure shows the frequentist 90% upper limit on the dark photon kinetic mixing κ (eq. (47)) for the Lise data on the y-axis, over the dark photon mass m_V on the x-axis, compared with a result obtained with a Bayesian approach. Additional limits obtained with other experiments (XENON) as well as astrophysical constraints from [40] are shown. The region from ≈ 5 keV to ≈ 9 keV was spared because of the three background peaks lying in this range (Fe- K_α (at ≈ 6.0 keV), Fe- K_β (at ≈ 6.6 keV) and the Cu (at ≈ 8.1 keV)).	102
33. This figure shows the photon cross section (σ_γ) used for the calculation of the dark photon kinetic mixing κ via eq. (47) for CaWO ₄ used in the detector module Lise. For the cross section data from NIST (red, [55]) and from VUO (yellow, [56]) were combined.	103
34. This figure shows the t distribution of the used procedure to calculate the limit for a model of one Gauss peak with 10 events, evaluated with 100.000 runs compared with a χ^2 distribution with 1 dof.	104
35. This figure shows the t distribution of the used procedure to calculate the limit for a model of one Gauss peak with 10 events, evaluated with 100.000 runs compared with a χ^2 distribution with 1 dof. It is the same as fig. 34 but zoomed in and given the 90% quantiles for both distributions. For clarity 20 bins were chosen.	105
36. This figure shows the t distribution of the used procedure to calculate the limit for a model of one Gauss peak with 1000 events, evaluated with 100.000 runs compared with a χ^2 distribution with 1 dof and for both distributions the 90% quantiles.	105
37. Illustration: Axel Quetz/Max Planck Institute for Astrophysics-Heidelberg/SDSS-II Collaboration that measured the velocities of nearly 2500 stars suggests that the true mass is just under 1 trillion Suns. [57], [58]	111
38. Representation of the Milky Way and some of its characteristics. [57], [59]	112
39. Hubble tuning fork diagram. Categorisation of Galaxies. [60]	112
40. Virgo Supercluster in 3D. [62]	114

References

- [1] Andrew Liddle. *An introduction to modern cosmology*. 2009.
- [2] K. Duncan C. J. Conselice A. Wilkinson and A. Mortlock. “The Evolution of Galaxy Number Density at $z < 8$ and its Implications”. In: *ArXiv e-prints* (July 2016). arXiv: 1607.03909.
- [3] E. P. Hubble. In: *Proc. Nat. Acad. Sci.* 15, 168 (1929).
- [4] G. Lemaître. In: *Annales de la Société Scientifique de Bruxelles*, 47, 49 (1929).
- [5] Jochen Schieck and Holger Kluck. “Script on Dark Matter”. Institute of High Energy Physics - Vienna University of Technology, 2015.
- [6] F. Zwicky. “Die Rotverschiebung von extragalaktischen Nebeln”. In: *Helv.Phys.Acta*, 6:110–127 (1933).
- [7] V. C. Rubin and W. K. Ford Jr. “Rotation of the Andromeda Nebula from a Spectroscopic Survey of Emission Regions”. In: *The Astrophysical Journal*, vol. 159 (1970).
- [8] N. Thonnard V. C. Rubin and W. K. Ford Jr. “Rotational properties of 21 sc galaxies with a large range of luminosities and radii, from ngc 4605 ($r = 4$ kpc) to ugc 2885 ($r = 122$ kpc)”. In: *Astrophys. J.*, 238:471-487 (1980).
- [9] Stefania Deluca. *Extended rotation curve of M33*. URL: https://commons.wikimedia.org/wiki/File:M33_rotation_curve_HI.gif.
- [10] Ants Kaasik Jaan Einasto and Enn Saar. “Dynamic evidence on massive coronas of galaxies”. In: *nature*, 250:309-310 (1974).
- [11] P. J. E. Peebles J. P. Ostriker and A Yahil. “The size and mass of galaxies, and the mass of the universe”. In: *Astrophys. J.*, 193:L1-L4 (1974).
- [12] Robert Minchin et al. “A Dark hydrogen cloud in the Virgo cluster”. In: *Astrophys. J.* 622 (2005), pp. L21–L24. DOI: 10.1086/429538. arXiv: astro-ph/0502312 [astro-ph].
- [13] Pieter van Dokkum et al. “A High Stellar Velocity Dispersion and 100 Globular Clusters for the Ultra Diffuse Galaxy Dragonfly 44”. In: (2016). arXiv: 1606.06291 [astro-ph.GA].
- [14] K. Begeman T. S. van Albada John N. Bahcall and R. Sancisi. “The Distribution of Dark Matter in the Spiral Galaxy NGC 3198”. In: *Astrophys. J.*, 295:305-313 (1985).
- [15] Carlos S. Frenk Julio F. Navarro and Simon D. M. White. “The structure of cold dark matter halos”. In: *Astrophys. J.* 462 (1996), pp. 563–575.
- [16] F. W. Dyson, A. S. Eddington, and C. Davidson. “A Determination of the Deflection of Light by the Sun’s Gravitational Field, from Observations Made at the Total Eclipse of May 29, 1919”. In: *Philosophical Transactions of the Royal Society of London Series A* 220 (1920), pp. 291–333. DOI: 10.1098/rsta.1920.0009.

-
- [17] Michael Sachs. *Diagram of angles involved in gravitational lensing*. URL: <https://en.wikipedia.org/wiki/File:Gravitational-lensing-angles.png>.
- [18] Matthias Bartelmann and Peter Schneider. “Weak gravitational lensing”. In: *Phys. Rep.* 340 (2014), pp. 291–472.
- [19] A. H. Gonzalez D. Clowe M. Bradač et al. “A direct empirical proof of the existence of dark matter”. In: *Astrophys. J.* 648 (2006), pp. L109–L113.
- [20] Avery A. Meiksin. “The physics of the intergalactic medium”. In: *Rev. Mod. Phys.* 81 (2009), pp. 1405–1469.
- [21] T. Kitching D. Harvey R. Massey et al. “The non-gravitational interactions of dark matter in colliding galaxy clusters”. In: *Science* 347 (2015), pp. 1462–1465.
- [22] W. Tucker et al. “1e0657-56: a contender for the hottest known cluster of galaxies”. In: *Astrophys. J.* 496 (1998), p. L5. DOI: 10.1086/311234. arXiv: astro-ph/9801120 [astro-ph].
- [23] J. Lee and E. Komatsu. “Bullet Cluster: A Challenge to Λ CDM Cosmology”. In: *The Astrophysical Journal* 718 (July 2010), pp. 60–65. DOI: 10.1088/0004-637X/718/1/60.
- [24] J. W. Moffat. “Gravitational Lensing in Modified Gravity and the Lensing of Merging Clusters without Dark Matter”. In: (2006). arXiv: astro-ph/0608675 [astro-ph].
- [25] STScI and ESO WFI et al NASA. *1e 0657-56: Nasa finds direct proof of dark matter*. URL: <http://chandra.harvard.edu/photo/2006/1e0657/index.html>.
- [26] C. Armitage-Caplan P. A. R. Ade N. Aghanim and M. Arnaud et al. “Planck 2013 results. XVI. Cosmological parameters”. In: *Astron. Astrophys.* 571:A16 (2014). DOI: <http://dx.doi.org/10.1051/0004-6361/201321591>.
- [27] ESA and the Planck Collaboration. *Planck CMB*. URL: http://www.esa.int/spaceinimages/Images/2013/03/Planck_CMB.
- [28] Jim Brau. URL: http://pages.uoregon.edu/jimbrou/BrauImNew/Chap27/7th/AT_7e_Figure_27_01.jpg.
- [29] Jim Brau. *Blackbody Radiation*. URL: http://pages.uoregon.edu/jimbrou/BrauImNew/Chap03/7th/AT_7e_Figure_03_10.jpg.
- [30] Howard Baer et al. “Dark matter production in the early Universe: beyond the thermal WIMP paradigm”. In: *Phys. Rept.* 555 (2015), pp. 1–60. DOI: 10.1016/j.physrep.2014.10.002. arXiv: 1407.0017 [hep-ph].
- [31] Wikipedia. *Standard Model of Elementary Particles*. URL: https://commons.wikimedia.org/wiki/File:Standard_Model_of_Elementary_Particles.svg.
- [32] W. J. G. de Blok. “The Core-Cusp Problem”. In: *Advances in Astronomy* 2010, 789293 (2010). DOI: 10.1155/2010/789293. arXiv: 0910.3538.

-
- [33] David H. Weinberg et al. “Cold dark matter: controversies on small scales”. In: *Sackler Colloquium: Dark Matter Universe: On the Threshold of Discovery Irvine, USA, October 18-20, 2012*. 2013. arXiv: 1306.0913 [astro-ph.CO]. URL: <https://inspirehep.net/record/1237028/files/arXiv:1306.0913.pdf>.
- [34] J. S. Bullock M. Boylan-Kolchin and M. Kaplinghat. “Too big to fail? The puzzling darkness of massive Milky Way subhaloes”. In: *Monthly Notices of the Royal Astronomical Society* (July 2011). DOI: 10.1111/j.1745-3933.2011.01074.x. arXiv: 1103.0007 [astro-ph.CO].
- [35] J. Hutchinson S. Chang R. Edezhath and M. Luty. “Effective WIMPs”. In: *Phys. Rev.* D89(1):015011 (2014).
- [36] Marc Kamionkowski Gerard Jungman and Kim Griest. “Supersymmetric dark matter”. In: *Phys. Rept.* 267:195 (1996).
- [37] R. D. Peccei and Helen R. Quinn. “CP conservation in the presence of pseudoparticles”. In: *Phys. Rev. Lett.* 38:1440 (1977).
- [38] Sean M. Carroll Lotty Ackerman Matthew R. Buckley and Marc Kamionkowski. “Dark Matter and Dark Radiation”. In: *Phys. Rev.* D79 (2009). [,277(2008)], p. 023519. DOI: 10.1103/PhysRevD.79.023519, 10.1142/9789814293792_0021. arXiv: 0810.5126 [hep-ph].
- [39] Huitzu Tu Jonathan L. Feng and Hai-Bo Yu. “Thermal Relics in Hidden Sectors”. In: *JCAP* 0810 (2008), p. 043. DOI: 10.1088/1475-7516/2008/10/043. arXiv: 0808.2318 [hep-ph].
- [40] Haipeng An et al. “Direct Detection Constraints on Dark Photon Dark Matter”. In: *Phys. Lett.* B747 (2015), pp. 331–338. DOI: 10.1016/j.physletb.2015.06.018. arXiv: 1412.8378 [hep-ph].
- [41] G. Raffelt. “Neutrinos and the stars”. In: *ArXiv e-prints* (Jan. 2012). arXiv: 1201.1637 [astro-ph.SR].
- [42] URL: <http://www.cresst.de/facility.php>.
- [43] URL: <http://www.cresst.de/cresst.php>.
- [44] G. Angloher et al. “Results on low mass WIMPs using an upgraded CRESST-II detector”. In: *Eur. Phys. J.* C74.12 (2014), p. 3184. DOI: 10.1140/epjc/s10052-014-3184-9. arXiv: 1407.3146 [astro-ph.CO].
- [45] G. Angloher et al. “Results on light dark matter particles with a low-threshold CRESST-II detector”. In: *Eur. Phys. J.* C76.1 (2016), p. 25. DOI: 10.1140/epjc/s10052-016-3877-3. arXiv: 1509.01515 [astro-ph.CO].
- [46] M. J. Treadway and R. C. Powell. In: *J. Chem. Phys.* 61 (1974), pp. 4003–4011.
- [47] URL: http://home.arcor.de/geologie-mineralogie/mineralogie/lumi/struktur_scheelit.jpg.
- [48] A.N. Kolmogorov. *Grundbegriffe der Wahrscheinlichkeitsrechnung*. 1933.

- [49] Glen Cowan. *Statistical Data Analysis*. 1998.
- [50] F. James and M. Roos. “CERN Program Library routine D506 (long write-up)”. In: *F. James, Interpretation of the Errors on Parameters as given by MINUIT, supplement to long write-up of routine D506 (1978)*. 1989.
- [51] S. S. Wilks. “The Large-Sample Distribution of the Likelihood Ratio for Testing Composite Hypotheses”. In: *Ann. Math. Statist.* 9.1 (Mar. 1938), pp. 60–62. DOI: 10.1214/aoms/1177732360. URL: <http://dx.doi.org/10.1214/aoms/1177732360>.
- [52] John P. Huelsenbeck and Keith A. Crandall. “PHYLOGENY ESTIMATION AND HYPOTHESIS TESTING USING MAXIMUM LIKELIHOOD”. In: *Annual Review of Ecology and Systematics* 28.1 (1997), pp. 437–466. DOI: 10.1146/annurev.ecolsys.28.1.437. URL: <http://dx.doi.org/10.1146/annurev.ecolsys.28.1.437>.
- [53] G. Angloher et al. “Commissioning Run of the CRESST-II Dark Matter Search”. In: *Astropart. Phys.* 31 (2009), pp. 270–276. DOI: 10.1016/j.astropartphys.2009.02.007. arXiv: 0809.1829 [astro-ph].
- [54] G. Angloher et al. “Limits on WIMP dark matter using scintillating CaWO_4 cryogenic detectors with active background suppression”. In: *Astropart. Phys.* 23 (2005), pp. 325–339. DOI: 10.1016/j.astropartphys.2005.01.006. arXiv: astro-ph/0408006 [astro-ph].
- [55] National Institute of Standards and Technology (NIST). *XCOM: Photon Cross Sections Database*. URL: <http://physics.nist.gov/PhysRefData/Xcom/html/xcom1.html>.
- [56] Elettra - Sincrotrone Trieste S.C.p.A. *Atomic Calculation of Photoionization Cross-Sections and Asymmetry Parameters*. URL: <https://vuo.elettra.eu/services/elements/WebElements.html>.
- [57] David Shiga. *Milky Way’s mass is drastically reduced*. URL: <https://www.newscientist.com/article/dn13997-milky-ways-mass-is-drastically-reduced/>.
- [58] Axel Quetz. *Milky Way dark matter halo*. URL: https://d1o50x50snmhul.cloudfront.net/wp-content/uploads/2008/05/dn13997-1_567.jpg.
- [59] Jim Brau. *Milky Way*. URL: http://pages.uoregon.edu/jimbrou/BrauImNew/Chap23/6th/23_10Figure-F.jpg.
- [60] Jim Brau. *Hubble tuning fork diagram*. URL: http://pages.uoregon.edu/jimbrou/BrauImNew/Chap24/6th/24_09Figure-F.jpg.
- [61] Yehuda Hoffman R. Brent Tully Hélène Courtois and Daniel Pomarède. “The Laniakea supercluster of galaxies”. In: *Nature* 513 (2014), pp. 71–73. DOI: 10.1038/nature13674. URL: <http://dx.doi.org/10.1038/nature13674>.
- [62] Jim Brau. *Virgo Supercluster in 3D*. URL: http://pages.uoregon.edu/jimbrou/BrauImNew/Chap25/6th/25_22Figure-F.jpg.